# Ultra-high Precision, Absolute, Earth Gravity Measurements

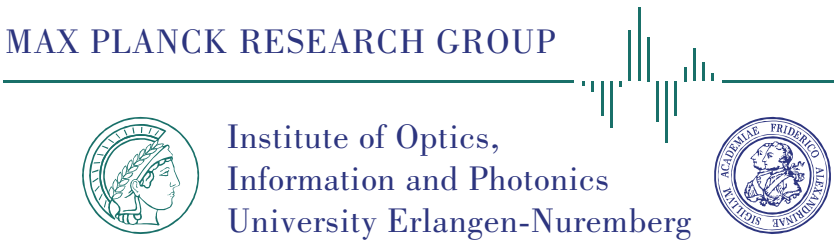


Den Naturwissenschaftlichen Fakultäten der
Friedrich-Alexander-Universität Erlangen-Nürnberg
zur
Erlangung des Doktorgrades

vorgelegt von

Christian Rothleitner

aus Berlin

Als Dissertation genehmigt
von den Naturwissenschaftlichen Fakultäten
der Universität Erlangen-Nürnberg

Tag der mündlichen Prüfung: 26. Juni 2008

| | |
|---|---|
| Vorsitzender der Promotionskommission: | Prof. Dr. Eberhard Bänsch |
| Erstberichterstatter: | Prof. Lijun Wang, Ph.D. |
| Zweitberichterstatter: | Prof. Dr. Thomas Fauster |

# Abstract

Within the framework of this thesis two apparatuses for an absolute measurement of gravity were designed, constructed, and tested for the purpose of detecting long-term variations of gravity, determining the absolute gravity value for metrological applications, and for research in fundamental physics. The work includes a stationary gravimeter, which functions as a highly accurate reference system and a portable gravimeter, which is aimed for field measurements.

The principle these gravimeters use to determine the gravity value is based on the relation between the falling distance, the falling time, and the acceleration due to gravity. A Michelson interferometer measures the distance change between a falling object mirror and an inertial reference mirror with a Helium-Neon laser (633 nm). The whole fringe signal is digitized by a high-speed ADC, which is disciplined by a rubidium frequency standard. This fringe recording is novel compared to common gravimeters, which use an analogue zero-crossing determination.

Our portable gravimeter's mechanics also deviate from the standard type. Springs, preloaded by a small motor accelerate the carriage supporting the falling object. This reduces the shock vibrations on the system.

Furthermore, a novel method was developed to reduce the uncertainty due to the falling body's rotation. The position of the optical centre is determined in order to subsequently superpose it with the falling object's centre of mass by means of a common balancing method. Resolutions of distance of less than 16 $\mu$m were reached in three dimensions, which reduces the uncertainty contribution to less than 0.7 $\mu$Gal (7 nm s$^{-2}$).

A complete uncertainty budget is given for both gravimeters. The combined standard uncertainty for the portable gravimeter is estimated to give 38.4 $\mu$Gal, and that for the stationary 16.6 $\mu$Gal, whereas for the portable gravimeter a standard error of 1.6 $\mu$Gal (statistical uncertainty for 24 hours of measurement), and

for the stationary gravimeter 0.6 $\mu$Gal (1 month of measurement) was reached. This is comparable to the resolution of the world's best absolute gravimeters.

The portable gravimeter was brought to the European Comparison of Absolute Gravimeters (ECAG) 2007 in Luxembourg, and to another comparison with the German Federal Agency of Cartography and Geodesy (Bundesamtes für Kartographie und Geodäsie – BKG), where it showed an agreement of the measured values obtained with other gravimeters within the instrument's uncertainty.

# Zusammenfassung

Im Rahmen dieser Arbeit wurden ein stationäres und ein tragbares Gerät zur Absolutschweremessung entworfen, gebaut und getestet. Die Geräte sollen sowohl zur Messung von Langzeit-Schwereänderungen und zum Einsatz in der Metrologie, als auch in der Grundlagenforschung verwendet werden. Das stationäre Gravimeter soll hierbei als ein hochgenaues Referenzgerät dienen, wohingegen das tragbare Gravimeter für Feldmessungen ausgelegt ist.

Das hier angewandte Messprinzip zur Bestimmung des absoluten Schwerewertes beruht auf der Beziehung zwischen Fallhöhe, Fallzeit und Schwerebeschleunigung. Mit Hilfe eines Michelson-Interferometers wird die Entfernungsänderung zwischen einem fallenden Objektspiegel und dem inert gelagerten Referenzspiegel gemessen. Als Längenstandard dient hier ein Helium-Neon-Laser (633 nm). Das komplette Interferenzsignal wird mittels eines ultraschnellen Analog-Digital-Wandlers, der durch eine Rubidium-Uhr stabilisiert wird, digitalisiert. Der Schwerewert wird anschließend durch eine eigens entwickelte Software ermittelt. Diese Interferenzsignal-Erfassung ist eine Besonderheit im Vergleich zu herkömmlichen Gravimetern, die üblicherweise eine analoge Erfassung der Nulldurchgänge anwenden.

Das tragbare Gravimeter hat außerdem eine spezielle Mechanik. Federn, die durch einen kleinen Motor vorgespannt werden, dienen dazu den Wagen, der den Fallkörper beinhaltet, nach unten zu beschleunigen. Dies reduziert die Schwingungen, die auf das System übertragen werden.

Ferner wurde eine neuartige Methode entwickelt, die dazu dient, die Unsicherheit zu verringern, die entsteht, wenn der Fallköper während des Freifalls rotiert. Dazu wird die Position des optischen Zentrums des Fallkörpers ermittelt, um anschließend seinen Schwerpunkt zu diesem hin zu verschieben. Ein herkömmliches Auswuchtgerät übernimmt diese Aufgabe. Auflösungen in der Bestimmung der

Entfernung im dreidimensionalen Raum von besser als 16 $\mu$m wurden hierbei erreicht. Dies entspricht einer Unsicherheit von weniger als 0.7 $\mu$Gal (7 nm $s^{-2}$).

Eine vollständige Messunsicherheitsanalyse wurde für beide Gravimeter ermittelt. Für das tragbare Gravimeter beträgt diese 38.4 $\mu$Gal. Für das stationäre Gravimeter sind 16.6 $\mu$Gal anzugeben. Hierbei wurden für das tragbare Gerät ein Standardfehler von 1.6 $\mu$Gal (Messdauer von 24 Stunden) und beim stationären Gerät von 0.6 $\mu$Gal (Messdauer von 1 Monat) gemessen. Dies ist mit der Auflösung der besten Absolutgravimeter weltweit vergleichbar.

Das tragbare Gravimeter nahm an einem europäischen Vergleich von Absolutegravimetern (ECAG), der 2007 in Luxemburg abgehalten wurde, teil und wurde mit dem Gravimeter des Deutschen Bundesamtes für Kartographie und Geodäsie (BKG) verglichen, wobei es eine gute Übereinstimmung innerhalb der ermittelten Messunsicherheit zeigte.

# Contents

**Abstract** **i**

**Zusammenfassung** **iii**

**1 Introduction** **1**

1.1 Theory of gravity . . . . . 3

1.1.1 The figure of the Earth . . . . . 3

1.1.2 Acceleration due to gravity . . . . . 4

1.1.3 Tides . . . . . 7

1.2 Absolute measurement of gravity . . . . . 11

1.2.1 Historical Background . . . . . 13

1.2.2 Free fall gravimeters . . . . . 14

1.2.2.1 Free fall . . . . . 14

1.2.2.2 Symmetric free fall - Rise and fall . . . . . 16

1.2.3 Atom gravimeters . . . . . 17

1.3 Selected applications . . . . . 18

1.3.1 New definition of the Kelvin . . . . . 18

1.3.2 New definition of the kilogram . . . . . 20

1.3.3 Measurement of the Planck constant . . . . . 21

1.3.4 Measurement of the Newtonian constant . . . . . 22

1.3.5 Time keeping . . . . . 22

1.4 Organization of the thesis . . . . . 22

**2 Stationary free fall gravimeter MPG-1** **25**
2.1 Setup . . . 25
2.1.1 Optics and laser . . . 26
2.1.2 Electronics . . . 27
2.1.3 Software . . . 29
2.1.4 Mechanics . . . 32
2.2 Results and analysis . . . 34

**3 Portable free fall gravimeter MPG-2** **39**
3.1 Introduction . . . 39
3.2 Set up . . . 40
3.2.1 Optics and laser . . . 40
3.2.2 Electronics . . . 41
3.2.3 Software . . . 41
3.2.4 Mechanics . . . 41
3.2.5 Results . . . 44
3.3 International comparison ECAG 2007, Walferdange/Luxembourg . . . 45
3.3.1 Discussion of results . . . 47
3.4 Comparison with BKG . . . 47
3.4.1 Discussion of the results . . . 50

**4 High-precision balancing of the falling body** **51**
4.1 Introduction . . . 52
4.2 Balancing in three dimensions . . . 54
4.2.1 Theory of balancing . . . 54
4.2.2 Method . . . 56
4.2.3 Results . . . 61
4.2.4 Uncertainty analysis . . . 63
4.2.4.1 Propagation of uncertainty . . . 63
4.2.4.2 OC coordinates . . . 65
4.2.4.3 Misalignment of the coordinate systems . . . 65
4.2.4.4 Mass values . . . 65
4.2.4.5 Balancing machine calibration . . . 66

4.2.4.6 Dynamic imbalances . . . 67
4.2.4.7 Calculated eccentricities . . . 68
4.2.4.8 COM coordinates and difference between the centres 69
4.3 Method of index balancing . . . 70
4.3.1 Theory of index balancing . . . 70
4.3.1.1 Eccentricity of the mounting jigs . . . 72
4.3.2 Method . . . 72
4.3.3 Results . . . 78
4.3.4 Uncertainty analysis . . . 80
4.3.4.1 Propagation of uncertainty . . . 80
4.3.4.2 OC coordinates . . . 81
4.3.4.3 Mass values . . . 82
4.3.4.4 Calibrating the balancing machine . . . 82
4.3.4.5 Dynamic imbalances . . . 83
4.3.4.6 Calculated eccentricities . . . 83
4.3.4.7 COM coordinates and difference between the centres 83
4.4 Conclusion . . . 85

**5 Uncertainty budgets and possible errors 87**
5.1 Uncertainty budget due to the instrument . . . 88
5.1.1 Vacuum . . . 88
5.1.1.1 Air drag . . . 88
5.1.1.2 Outgassing . . . 89
5.1.1.3 Buoyancy . . . 90
5.1.2 Magnetic field . . . 90
5.1.2.1 Magnetic attraction . . . 90
5.1.2.2 Eddy currents . . . 91
5.1.3 Electrostatic field . . . 91
5.1.4 Influence of instrumental masses . . . 92
5.1.5 Verticality of the laser beam . . . 94
5.1.6 Accuracy and stability of the laser . . . 96
5.1.7 Accuracy and stability of the atomic clock . . . 97
5.1.8 Corner cube rotation . . . 98

5.1.9 Radiation pressure . . . . . 98
5.1.10 Beam divergence . . . . . 99
5.1.11 Temperature effects . . . . . 100
5.1.11.1 Temperature gradient . . . . . 100
5.1.11.2 Effects on the setup . . . . . 101
5.1.12 Floor recoil and seismic vibrations . . . . . 103
5.1.13 Speed of light . . . . . 107
5.1.14 Reference height . . . . . 108
5.1.15 Non-linearity of electronics . . . . . 110
5.2 Uncertainty budget due to environmental effects . . . . . 111
5.2.1 Solid Earth tides . . . . . 111
5.2.2 Ocean loading . . . . . 113
5.2.3 Polar motion . . . . . 113
5.2.4 Pressure effects . . . . . 114
5.2.5 Coriolis force . . . . . 115
5.3 Combined standard uncertainty . . . . . 117
5.3.1 MPG-1 . . . . . 117
5.3.2 MPG-2 . . . . . 118
5.4 Discussion of the uncertainty budgets . . . . . 118

**6 Summary and outlook** **121**

**A List of numbers and physical constants** **125**

**Conclusions and outlook** **124**

**B Results of long term measurements** **127**
B.1 Measurements with MPG-1 . . . . . 127
B.2 Measurements with MPG-2 . . . . . 130

**References** **140**

# List of Figures


1.1 Geoid and reference ellipsoid . . . . . 3
1.2 Gravity as the sum of gravitational force and centrifugal force. . . 5
1.3 Lunar attraction. . . . . 8
1.4 Geocentric reference system. . . . . 10
1.5 Tides calculated with TSoft. . . . . 12
1.6 Tidal spectrum calculated with TSoft. . . . . 12
1.7 Historical overview of increase of accuracy of gravimeters. . . . . 14
1.8 Michelson interferometer in a free fall gravimeter. . . . . 15
1.9 Interference signal generated due to the dropped mirror. . . . . 16
1.10 Rise and fall gravimeter IMGC-2. . . . . 17
1.11 Atom gravimeter from ONERA. . . . . 18
1.12 Watt balance. . . . . 20

2.1 Set up of the stationary gravimeter MPG-1. . . . . 26
2.2 Interferometer set up of MPG-1. . . . . 27
2.3 Data acquisition and processing scheme. . . . . 28
2.4 Workflow of MPG-1. . . . . 29
2.5 Graphical user interface. . . . . 30
2.6 Non phase shifting digital filter. . . . . 31
2.7 Perforated steel belt in MPG-1. . . . . 33
2.8 One month of measured gravity with MPG-1. . . . . 35
2.9 One month of measured gravity with MPG-1 in a closer look. . . . 36
2.10 Residuals of one month of measured gravity with MPG-1. . . . . 37
2.11 Power spectrum from MPG-1 measurement. . . . . 37

## LIST OF FIGURES


3.1 Set up of the portable free fall gravimeter MPG-2. . . . . 40
3.2 Michelson interferometer on the Super Spring. . . . . 41
3.3 PCI extension for MPG-2. . . . . 42
3.4 Workflow of MPG-2. . . . . 43
3.5 Mechanics of MPG-2. . . . . 44
3.6 Long-term measurement with MPG-2. . . . . 45
3.7 Measurement site of ECAG 2007 in Walferdange, Luxembourg . . 46
3.8 Measurement at the site C4 at ECAG 2007. . . . . 46
3.9 Measurement at all sites at ECAG 2007. . . . . 47
3.10 MPG-2 with ion pump at different positions. . . . . 48
3.11 Measurements at Bad Homburg. . . . . 49
3.12 Measurement results – Bad Homburg. . . . . 49

4.1 Rotation of the falling body. . . . . 53
4.2 Eccentricity of the centre of mass in 3D space. . . . . 55
4.3 Falling body of the absolute gravimeter. . . . . 57
4.4 Coordinate measuring machine measures OC position. . . . . 57
4.5 Balancing setup. . . . . 58
4.6 Enhanced method to detect the imbalance. . . . . 59
4.7 Results of the imbalance measurements. . . . . 62
4.8 Imbalance of the mandrel without rotor. . . . . 71
4.9 Imbalance of the mandrel with rotor. . . . . 71
4.10 The imbalance of the mandrel is cancelled out. . . . . 72
4.11 The imbalance **E** due to the eccentricity. . . . . 73
4.12 The imbalance of the mandrel and the eccentricity are cancelled out. 73
4.13 Three rotation axes around which the FB will be balanced. . . . . 74
4.14 Falling body of the absolute gravimeter. . . . . 75
4.15 Mounting jig for balancing the FB. . . . . 75
4.16 Balancing machine BMT 200 S. . . . . 76
4.17 Results of the imbalance measurement. . . . . 79
4.18 Fabrication tolerances for the housing. . . . . 82

5.1 Gravitational attraction due to instrumental parts. . . . . 93
5.2 Beam verticality. . . . . 94

5.3 Verticality alignment. . . . . 95
5.4 Beam deviation angle. . . . . 96
5.5 Laser beam divergence. . . . . 99
5.6 Tilt of optical table. . . . . 102
5.7 Correlation between gravity values and temperature. . . . . 102
5.8 Ground vibration acceleration spectrum. . . . . 104
5.9 Single drop residuals of MPG-2 when Super Spring is locked. . . . 104
5.10 Residuals of a single drop with MPG-1 and MPG-2. . . . . 105
5.11 Synthetically generated drop. . . . . 106
5.12 Effective height. . . . . 110
5.13 Results of the phase response measurement of the amplifier. . . . 112

B.1 Results of the long term measurement #4 with MPG-1. . . . . 128
B.2 Power spectrum from MPG-1 measurement. . . . . 128
B.3 Results of the long term measurement #5 with MPG-1. . . . . 129
B.4 Measurements at ECAG 2007 in Walferdange/ Luxembourg with MPG-2. . . . . 130
B.5 Measurements at Bad Homburg. . . . . 130

# List of Tables


1.1 Gravitational influences. . . . . 2
1.2 Main tidal constituents. . . . . 11

2.1 Typical single drop parameters. . . . . 32

3.1 Measurement results – Bad Homburg. . . . . 48

4.1 Results of the COM to the OC adjustment. . . . . 62
4.2 Uncertainty budget of the measured imbalance – Method I. . . . . 68
4.3 Uncertainty budget: COM and OC adjusted – Method I. . . . . 69
4.4 The fitted values obtained with the enhanced method. . . . . 78
4.5 Results of the centre of mass to the optical centre adjustment. . . 80
4.6 Uncertainty budget of the measured imbalance – Method II. . . . 84
4.7 Uncertainty budget: COM and OC adjusted – Method II. . . . . 84

5.1 Uncertainty budget for air drag . . . . . 89
5.2 Uncertainty budget for outgassing . . . . . 90
5.3 Uncertainty budget for eddy currents . . . . . 91
5.4 Uncertainty budget for electrostatic field . . . . . 91
5.5 Uncertainty budget for instrumental masses . . . . . 94
5.6 Uncertainty budget for laser verticality . . . . . 96
5.7 Length standard specifications. . . . . 96
5.8 Uncertainty budget for laser stability . . . . . 97
5.9 Frequency standard specifications. . . . . 98
5.10 Uncertainty budget for clock stability . . . . . 98
5.11 Uncertainty budget for corner cube rotation . . . . . 98

5.12 Uncertainty budget for radiation pressure . . . . . 99
5.13 Uncertainty budget for beam divergence . . . . . 100
5.14 Uncertainty budget for temperature gradient . . . . . 101
5.15 Uncertainty budget for seismic noise . . . . . 107
5.16 Uncertainty budget for speed of light . . . . . 108
5.17 Uncertainty budget for effective height . . . . . 109
5.18 Specifications of Photoreceiver. . . . . 110
5.19 Uncertainty budget for amplifier . . . . . 111
5.20 Uncertainty budget for solid Earth tides . . . . . 113
5.21 Uncertainty budget for ocean loading . . . . . 113
5.22 Uncertainty budget for polar motion . . . . . 114
5.23 Uncertainty budget for environmental pressure . . . . . 115
5.24 Uncertainty budget for Coriolis force . . . . . 116
5.25 Uncertainty budget for MPG-1. . . . . 117
5.26 Uncertainty budget for MPG-2. . . . . 118

A.1 Physical constants and numbers. . . . . 126

# Chapter 1

# Introduction

By the end of the 16$^{\text{th}}$ century Galileo Galilei showed experimentally that the free-fall is a uniformly accelerated motion. He showed that bodies of different materials fall equal distances during equal times. In the 17$^{\text{th}}$ Sir Isaac Newton derived the law of motion of a freely falling body from the Keplerian laws of planetary motion. In the same century Christian Huygens developed the theory of the mathematical and physical pendulum. Thus two basic relations for the measurement of gravity have been established. The need for a measurement of the gravity was connected with the determination of the figure of the Earth. Over the years sophisticated pendulum methods were invented to measure the acceleration due to gravity (simply called "$g$,") and the pendulum methods were replaced by free-fall determination methods, in the 1950's. Today, this technique still represents the state-of-the-art.

Further applications arose with the absolute gravimeters' improving accuracy and resolution, and the measurement of $g$ has become indispensable today, even in many areas of daily life. Resolutions of 1 $\mu$Gal (=10 nm s$^{-2}$) are the state-of-the-art for absolute gravimeters - this corresponds to a resolution of height of about 0.3 cm. Navigation systems, for instance, became more precise with the increasing accuracy of the measurements, since the gravitational potential has to be known to determine the satellite positions accurately. Highly accurate maps of the Earth are based on these results, and the dimension of height is now defined through gravity. Gravimeters are used to monitor tectonic changes and to detect

mineral resources. Table 1.1 lists the orders of magnitudes of some influence factors, to give an idea of how precise today's gravimeters are.

Metrology is another field that benefits from absolute gravity determination.

**Table 1.1:** Orders of magnitudes of gravitational attraction on Earth's surface. (Data compiled from Niebauer *et al.* (1995); Peters *et al.* (1999); Torge (1989))

| Source | Magnitude/$\mu$Gal |
|---|---|
| Earth | 980 000 000 |
| Change due to gravity gradient /1 m | -300 |
| Solid Earth tides (Moon /Sun) | $\pm$150 |
| Ocean loading | $\pm$10 |
| Ground water level | $\pm$10 |
| Air mass (atmospheric pressure 0.3 $\mu$Gal/m) | $\pm$9 |
| Polar motion | $\pm$6 |
| Geodynamics (glacial rebound, tectonic motion) | $\pm$5 |
| Gravity field anomaly (due to minerals) | up to 10 000 |
| Human activity (construction, excavations) | $\pm$100 |
| Person of 70 kg weight at 0.5 m | 2 |

The redefinition of the "kg" requires a relative standard uncertainty in $g$ of $10^{-8}$ or better (Schwitz *et al.*, 2004). There are also plans to redefine the "Kelvin", which require an exact measurement of the Boltzmann constant, which in turn is based on the measurement of $g$. The Planck constant is a further candidate for a more highly accurate standardisation by the same principle as the kg. Finally, gravimeters can be used to determine the less accurately known fundamental physical constant $G$, Newton's gravitational constant, which is of high importance in many parts of physics.

Gravimetry is essential for the above reasons and additionally, in military applications and deposit exploration. However, the gravimeters still need to be improved to give higher resolution and accuracy, and they need to be miniaturised.

Chapter 1 presents a definition of gravity and a brief mathematical description of the gravitational influence of the Sun and Moon on the gravity values measured

on the Earth's surface. This is instructive, as gravity variations due to tidal influences can be nicely seen in our long term measurements.

## 1.1 Theory of gravity

The following will provide the terminology of gravity and derive the equation of motion of a freely falling test mass in a gravity field. The treatment is standard and can be found in many textbooks (e.g. Dehlinger, 1978; Hofmann-Wellenhof & Moritz, 2005; Lowrie, 1997; Seidelmann, 1992).

### 1.1.1 The figure of the Earth

The main objective of *geodesy* is to determine the figure of the Earth and its gravity field. There are many models for this figure. The simplest is a sphere, which is a good approximation of the actual shape of the Earth, as the Earth's flattening $f$ (defined as $f = (a - c)/a$ (cf. Appendix A for numbers), where $c$ is the polar radius, and $a$ the equatorial radius) is just $3.4 \times 10^{-3}$. However, this model was quickly superseded, as more complex models emerged. One is the *reference ellipsoid*, which is a close approximation to the equipotential surface of gravity, but at heart is just a mathematical convenience. Nowadays, the figure of the Earth is defined by the so called *geoid*. It is defined as one of the equipotential surfaces of the Earth's gravity potential. This potential coincides with the mean

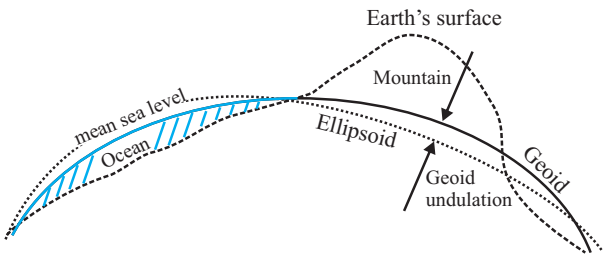


(a) The geoid surface coincides with the mean sea level. The geoid undulation is the displacement between the Geodetic Reference Ellipsoid and the geoid.

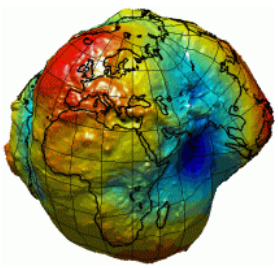

(b) The geoid.

**Figure 1.1:** Geoid and reference ellipsoid.

surface of the oceans. The difference between the reference ellipsoid and the geoid is called *geoid undulation*, and is sketched in Fig. 1.1(a). In fact, the deviation of the geoid from the best-fitting ellipsoid is quite small. The largest negative undulation of −105 m is in the Indian Ocean, and the largest positive undulation of +73 m is in the Pacific Ocean (Lowrie, 1997). Often a three dimensional map of the geoid is shown, like that in Fig. 1.1(b), to demonstrate that the gravitational shape of the Earth bears more similarity to a "potato" than a sphere, however one should note that such figures are exaggerated by many orders. As a result of this definition of the geoid, gravity enters into the geometry of the Earth. "Heights above sea level" are heights above the geoid (Hofmann-Wellenhof & Moritz, 2005). This brings up the question why the shape of the Earth is not just measured with GPS (Global Positioning System). Geocentric positions today can be measured to better than 0.1 m by means of GPS. The answer is that satellite orbits also follow potential surfaces, and this is where the gravity field comes in again.

### 1.1.2 Acceleration due to gravity

The potential of the geoid equals the gravity potential $W$ (also called geopotential) at mean sea level. $W$ is defined as the sum of the gravitational potential $V$, and the centrifugal potential $Z$ of the Earth:

$$W = V + Z = -\frac{GM}{r} + \frac{1}{2}\omega^2 r^2 \sin^2(\vartheta) \; . \tag{1.1}$$

Then the force due to gravity $\mathbf{F_g}$[1] is the sum of the gravitational force and the centrifugal force (cf. Fig. 1.2), and can be written as the gradient of the gravity potential:

$$\mathbf{F_g} = -\nabla W \; . \tag{1.2}$$

In geophysical applications, however, accelerations are more important than forces. Comparing Newton's law of motion

$$\mathbf{F} = m_i \mathbf{a} \; , \tag{1.3}$$

[1]Boldfaced letters denote vectors.

where $m_i$ denotes the *inertial mass* of the test mass $m$, and $\mathbf{a}$ its acceleration, with Newton's law of gravitation

$$\mathbf{F} = -\frac{Gm_gM}{r^3}\mathbf{r} \,, \tag{1.4}$$

where $m_g$ denotes the *gravitational mass* of the test mass $m$, $M$ the field generating mass, $G$ the Newtonian constant of gravitation, and $r = |\mathbf{r}|$ the distance between the centre of mass of the attracting mass $M$ and the test mass $m$, the gravitational acceleration $\mathbf{a_g}$ can be written as

$$\mathbf{a_g} = -\frac{GM}{r^3}\mathbf{r} \,, \tag{1.5}$$

for $m_i = m_g$. This equality has been proved to relative accuracies better than $9 \times 10^{-13}$, by Braginsky & Panov (1971) (cf. also Adelberger *et al.* (1990); Su *et al.* (1994)).

From the second potential of Equ. (1.1), the centrifugal potential, we can derive the centrifugal acceleration. To calculate the centrifugal acceleration we

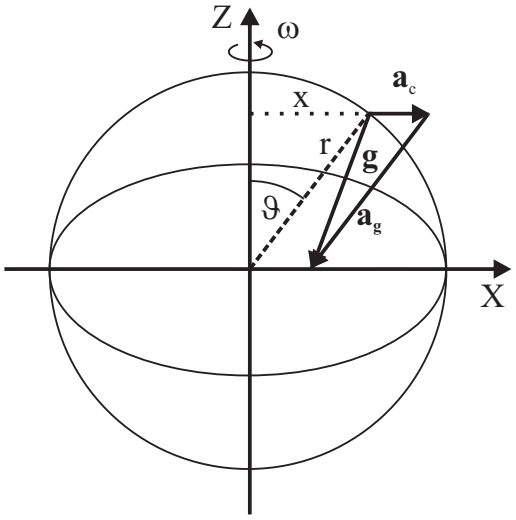


**Figure 1.2:** Gravity is the sum of gravitational force and centrifugal force. The direction of $\mathbf{g}$ depends on the combination of centrifugal acceleration $\mathbf{a_c}$ and gravitational acceleration $\mathbf{a_g}$ at each point.

can write (cf. Fig. 1.2)

$$\begin{aligned} \mathbf{a_c} &= \omega^2 x \frac{\mathbf{x}}{x} \ , \quad \text{or} \\ \mathbf{a_c} &= \omega^2 r \sin\vartheta \, \frac{\mathbf{x}}{x} \ . \end{aligned} \tag{1.6}$$

Here $\vartheta$ is the polar angle describing the angle between the axis of rotation and the the position vector in an earthbound system with the origin of the coordinate system coinciding with the centre of the Earth. From Fig. 1.2 we see that the forces add to the resultant force of gravity $\mathbf{g}$ (divided by unit mass). The direction of $\mathbf{g}$ coincides with the plumb line and is perpendicular to the geoid's surface at each point.

Let us define a local coordinate system in a way that its positive $z$-direction coincides with the gravity vector $\mathbf{g}$. If we now assume a constant angular velocity $\omega$ and a homogeneous gravitational field, the resultant acceleration due to gravity will be

$$|\mathbf{g}| = |\mathbf{a_g} + \mathbf{a_c}| = g = \text{constant} \ . \tag{1.7}$$

Thus, the equation of free fall motion we get by integrating twice will have the form

$$z(t) = z_0 + v_0 t + \frac{g}{2} t^2 \ , \tag{1.8}$$

where $z_0$ is the position, and $v_0$ the velocity of the test mass at the time $t = 0$. Equation (1.8) is the form of the equation of motion we will use later for our data analysis.

In high-precision measurements, however, the gradient cannot be neglected, as the acceleration due to gravity changes by $\approx 300$ $\mu$Gal m$^{-1}$ (1 $\mu$Gal$=$ 10 nm s$^{-2}$). We will now include it in the equation of motion. For simplification, but still in a good approximation, we assume the change in gravity with height to be linear, so that we can write for the *gravity gradient* $\gamma(z) = dg(z)/dz = \gamma_0 \, z$, where $\gamma_0$ is a constant. Then the gravity is given by

$$\ddot{z} = g(z) = g_0 + \gamma_0 \, z \ , \tag{1.9}$$

the solution of which is (Cook, 1965):

$$z(t) = \frac{g_0}{\gamma_0} \Big( \cosh\left(\sqrt{\gamma_0} \, t\right) - 1 \Big) \ , \tag{1.10}$$

where we set $z_0 = 0$ and $v_0 = 0$, and $\ddot{z} = \frac{d^2z}{dt^2}$. The cosh can be expanded in a Taylor series, which gives

$$z(t) = \frac{g_0}{2}\left(t^2 + \frac{\gamma_0 t^4}{12}\right) , \tag{1.11}$$

neglecting higher order terms. This shows that by neglecting the gradient, the height to which the gravity value is referred, is no longer $z|_{t=0}$, but instead refers to a position $z|_{t>0}$. The height the calculated $g$-value refers to in the presence of a gravity gradient will be calculated later (Sec. 5.1.14).

### 1.1.3 Tides

The problem of tide calculations is a fascinating, albeit also a very complex subject. The variations measured in the $g$-value not only contain the lunar-solar attraction, but also secondary effects, such as deformation of the solid earth and ocean tides, which are the manifestations of the sea to keep its surface perpendicular to the gravity vector. Because of the deformation of the Earth, gravity measurements are also influenced by changes of the Earth's radius, which can reach up to 56 cm (Dehlinger, 1978).

Fortunately, astronomy has a long tradition, allowing the times and positions of the Sun and Moon to be calculated to considerable precision, as the basis for calculating tidal corrections can thus be calculated that can easily be applied to measured gravity data.

The following will show a method of calculating the lunar tidal attraction. The solar tidal attraction is calculated in a similar way.

Let us start with the Moon's potential on the Earth's surface (cf. Fig. 1.3):

$$V_M = \frac{GM_M}{r_1} , \tag{1.12}$$

where $G$ is the Newtonian constant of gravitation and $M_M$ is the Moon's mass. Furthermore, we have the relation

$$r_1^2 = r^2 + R^2 - 2rR\cos(\varphi) , \tag{1.13}$$

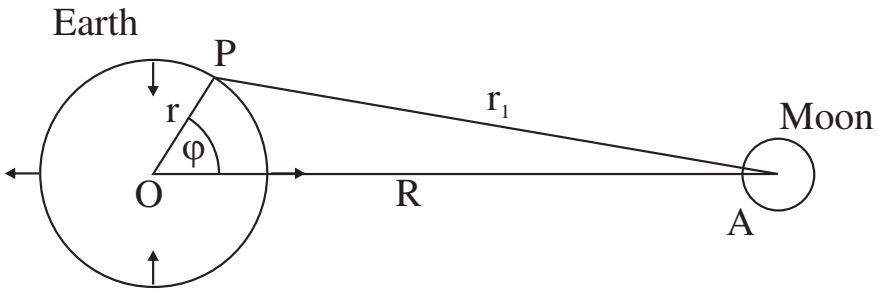


**Figure 1.3:** Illustration of the lunar attraction on a point $P$ on the Earth's surface. $R$ determines the distance between the centre of mass of the Earth $O$ and the centre of mass of the Moon $A$. The Earth's radius is given by $r$, and $r_1$ is the distance from the Moon's centre of mass to the point $P$ on the Earth's surface. The zenith angle w.r.t. the centre of the Earth is given by $\varphi$. The arrows indicate the tidal forces acting on the Earth.

where $\varphi$ describes the zenith angle in a reference system bound to the Earth's centre. Inserting (1.13) in (1.12) gives

$$V_M = \frac{GM_M}{R}\left[1 - 2\left(\frac{r}{R}\right)\cos(\varphi) + \left(\frac{r}{R}\right)^{1/2}\right]^{-1/2} . \tag{1.14}$$

In the case of the Earth and Moon $r/R \approx 1/60$. Therefore, we can expand the right hand side of (1.14) in a Taylor series in terms of $r/R$ and obtain

$$V_M = \frac{GM_M}{R} + \frac{GM_M}{R}\left(\frac{r}{R}\right)\cos(\varphi) + \frac{GM_M}{R}\left(\frac{r}{R}\right)^2\left(\frac{1}{2}\right)\left(3\cos^2(\varphi) - 1\right) + \cdots . \tag{1.15}$$

This can be regarded as a sum of different potentials. The tidal forces are calculated from the gradient of the potential. The first term in (1.15) is a constant and, hence, does not produce any force.

The second term in (1.15) is linear in $r$ and thus produces a constant force, namely the one which keeps the Earth in its orbit around the centre of mass of the Earth-Moon system.

The third term is the most interesting of the three. Assuming that higher order terms are neglected in (1.15), it is the third term that produces tides. The tide-generating potential can thus be written as

$$V_{Tide} = \frac{GM_M r^2}{2R^3}\Big(3\cos^2(\varphi) - 1\Big) . \tag{1.16}$$

The vertical component of the attractive force per unit mass can easily be calculated from the potential (1.16):

$$(g_\perp)_M = -\frac{\partial V_{Tide}}{\partial r} = -\frac{GM_M r}{R^3}\Big(3\cos^2(\varphi) - 1\Big) \; . \tag{1.17}$$

The subscript $\perp$ shall denote the fact that this component of force acts perpendicular to the sea level. For the sake of completeness we will give the component parallel to the sea level:

$$(g_\parallel)_M = -\frac{1}{r}\frac{\partial V_M}{\partial \varphi} = -\frac{3GM_M r}{R^3}\Big(\sin(\varphi)\cos(\varphi)\Big) \; . \tag{1.18}$$

The same calculation can be performed for the Sun's attraction. Although the Sun's mass is much larger than the Moon's, its distance to the Earth is also greater, and it can be shown that the ratio between the Sun's and Moon's attractions is $g_S/g_M = 0.46$, where $g_S$ denotes the acceleration due to the Sun. The influence of other planets is so small (5 orders less in the case of Jupiter!) that they can safely be ignored.

By inserting into equation (1.17) the values for $G$, $R$, $M_M$, and $r$ (= Earth's equatorial radius $a$; cf. Appendix A), we obtain as a maximum acceleration due to the Moon's gravitation $[(g_\perp)_M]_{max} = -109.7$ $\mu$Gal, and as a minimum value $[(g_\perp)_M]_{min} = 54.8$ $\mu$Gal. The respective values for the Sun are $[(g_\perp)_S]_{max} = -50.5$ $\mu$Gal, and $[(g_\perp)_S]_{min} = 25.3$ $\mu$Gal. When the Sun and Moon are in line with the Earth (and on the same side), the tidal attraction superposes to give a maximum value of 240 $\mu$Gal. If we also consider the variation due to the deformation of the Earth, it can be shown (Dehlinger, 1978) that these effects reach magnitudes of up to 40 $\mu$Gal, the maximum variation in gravity therefore summing up to 300 $\mu$Gal.

Now, let us consider the temporal variation of tidal attraction on a point $P$ on the Earth's surface. It turnes out to be inconvenient to describe the Moon's position with respect to this point $P$ in terms of the zenith angle $\varphi$. Therefore, we introduce a geocentric reference system (cf. Fig. 1.4) where the Moon's position can be described by its astronomic latitude $\phi$, its declination north of the equatorial plane $\delta$, and its hour angle $\tau$. The hour angle defines the longitude of the Moon where the plane described by the Earth's rotating axis and the Moon

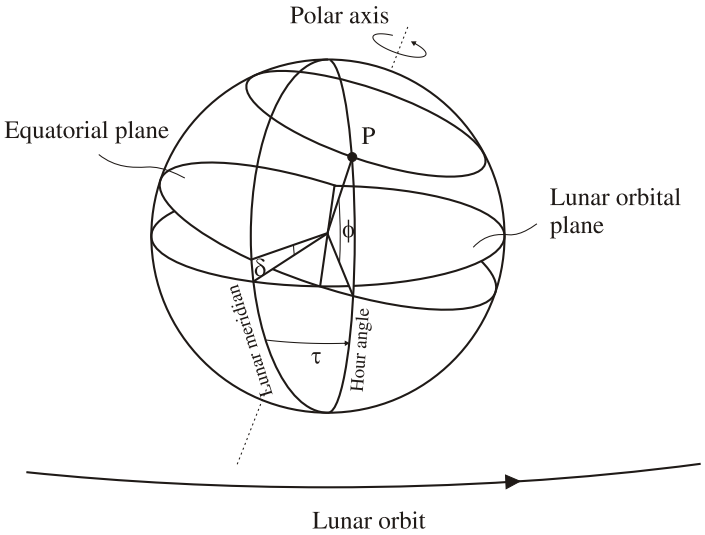


**Figure 1.4:** Instead of the zenith angle $\varphi$ latitude $\phi$, declination $\delta$ and hour angle $\tau$ can be introduced.

crosses the equator. The transformation is done with the following equation, known from spherical trigonometry (Dehlinger, 1978):

$$\cos(\varphi) = \sin(\phi)\sin(\delta) + \cos(\phi)\cos(\delta)\cos(\tau)\ . \tag{1.19}$$

By substituting (1.19) into (1.16) we get:

$$V_M = \frac{GM_M r^2}{R^3}\frac{1}{4}\Big[\big(3\sin^2(\phi)-1\big)\big(3\sin^2(\delta)-1\big) + 3\sin(2\phi)\sin(2\delta)\cos(\tau) + 3\cos^2(\phi)\cos^2(\delta)\cos(2\tau)\Big]\ . \tag{1.20}$$

The quantities $\phi$, $\delta$ and $\tau$ change with different periods. Doodson (1921) proposed a Fourier series expansion in order to group the tidal signal into components by frequencies and spacial variability. According to Doodson, each component has a frequency

$$f = \sum_{\mathrm{i}=1}^{6} n_{\mathrm{i}}\, f_{\mathrm{i}}\ . \tag{1.21}$$

The numbers $n_{\mathrm{i}}$ are integer numbers with $n_1$ ranging from 1 to 3, and $n_{2,\ldots,6}$ taking values ranging from -5 to +5. In order to avoid negative numbers for

the values $n_{2,\ldots,6}$, Doodson added 5 to each of these numbers. As a result, we can classify the tidal constituents into groups of *semi diurnal*, *diurnal*, and *long periodic* frequencies. The main tidal components are shown in the following table 1.2 (adopted from Dehlinger (1978)). Doodson included almost 400 constituents

**Table 1.2:** Main tidal constituents. The subscripts, like $M_2$, refer to the number of cycles per day. The letters are called Darwin's symbols (after Darwin, G.H.) and often denote the origin of the constituent.

| | Symbol | Tidal component | Period |
|---|---|---|---|
| Semi diurnal | $M_2$ | Principal lunar | 12.42 h |
| $n_1 = 2$ | $S_2$ | Principal solar | 12.00 h |
| | $N_2$ | Lunar ellipticity (due to monthly variation in the moon's distance) | 12.66 h |
| | $K_2$ | Lunar-solar declination | 11.97 h |
| Diurnal | $O_1$ | Principal lunar | 25.82 h |
| $n_1 = 1$ | $P_1$ | Principal solar | 24.07 h |
| | $K_1$ | Lunar-solar declination | 23.93 h |
| Long period | $M_0$ | Lunar flattening | 13.66 days |
| $n_1 = 0$ | $S_0$ | Solar flattening | 182.5 days |

in his expansion. 100 of them are long periodic.

The theoretical tidal accelerations can be calculated from the tide-generating potential derived above. Longman (1959) did this as early as 1959 for an IBM 709 computer. Nowadays, the most popular program is called ETERNA. It was developed by Wenzel (1996b). Today's programs also include secondary tidal effects. (To show how those effects are calculated is outside the scope of this thesis, and the interested reader is encouraged to look up e.g. Dehlinger (1978), Lambeck (1980), or Seidelmann (1992).)

Figures 1.5 and 1.6 show the theoretical tides and the amplitude spectrum, respectively, for the site *Erlangen* calculated with the program TSoft (van Camp & Vauterin, 2005).

## 1.2 Absolute measurement of gravity

With an absolute gravimeter the absolute value of gravity acceleration can be measured. In contrast, relative gravimeters are for measuring the difference of

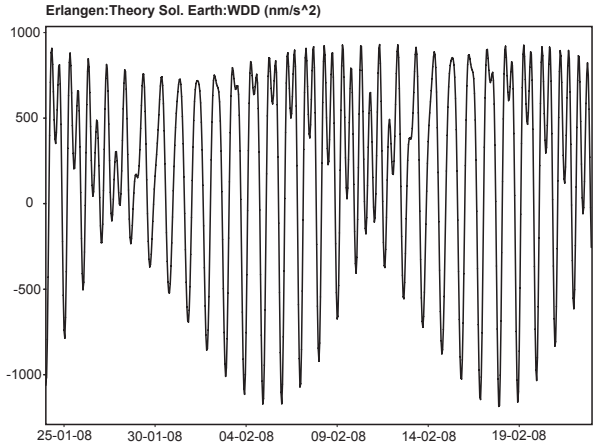


**Figure 1.5:** The figure shows the temporal variations in the gravity value for the site *Erlangen* (49.34°N, 11.00°E, elevation 287.0 m). The values are calculated with the program *TSoft*. Start 24-01-2008, duration 30 days. The amplitude is given in nm $s^{-2}$.

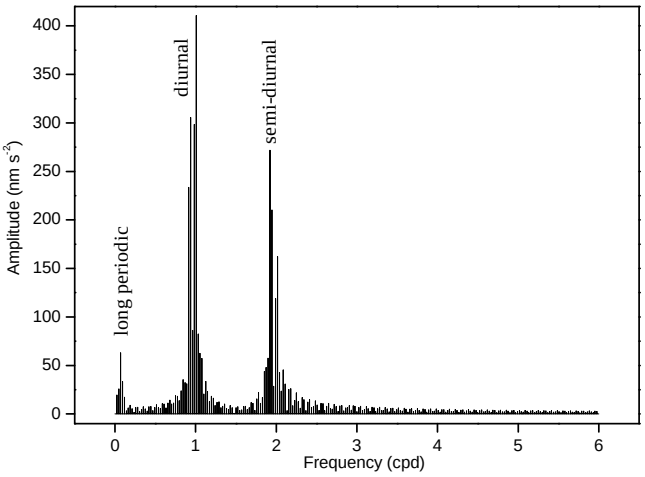


**Figure 1.6:** The amplitude spectrum of the tidal influences is calculated for *Erlangen*, with the program *TSoft*. The horizontal axis shows the cycles per day which correspond to the Doodson-numbers $n_1$ in table 1.2. The main tidal constituents can clearly be seen.

two gravity values, and need to be calibrated using an absolute gravimeter.

### 1.2.1 Historical Background

The investigation of gravity started with the development of the theoretical description of the *free fall motion* by Sir Isaac Newton (1643-1727) in his "Philosophiae Naturalis Principia Mathematica", published in 1687, and with the description of the *motion of the pendulum* by Christian Huygens (1629-1695).

For a long time ($\approx$ 200 years) the pendulum was the only apparatus for measuring gravity. Although the pendulum (patented by Christian Huygens in 1657) was originally invented to measure time, it soon became evident that the oscillation period depended on the latitude and on the height (above sea level). The pendulums used were mostly simple approximations of the mathematical pendulum. The breakthrough in accuracy came in 1818 with Kater's reversible pendulum (Cook, 1965). Who really invented the reversible pendulum is not clear (Kühnen & Furtwängler, 1906). A reversible pendulum was also used by Kühnen & Furtwängler (1906) who measured $g$ at the "Königliches Geodätisches Institut Potsdam" in Germany. This measurement was a key event in Germany's geodetical history, as this value 1909 became the global gravity reference (Dehlinger, 1978) for a period of more than 50 years, which ended with the advent of free fall measurements, as these turned out to be more accurate.

The epoch of free fall gravimeters started with the proposals by Guillet, and by Volet in 1946 (Cook, 1965). In 1952 Volet conducted a first measurement with a falling graduated scale and high speed photography. Later free fall experiments were performed by Agaletzkij *et al.* (1959) in Leningrad, Russia, Preston-Thomas et al. (1960) in Ottawa, Canada, Thulin (1961) in Sèvres (Paris), France, and Faller (1965) in Princeton, New Jersey, USA. In 1967 Cook built the first symmetric free fall gravimeter, where a glass ball was launched upward and fell back under the force of gravity. Sakuma improved this design in 1971 in Sèvres, France, by applying optical (white light) interferometry for the length measurement (Faller was the first contemporary with him to do this). By the end of the seventies a Ukrainian group started a series of rise-and-fall gravimeters (Bondarenko *et al.*, 1997). Under the supervision of Faller, Niebauer (1987) launched the first serial

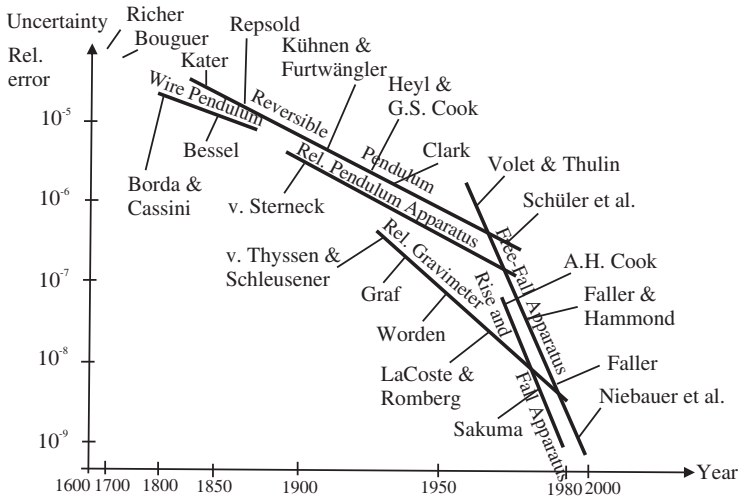


**Figure 1.7:** Historical overview of the gravimeter's increasing accuracy.

production of absolute free fall gravimeters (JILAG). The "new generation of absolute gravimeters" (Niebauer *et al.*, 1995) named *FG5* was an improvement of the *JILAG*. They were the first commercially available gravimeters on the market, sold by the company AXIS (now MicroG-LaCoste).

Finally, Kasevich & Chu (1991) succeeded in the first measurement of gravitational acceleration with a gravimeter based on an atom interferometer (cf. Baudon *et al.*, 1999). Despite the sophisticated setup, the atom gravimeter is still a free fall gravimeter, with the difference that the falling body is now microscopic, rather then macroscopic objects, namely atoms, which obey the same law of gravitation.

Figure 1.7, adopted from Torge (1989), illustrates the historical development in terms of accuracy of absolute gravimeters.

## 1.2.2 Free fall gravimeters

### 1.2.2.1 Free fall

Nowadays, the most common ballistic gravimeter is the simple free fall gravimeter. This type of gravimeter uses a macroscopic object as a test body.

The operating principle of a free fall gravimeter is quite simple. A test

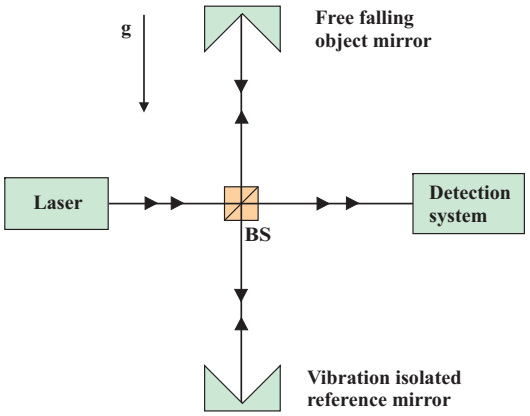


**Figure 1.8:** Working principle of a Michelson interferometer in a free fall gravimeter. The object mirror (falling mirror) is attached to the test mass. During the drop the change in path length with respect to the reference mirror is measured. (BS = beam splitter)

body, to which a triple mirror retro-reflector is attached, functions as an object mirror in a Michelson-type interferometer (cf. Fig. 1.8). The reference mirror is attached to a long period seismometer (D'Agostino, 2005) or an active vibro-isolation (Rinker, 1983) and defines a quasi-inertial reference system which the movement of the test body is referred to. Due to the path length change, which occurs when dropping the test mass, a chirped fringe signal (interferences of the reference beam and object beam) is generated on the detector over a frequency range from DC - 6 MHz, for a 200 ms drop (cf. Fig. 1.9). By measuring the time when the zero crossings of the fringe signal occur, the trajectory can be described (displacement in function of time). Each zero crossing equals a spacial displacement of $\lambda/4$, where $\lambda$ is the laser wavelength (usually a Helium-Neon laser with $\lambda = 633$ nm). With a least squares fitting of the equation of motion (e.g. equation 1.8) to the obtained trajectory, the parameters $g$ (acceleration due to gravity), $v_0$ (velocity at $t = 0$) and $z_0$ (position at $t = 0$) of the equation of motion can be derived.

Modern gravimeters reach accuracies of the order of 1-2$\times 10^{-9}$ (Niebauer *et al.*, 1995). Therefore relative uncertainties of $1 \times 10^{-9}$ and $5 \times 10^{-10}$ have to

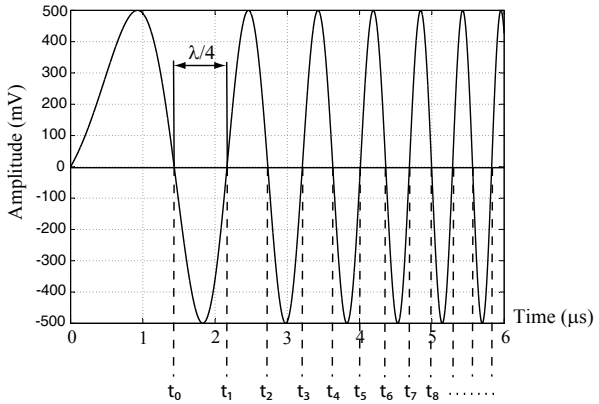


**Figure 1.9:** The interference signal generated due to the dropped mirror is a chirped sine wave, which ranges from approximately DC to about 6 MHz for a 200 ms drop. Each zero crossing signifies a relative translation of $\lambda/4$, where $\lambda$ denotes the laser wavelength.

be reached for the displacement and the time interval measurement, respectively. This is only possible due to the invention of stabilized lasers and due to atomic clocks, as well as the invention of the corner cube retroreflectors (Peck, 1948).

#### 1.2.2.2 Symmetric free fall - Rise and fall

The operation principle of the symmetric free fall (also rise and fall) gravimeter, which was first built by Cook in 1967, is essentially the same as that of the simple free fall gravimeter, with the difference that the test body is launched upwards rather than just dropped. So the movements upwards and downwards are tracked and processed. The data acquisition is similar to that of simple free fall gravimeters.

The advantages of this type of gravimeters are that the trajectory is longer (up to 400 ms (D'Agostino, 2005)) – this reduces the error due to seismic noise – and the gravimeter is less sensitive to air drag and non-homogeneous electrical and magnetic fields, but more difficult to align. As the test body is launched, it can have a horizontal velocity component, which introduces an error due to the Coriolis effect. This error is one of the biggest contributions to the uncertainty

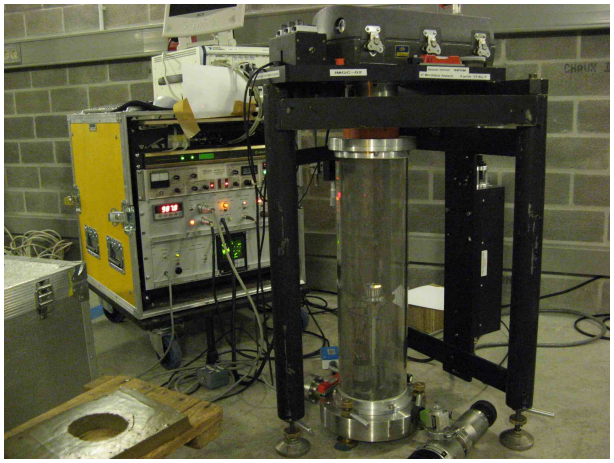

**Figure 1.10:** The picture shows the rise and fall gravimeter IMGC#2 of the Institute of Metrology G. Colonnetti, Italy, at the international comparison of absolute gravimeters in Walferdange, Luxembourg, November 2007.

budget of a rise and fall gravimeter (D'Agostino, 2005). Figure 1.10 shows an example of a symmetric free fall gravimeter.

### 1.2.3 Atom gravimeters

Basically, atom gravimeters are free fall gravimeters, with the difference that atoms are dropped instead of macroscopic objects. The principle is basically laser ranging of atoms, where the position information is encoded into the atomic wavefunction. This type of gravimeter is based on atomic interferometry (Baudon *et al.*, 1999). The first atom gravimeter was realized by Kasevich & Chu (1991). However, its accuracy was quite poor. With an improved gravimeter, they reached an accuracy of $3 \times 10^{-9}$ (Peters *et al.*, 1999). Although the dropping chamber can already be built quite compact, the electronics are very bulky (cf. Fig. 1.11), making real portable gravimeters infeasible. The considerable costs are another disadvantage. On top of this, atom gravimeters suffer from the same sensitivity of the reference mirror to seismic noise as the simple free fall gravimeters.

**Figure 1.11:** Atom gravimeter from ONERA. Although the set-up is compact, the electronics is bulky.

## 1.3 Selected applications

There are many applications for gravimeters. One of the main applications is surely the determination of the geoid, i.e. geodesy, and with it cartography, which needs gravity data for the height determination. But there are a variety of applications that indirectly require the value of gravitational acceleration. These are metrology, physical sciences, and geophysics, among others. The following will report on some selected applications.

### 1.3.1 New definition of the Kelvin

Up to this date, the triple point of water (TPW) is used to define the unit of temperature $T$. This means that the temperature is linked to a material property. Recently, there was a proposal for a new definition of the Kelvin, namely via the Boltzmann constant $k_B$ (Fischer *et al.*, 2007). However, the current uncertainty, with the temperature linked to the TPW, is $3 \times 10^{-7}$, whereas the

uncertainty of the Boltzmann constant is $10^{-6}$. For a redefinition of the Kelvin, the new definition's uncertainty should equal or exceed the old definition's. The most promising of the proposed measurement methods is dielectric-constant gas thermometry (DCGT). The idea is basically to replace the density in the equation of state of a gas by the dielectric constant $\varepsilon$. This constant is then measured via a capacitor, which is placed in the gas bulb. The equation of measurement is obtained by stipulating that

$$R = k_B N_A \ ,$$

where $R$ is the molar gas constant, $k_B$ is the Boltzmann constant, and $N_A$ is the Avogadro constant. The molar polarizability $A_\varepsilon$, defined as

$$A_\varepsilon = \frac{N_A \alpha_0}{3\varepsilon_0} \ ,$$

contains the static electric dipole polarizability $\alpha_0$, and the exactly known electric constant $\varepsilon_0$. Combining both equations results in

$$k_B = \frac{R\alpha_0}{A_\varepsilon 3\varepsilon_0} \ .$$

Finally, performed *ab initio* calculations (Fellmuth *et al.*, 2006) gave exactly the static electric dipole polarizability of the $1^1$S ground state of the $^4$He atom in the $^4$He reduced atomic unit of polarizability

$$\alpha_0^*(^4\mathrm{He}) = \frac{\alpha_0(^4\mathrm{He})}{(4\pi\varepsilon_0 a_0^3(1 + m_e/m_\alpha)^3)} \ ,$$

where $a_0$ is the Bohr radius and $m_e/m_\alpha$ is the electron to $\alpha$ particle mass ratio. Thus, the final measurement equation for $k_B$ becomes

$$k_B = \frac{4\pi}{3} a_0^3 \left(1 + \frac{m_e}{m_\alpha}\right)^3 \frac{\alpha_0^*(^4\mathrm{He})}{(A_\varepsilon/R)_{^4\mathrm{He}}} \ .$$

The need for the acceleration due to gravity $g$ enters here via the measurement of pressure. By combining the virial expression of the equation of state of a real gas and the Clausius-Mosotti equation, the pressure $p$ can be approximated as

$$p \approx \frac{\chi}{(3A_\varepsilon/RT) + \kappa_{eff}} \left[1 + \frac{B(T)}{3A_\varepsilon}\chi + \frac{C(T)}{(3A_\varepsilon)^2}\chi^2 + \cdots\right] \ ,$$

with $\chi = \varepsilon/\varepsilon_0 - 1$ as the dielectric susceptibility and $\kappa_{eff}$ as the effective compressibility. $B(T)$ and $C(T)$ are the second and third density virial coefficients, respectively. For different pressures $p$ of the gas-filled capacitor, the relative change in capacitance is measured, which finally determines $3A_\varepsilon/RT$. This measurement, however, requires an exact pressure determination, which demands a knowledge of the gravitational acceleration to accuracies of better than $1 \times 10^{-7}$ (Sabuga, 2007).

### 1.3.2 New definition of the kilogram

Of the seven units of measurement in the International System (SI), the kilogram is the only unit still defined by an artefact standard. It recently also became evident that the kilogram (based on the International Prototype Kilogram (IPK), a bar of platinum-iridium alloy made in the 1880's and kept in a vault near Paris) is loosing weight. Many international scientists believe it is time to redefine it (Walker, 2004). Among other proposals to redefine the kilogram based on a fundamental constant (Schwitz *et al.*, 2004; Wignall, 2005), one idea is to relate mechanical to electrical power via the so called moving-coil watt balance, first suggested by Kibble (1976) (cf. also Kibble *et al.* (1990)). This is done as follows (Fig. 1.12). On one side of a balance the gravitational force on a mass $m$ in the

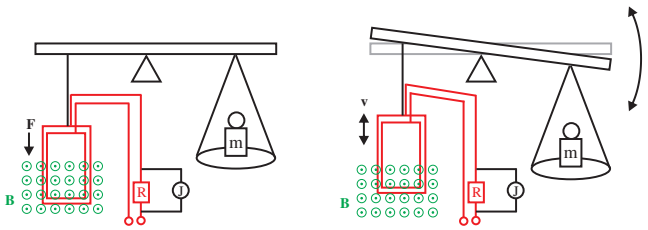


**Figure 1.12:** With the moving-coil watt balance mechanical force is compared to electrical force.

Earth's gravitational field is measured, where the acceleration due to gravity $g$ has to be known. This force is compared to the electromagnetic force acting on a coil of the length $l$ in a magnetic field $B$ when a current $I$ flows through it.

When the balance is in equilibrium, we have

$$I(Bl) = mg \ .$$

In a further step of the experiment the coil is moved with the velocity $v$ through the magnetic field $B$. The induced voltage $U$ gives

$$U = v(Bl) \ .$$

Combining both equations, for the site of measurement the following equation results:

$$UI = mgv \ .$$

The electrical power is determined by means of the Quantum-Hall-effect and the Josephson-effect:

$$P = UI = kf_J^2 h \ ,$$

where $f_J$ is the Josephson-frequency of the microwaves (typically about 70 GHz), radiating onto the Josephson-element, $h$ is Planck's constant, and $k$ is a calibration constant. The final result is for the mass

$$m = kf_J^2 h \frac{1}{gv} \ .$$

Hence, by means of this balance the kilogram will be traced back to electrical power, which can be measured very accurately through the Josephson effect and the quantum Hall effect. To convert the weight, which is measured with such a balance, into kilograms, the gravitational acceleration $g$ needs to be known. The accuracy of a new mass presentation should be better than $10^{-8}$ (Schwitz *et al.*, 2004).

### 1.3.3 Measurement of the Planck constant

The same moving-coil watt balance can also be used to measure the Planck constant to higher accuracy (Williams (1998); also see Eichenberger *et al.* (2003); Robinson & Kibble (2007); Steiner *et al.* (2005)). Here again the knowledge of $g$ is necessary, and the mass $m$ has to be known, as well. The current relative standard uncertainty for the Planck constant is $5 \times 10^{-8}$ (NIST).

### 1.3.4 Measurement of the Newtonian constant

Newtonian constant of gravitation, $G$, is determined with the least accuracy ($1.5 \times 10^{-4}$). This is because of tremendous experimental difficulties. Henry Cavendish performed the first measurement to determine $G$, in 1798, with a torsion balance, invented in 1777 by Charles-Augustin de Coulomb, and independently by John Michell, in 1783 (Jungnickel & McCormmach, 1996). Later measurements were mainly based on the same principle. However, to reveal systematic errors, it is helpful to have different kinds of measurement principles to measure the same quantity. Schwarz and collaborators (Schwarz, 1998; Schwarz *et al.*, 1998) were finally able to measure $G$ using a free fall gravimeter. They determined $G$ by differential measurement, locating a huge test mass ($\approx 500$ kg) close to the gravimeter at subsequently different positions. The achieved relative accuracy was $1.4 \times 10^{-3}$. Fixler *et al.* (2007) performed a similar experiment with an atom interferometer. Systematic uncertainties limited the experiment to an accuracy of 3 ‰.

### 1.3.5 Time keeping

In a recent article Kleppner (2008) reported the latest achievements in time standard (Ludlow *et al.*, 2008; Rosenband *et al.*, 2008). An overall uncertainty of $5.2 \times 10^{-17}$ could be reached. At this level of accuracy, a general relativistic effect had to be included in the uncertainty budget. The uncertainty contribution of $1 \times 10^{-18}$ arises from the potential difference, which corresponds to a height difference of 1 cm. Kleppner concludes that "the effects of general relativity that mix time with gravity are starting to approach a point that will require rethinking the basic concept of 'keeping time' ". Modern gravimeters, however, can resolve the potential difference surging from height differences, to better than 1 cm. Gravimeters, hence, could contribute to time measurement.

## 1.4 Organization of the thesis

This chapter briefly introduced the reader to gravimetry, showed how theoretical tides can be calculated, and gave some selected applications. Also a historical

overview of absolute gravity measurement was given and the working principles of current free fall gravimeters were sketched.

The following Chapters 2 and 3 are dedicated to the gravimeter set ups, developed during the thesis. The mechanics and optics of the stationary, as well as of the portable gravimeter will be explained, and results will be discussed.

Two novel methods to balance the falling body will be described in-depth in Chapter 4.

Before concluding with a summary and outlook in Chapter 6, the uncertainty budgets for both gravimeters are given in detail in Chapter 5.

# Chapter 2

# Stationary free fall gravimeter MPG-1

This chapter presents the setup of the stationary free fall gravimeter (MPG-1) and its operation principle. The mechanical, optical and electronics parts are described. Results from long-term measurements are shown and discussed, as well.

## 2.1 Setup

In Fig. 2.1 the schematic of MPG-1 (abbreviated from *Max Planck Gravimeter*) (a), and the laboratory setup (b) are shown. The whole measurement apparatus can be divided into three principal parts. (1) The ballistic block, with the mechanics and falling body; (2) the laser interferometer with the quasi-inertial reference mirror; (3) the electronics and computer for data acquisition and processing. As the figure illustrates, the ballistic block (dropping chamber) is placed on an optical table. The interferometer is mounted on top of the table except for the quasi-inertial reference mirror, in this case a Super Spring (Rinker, 1983), which is also used in the commercial FG5 absolute gravimeters from MicroG-LaCoste. The Super Spring is placed on the laboratory floor beneath a 30 cm $\times$ 30 cm hole in the optical table, so it is not visible in the top view photograph in Fig. 2.1(b).

a)

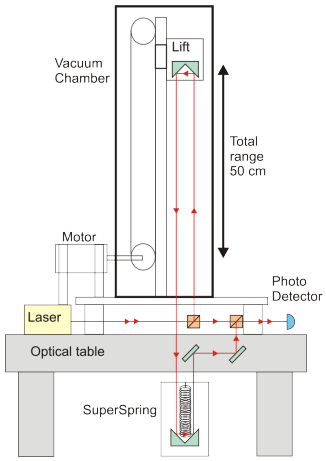


b)

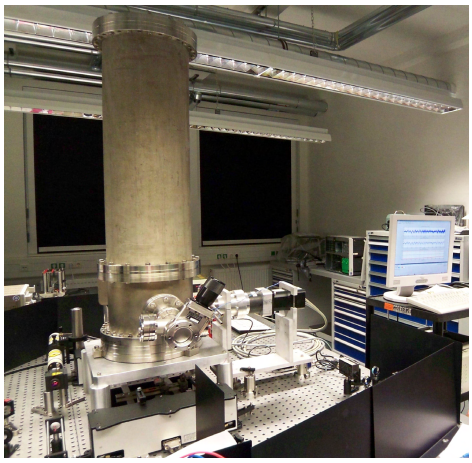

**Figure 2.1:** Set up of the stationary gravimeter MPG-1. a) The schematic of the measurement apparatus. b) The set up in the laboratory at Erlangen.

### 2.1.1 Optics and laser

The falling body's free fall is traced with a Michelson type interferometer (2.2). The object mirror, which is part of the falling body (FB), and the reference mirror, which is part of the Super Spring, are not physically connected to the rest of the interferometer. This main block of the interferometer consists of two non-polarizing beam splitters (BS) and two mirrors (M). The design of the interferometer is chosen so that a vertical displacement of the main block does not introduce any change in path length (in-line interferometer system; cf. Niebauer *et al.* (1995)). Only horizontal movements can alter the measurement, but those movements are assumed to be small. The laser light emitted from a Helium-Neon laser is expanded from 2 mm to 5 mm by means of a telescope. It is then split into two beams by a non-polarizing beam splitter BS1. The reference beam (which has to be aligned along $g$) is reflected from the free falling object mirror CCM1 to the vibration isolated reference mirror CCM2, deflected by mirrors M1 and M2, to finally recombine at beam splitter BS2 with the reference beam. By means of a third lens L3, the interfering beams are focussed on the detector.

As a laser, a polarisation-stabilized (Spectra Physics[1], A117), with a wavelength of 633 nm, is used (for specifications see table 5.7). The beam splitters

[1]Sold by Newport

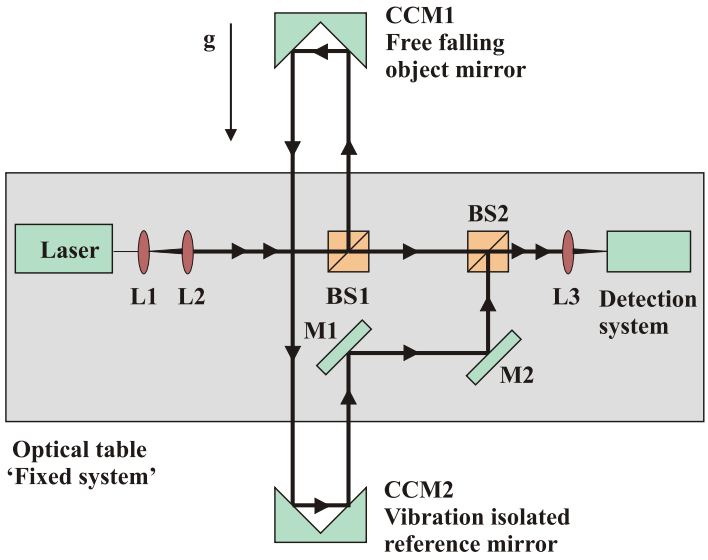


**Figure 2.2:** Interferometer setup. A Michelson-type interferometer is chosen. The free falling corner cube mirror (CCM1) and the reference mirror (CCM2), isolated by the Super Spring, are not mechanically connected to the non-polarizing beam splitters (BS1,2), the two mirrors (M1,2), and the two lenses (L1,2).

and the mirrors are commercially available and have surface qualities of better than $\lambda/10$.

### 2.1.2 Electronics

One of the new features of our setup is that the whole fringe signal (with up to 1.6 million data points) is digitized and processed. In other gravimeters usually just parts of the fringe signal are used for data processing. Since the duration of our FB's fall in the MPG-1 is about 200 ms, the resultant signal reaches a frequency of up to 6.2 MHz. As an industry standard, a sampling rate of at least 7 times the measured frequency is suggested. This means that the sampling rate of the digitizing card should be a minimum 50 MHz. We use a high performance digitizing PCI card (Gage Applied, CS 12400) capable of sampling up to 400 MS $s^{-1}$. Usually, a sampling rate of 100 MS $s^{-1}$ is taken. The ADC card has

512 MB onboard memory, with a 12 bit amplitude resolution, and is built into an industrial computer with a Pentium IV processor (3 GHz), with 2 GB of RAM running under Microsoft Windows XP.

Since the sampling frequency gives the time scale of the tracked falling body, the sampling time has to be referenced to a time standard. This is done by connecting an external (atomic) clock to the digitizing card, in our case a rubidium time standard (SRS, FS725).

To trigger the digitizer, a special *frequency trigger* was built at our institute. This frequency trigger gives a TTL pulse when the signal frequency reaches 1 MHz, i.e. a pure free fall of $\approx 0.5$ cm. Here, a stable starting reference height is reached.

The laser fringe signal is converted by a photodetector into an AC signal and is amplified.

Figure 2.3 shows the data acquisition and processing schematic. The laser fringe

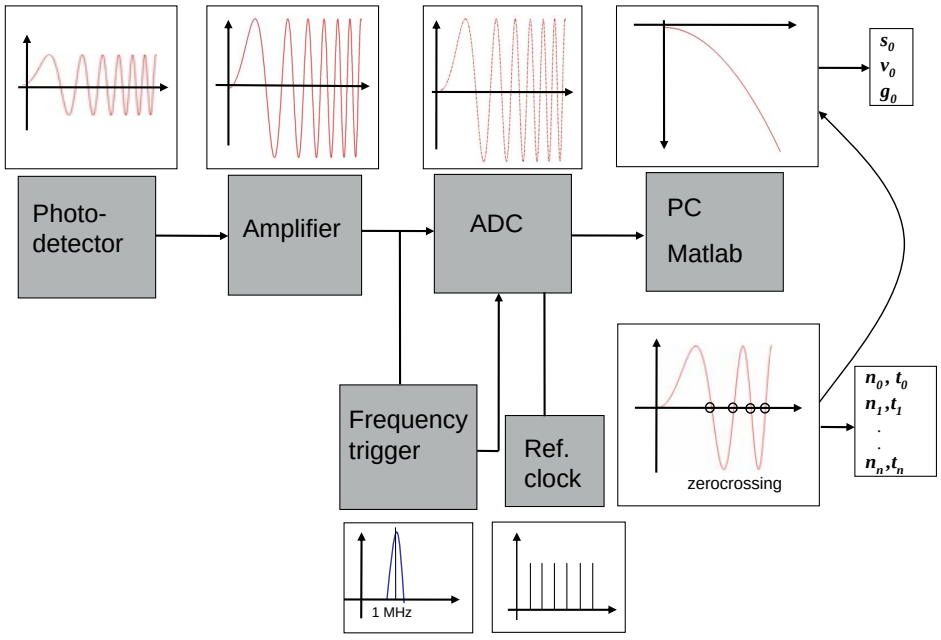


**Figure 2.3:** Data acquisition and processing.

signal is first detected and amplified, and then digitized, before it is processed by the software.

### 2.1.3 Software

After the fringe signal is digitized, the data is loaded onto the PC and processed. The analysis software was written with MATLAB. Figures 2.5(a) and 2.5(b) show screen shots of the graphical user interface.

Alongside the data analysis, MATLAB also controls the motor. Although the trajectories for the motor are programmed with software provided by Mattke AG, the motor company, the MATLAB code retrieves the trajectories, stored in the motor drive, by an RS232 serial connector. So the whole measurement is automated with the software. The algorithm for the measurement is depicted in Fig. 2.4.

Since the whole fringe signal is digitized, different fitting algorithms can

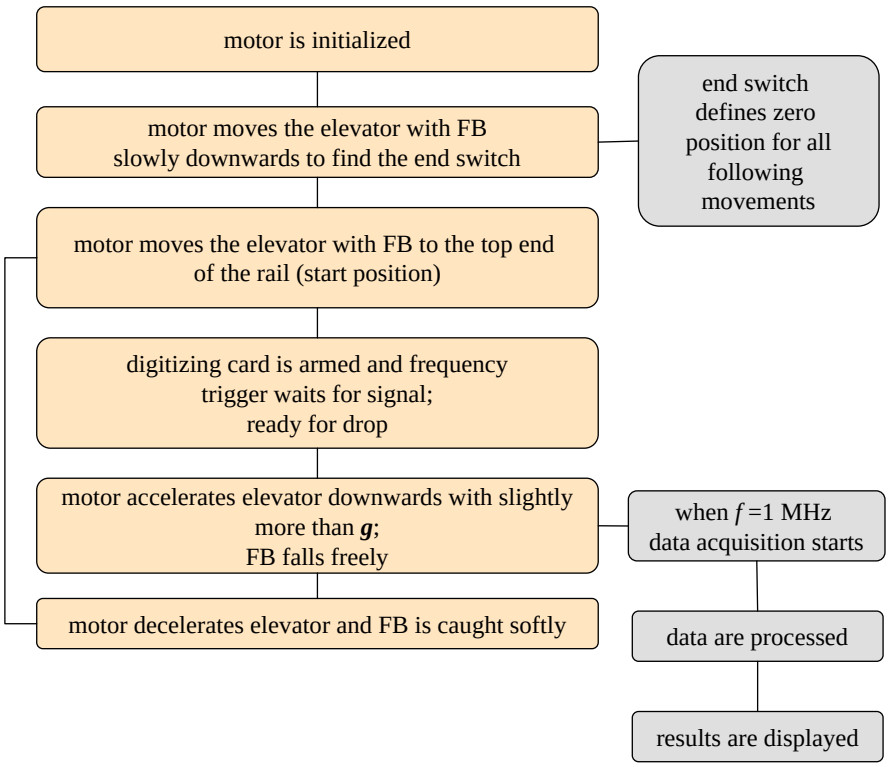


**Figure 2.4:** Workflow of MPG-1.

be applied to the same drop and can be compared. We have implemented (1) digital zero crossing (*DZC*), (2) the second difference method (*2ndDiff*) and (3)

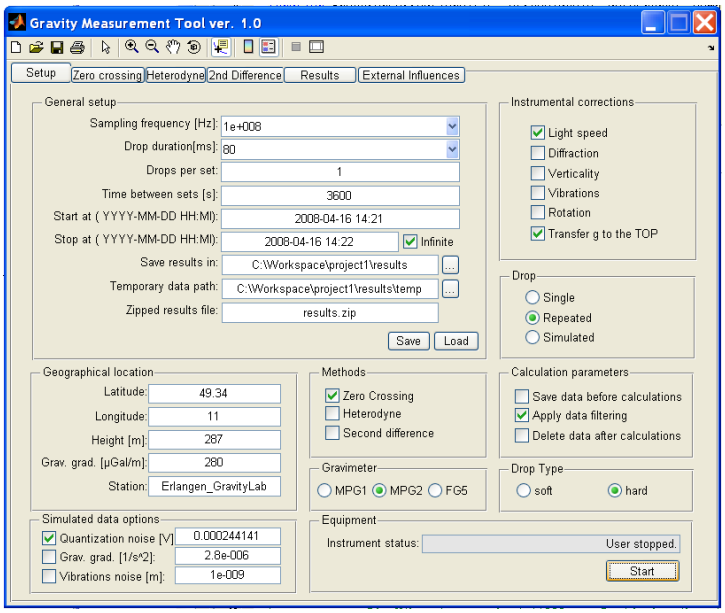


(a) GUI – principle page.

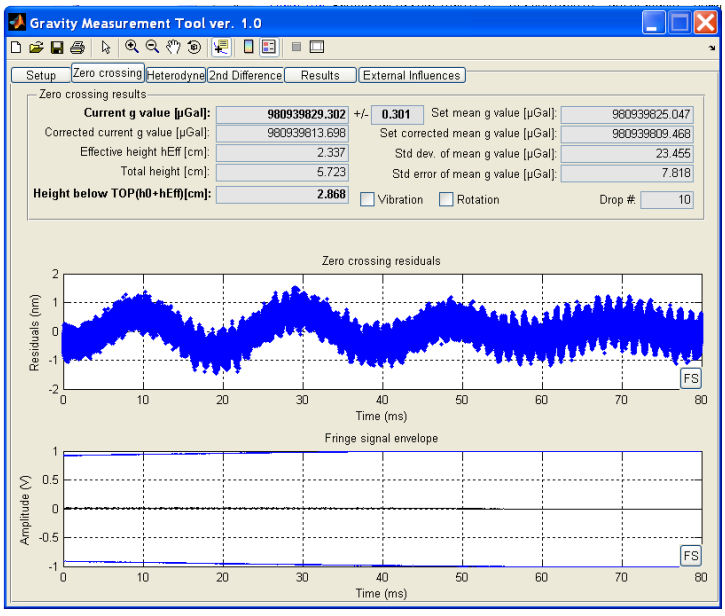


(b) GUI – residuals page.

**Figure 2.5:** The graphical user interface programmed with MATLAB.

heterodyning. This opens new possibilities in data analysis. So far just DZC is used, but comparisons of the three methods are planned for future long-term measurements.

DZC works similar to analogue zero crossing. The fringe signal is browsed

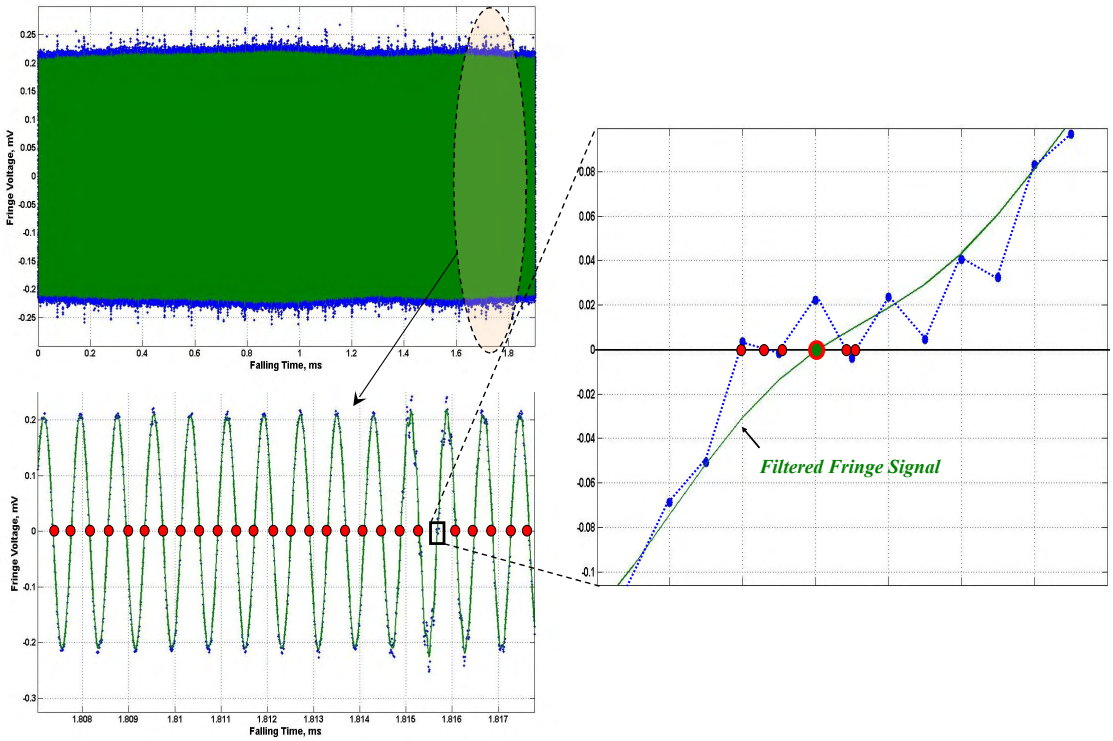


**Figure 2.6:** The non phase shifting digital filter helps to reduce noise in the fringe signal. The blue dots show the digitized fringe signal, and the green line the filtered fringe signal.

for zero crossings and the respective times are calculated. Each zero crossing signifies a change in path length of the falling object of a quarter wavelength $\lambda/4$ of the laser ($\lambda \approx 633$ nm for the He-Ne laser). To these time-space data pairs, a polynomial of second order is fitted (Equ. 1.8). The coefficient of the quadratic term contains the acceleration due to gravity.

One advantage *DZC* has over analogue zero crossing is that it allows for application of digital filters. In our software, we included a non-phase-shifting filter. This filter makes it possible to clean a noisy fringe signal, without introducing

errors due to phase shifts. When the signal is noisy, fake multiple zero crossings can be detected, as seen in Fig. 2.6. These values give a bad $g$-value and the drop should be skipped. So by applying this filter, the number of outliers can be reduced and the lifetime of the gravimeter can be enhanced.

The 2ndDiff method will not be explained here, but a detailed description can be found in Tsubokawa & Svitlov (1999).

Both of these methods, DZC and the 2ndDiff employ linear models. In contrast, the third method, the heterodyning, is a non-linear method. The advantage of heterodyning is that the signal can be undersampled. So if memory has to be saved, or the maximum sampling rate of the digitizing card cannot fulfil the Nyquist-Shannon theorem, where the sample rate must be more than twice the signal frequency then this method provides a good alternative. A description of the method can be found in Niebauer *et al.* (2006). A drawback is the difficulty of introducing disturbing effects in a non-linear model.

Table 2.1 shows typical single drop parameters for the MPG-1.

**Table 2.1:** Typical single drop parameters

| | |
|---|---|
| Falling time T | = 200 ms |
| Tracked falling distance H | ≈ 26 cm |
| (Triggered @ 1 MHz, or $h_0$ | ≈ 0.5 cm after 33 ms of a free fall) |
| Effective height $h_{eff}$ | = 9.80/8.80 cm (*depending on the method*) |
| Sampling frequency $f_s$ | = 100/200/400 MS/s |
| Required memory depth | = 160/320/640 MByte |
| Amplitude resolution | = 12 Bit |
| Number of samples | = 20/40/80 MS |
| Number of zero crossings | ≈ 1.6 Million (*in case of linear model*) |
| Time to process 1 drop $t_d$ | ≈ 15/30/45 s |

### 2.1.4 Mechanics

The dropping chamber is composed of the vacuum chamber, with the mechanics inside, the motor, and the ion pump. The vacuum chamber is made of stainless steel, measures 100 cm in height and has a diameter of 25 cm. It is placed on a smaller table, which in turn is fixed to the surface of the optical table. The verticality of the vacuum chamber can be adjusted by means of three screws on

the bottom flange of the chamber. This aligns the rail the elevator, and hence the FB, moves along, parallel to the gravity vector **g**. Only coarse adjustment is needed here, as the FB falls freely during the measurement with no physical contact with the elevator until it is caught again. The alignment of the rail ensures that the FB falls into the elevator's vee-grooves in the same position it had in the beginning, when the data acquisition started. The bottom flange of the vacuum chamber also has a fused silica window, through which the vertically aligned laser beam enters from the interferometer, goes to the object mirror, i.e. the FB, and is reflected back to the interferometer.

The mechanical parts inside are made of aluminium and stainless steel. The

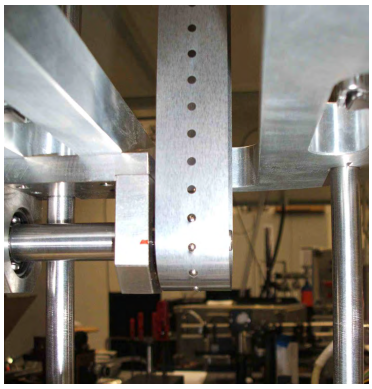

**Figure 2.7:** The elevator is connected to a perforated steel belt. The pulley is driven by a position controlled motor.

small lifting chamber (elevator), containing the falling body is fixed to a perforated stainless steel belt (fig. 2.7). Its perforation holes fit into small teeth from the pulley, which prevent the belt from slipping through. This belt, in turn, is connected to the motor (Mattke AG), which has a position encoder, which – together with the perforated belt – allows precise positioning of the lifting chamber. Different ramps can thus be programmed on the motor and the distance between the lifting chamber and the falling body can be calculated. As the motor lies outside the vacuum chamber, a rotary magnetic feedthrough is used to connect the motor to the belt. It is dimensioned for a vacuum of the order of $10^{-10}$ mbar. The lifting chamber is guided along a rail by two bearings (THK), which provide

high stiffness on the one hand and low friction on the other. UHV-grease (Lubcon, Ultratherm 2000) is used for lubrication.

The whole setup sits on an optical table (Opta GmbH) with a mass of approximately 500 kg. This huge mass makes the whole set up very rigid and reduces the transmission of the shocks resulting from the drop to the laboratory floor and, hence to the Super Spring, i.e. the reference mirror.

All of the mechanical parts and the vacuum chamber were baked during the first pumping, to free all surfaces from residual water molecules. Once the desired vacuum of the order of $1 \times 10^{-8}$ mbar is reached by means of the rough pump and the turbo pump, the vacuum is maintained with an ion pump (Varian Inc), attached to the bottom end of the vacuum chamber, at a sufficient distance to avoid disturbing magnetic fields on the FB.

The FB itself is made of titanium and contains a hollow corner cube retroreflector (ProSystems[1], model VersaMount, USA), silver coated for a laser wavelength of 633 nm. Three ball-bearing balls, which fit into three vee-grooves of a support ring, are pressed into its housing, and the support ring is mounted to the interior of the elevator. Due to the fact that the elevator is accelerated downwards with more than $g$ when a drop is performed, the FB separates to up to 5 mm from the support ring until it is softly caught again by the elevator. The distance the elevator moves during the drop is about 50 cm. During this distance a pure free fall length of the FB of 30 cm can be reached, i.e. a drop duration of about 250 ms.

## 2.2 Results and analysis

After 1.5 years, MPG-1 was able to record long-term measurements (LT) with standard errors of less than 10 $\mu$Gal. With this resolution we were able to reveal systematic errors, like a serious problem caused by the interferometer being mounted on the optical table, where it was picking up the motor's vibration. The error source was easily removed by putting the interferometer on an active vibration isolation, which reduced the residuals in a single drop data fit from $\approx$

[1]This company does not produce retroreflectors any more.

100 nm to less than 10 nm.

Once the main error sources were eliminated or reduced, and the measurement procedure was automated, the set up was tested in a one-month LT. Figure 2.8 shows the result, whereas Fig. 2.9 is a closeup of a 72 hour section of the same LT. The measured data (blue dots) very smoothly fit to the theoretical change of gravity calculated by an Earth tides model (TSoft, 2008). During the LT, a

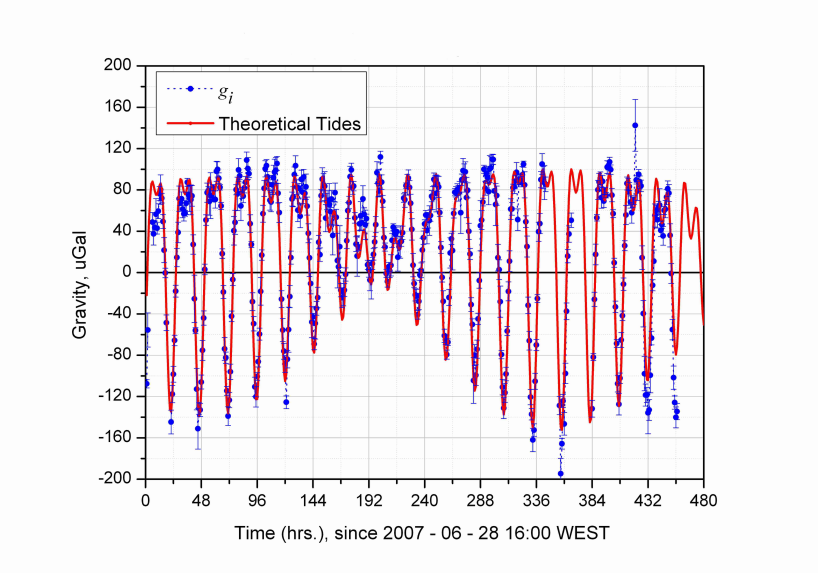


**Figure 2.8:** One month of measured gravity with MPG-1 (LT#5). The red solid line shows the theoretical tidal gravity influence. The blue dots show the measured values with the respective standard errors as error bars.

sampling frequency $f_s$ of 100 MS $s^{-1}$ was used. Each hour one set of data was taken, with a set of data consisting of 10 single measurements. The standard error bars (shown in Figs. 2.8, 2.10 and 2.9; mean $g$-values are subtracted) are calculated from these sets. Figure 2.10 shows the residuals of the LT after subtracting the mean $g$-value. One set takes approximately 3 minutes. The time needed to perform one set of measurements could be reduced by just skipping the digital filter, but it greatly improved the number of accepted drops, so the option is kept switched on. Unfortunately, first saving the fringe signal and processing it later does not improve the performance, since saving data takes as much time as processing them. The filtering algorithm is a built in function from MATLAB's

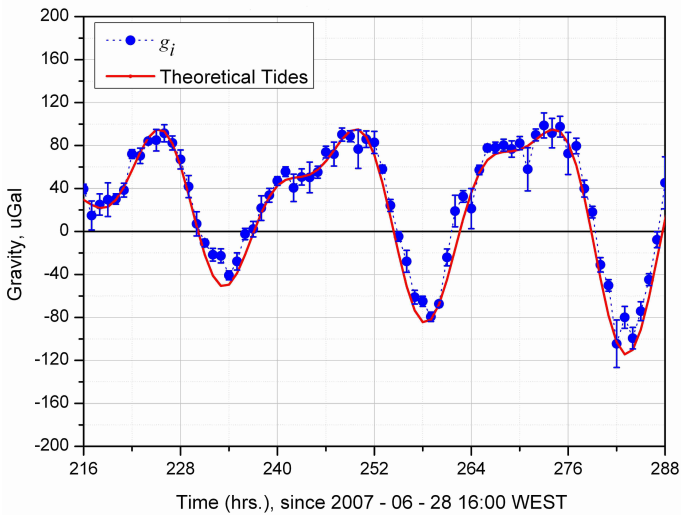


**Figure 2.9:** One month of measured gravity with MPG-1 (LT#5). A closer look clearly shows that the data measured agree with theoretical tidal models.

signal processing toolbox, and hence, already optimized. *DZC* is also optimized and leaves no room for further improvement.

With the one-month LT we finally were able to reach a resolution of 0.6 $\mu$Gal, after correction for solid tides, pressure effects, and temperature effects.

In Fig. 2.11 the amplitude spectrum of LT#5 is shown. The diurnal constituents $O_1$ (26 h 16 m) and $K_1$ (23 h 49 m) can be identified, as well as the semi-diurnal constituents $M_2$ (12 h 29 m) and $S_2$ (12 h 03 m). This is in good agreement with the amplitude spectrum obtained from theoretical data (cf. Fig. 1.6 and Tab. 1.2).

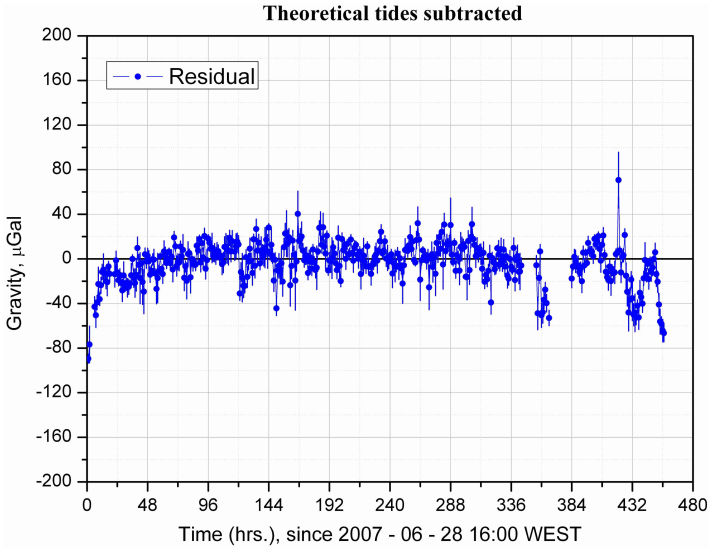


**Figure 2.10:** Residuals of one month of measured gravity with MPG-1 (LT#5), with the theoretical tides subtracted. The mean $g$-value is also subtracted.

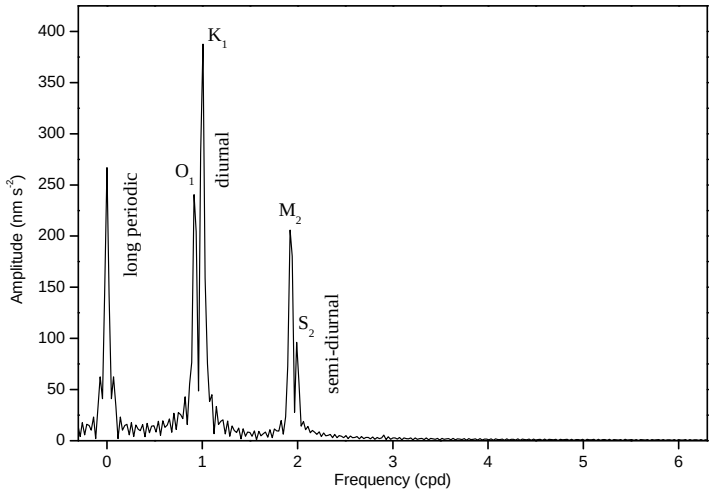


**Figure 2.11:** Amplitude spectrum of one month of measured gravity with MPG- 1 (LT#5).

# Chapter 3

# Portable free fall gravimeter MPG-2

## 3.1 Introduction

Once MPG-1 was running and producing satisfactory results, we went on to build a portable absolute gravimeter MPG-2 based on the experience obtained with MPG-1. As an improvement over MPG-1, the mechanics were redesigned to reduce the vibrations the motor caused during the drop.

The need for a portable device is obvious. In a day-to-day practice, gravimetric measurements have to be carried out on-site at different locations. The data obtained on-site are compared and are used for gravity networks. While MPG-1 functions as a highly accurate reference system, the portable gravimeter is further developed in order to be directly compared with other gravimeters, as is regularly done at international comparisons like the European Comparison of Absolute Gravimeters (ECAG), Luxembourg, or the International Comparison of Absolute Gravimeters (ICAG) at the Bureau International des Poids et Mesures (BIPM), Paris.

This chapter presents the setup of the portable absolute free fall Max Planck Gravimeter 2 (MPG-2). The results of the ECAG 2007 in Walferdange, Luxembourg, will be discussed, as well as a further comparison with Germany's federal agency for cartography and geodesy, which was conducted in February 2008.

## 3.2 Set up

Figure 3.1 shows the setup of the MPG-2. It is a portable absolute gravimeter, albeit still a prototype. It consists of the dropping chamber with the ion pump, a tripod, the Super Spring as reference mirror, and a notebook with a PCI extension. Further components are the laser and the atomic clock, as separate units.

**Figure 3.1:** The setup of the portable free fall gravimeter MPG-2 at a measurement point in the mine in Walferdange/ Luxembourg in November 2007. (The position of the ion pump is different in the new setup - see discussion in Subsection 3.3.1).

### 3.2.1 Optics and laser

MPG-2's interferometer follows the same principle as used for MPG-1, but miniaturized and fixed to the housing of the Super Spring (Fig. 3.2). Additionally, the laser is fibre-coupled to the interferometer. The beam verticality is aligned by replacing the second beam splitter with a hollow retroreflector, and is explained

in Section 5.1.5. The same laser is used for MPG-2 and MPG-1, but with MPG-2

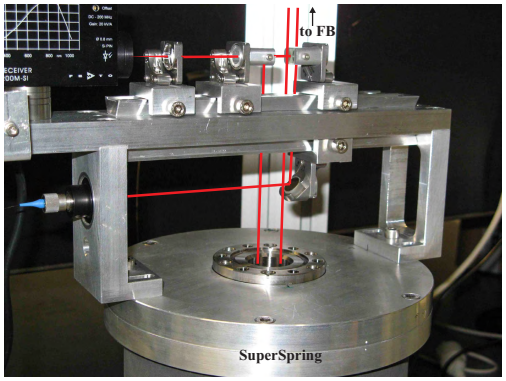


**Figure 3.2:** The Michelson interferometer is directly mounted on the Super Spring.

it is fibre-coupled and mounted on a breadboard. For this breadboard, a housing was constructed to make the setup rigid and portable.

### 3.2.2 Electronics

The electronics is assembled in a 4-slot PCI-extension from Magma (Fig. 3.3). It consists of the digitizing card and the frequency trigger. The PCI-extension is connected to a notebook (2 GB RAM, Intel® Core™ T7200 @ 2.00 GHz). The motor drive and power supplies are integrated in a 19 inch rack, which is connected to the PCI-extension.

### 3.2.3 Software

The same software is used for MPG-2 and MPG-1, which is possible due to its option of switching from MPG-1 to MPG-2 parameters. The workflow of a drop is sketched in Fig. 3.4.

### 3.2.4 Mechanics

The mechanics were completely redesigned for MPG-2. It was necessary to reduce the motor's size and minimize the vibrations it caused during the drops. Beyond

**Figure 3.3:** The electronics for MPG-2 is assembled in a PCI extension, connected to a notebook.

this, a portable gravimeter should be easy to disassemble and have a compact design. The main modification to MPG-1's mechanics is that MPG-2's elevator is accelerated by springs instead of a motor (cf. Fig. 3.5). MPG-2's vacuum-compatible stepper motor (Phytron) is mounted inside the vacuum chamber and has the sole purpose of lifting the elevator containing the FB. On its way up, the elevator is guided by two ball bearings (THK), lubricated with vacuum grease. A third ball bearing guides a cart that hooks into the elevator to tow it upwards. The springs are loaded during the lifting process. When a special mechanism releases them once they reach the top position, they withdraw the elevator back to its initial position.

A further modification was made regarding the drop length. MPG-1's maximum drop length is 30 cm, whereas MPG-2 is reduced to 10 cm as a further requirement to compactness. The drop length can be adjusted by changing the spring's length and strength.

The vacuum chamber has an upper and a lower window flange, the upper serving as an observation window while the lower is the entrance and exit window of the laser light. Originally, the ion pump was placed on the vacuum chamber next to the falling tower. During the international comparison it became evident that this arrangement negatively affected the measurements (cf. Section 3.3.1). The magnetic field produced by the ion pump was far too strong at this distance and accordingly distorted the results. So in a later design we displaced it to a

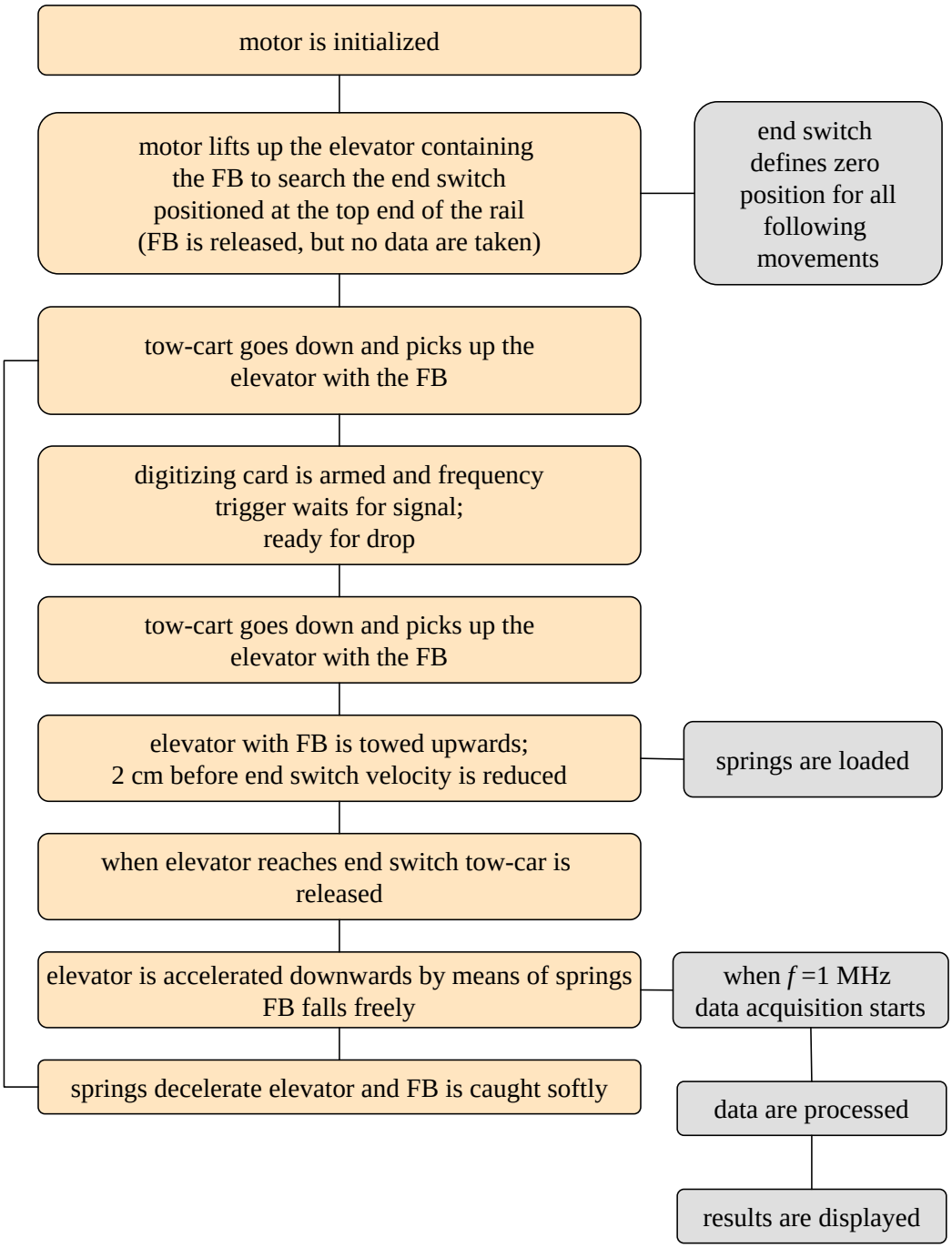


**Figure 3.4:** Workflow of MPG-2.

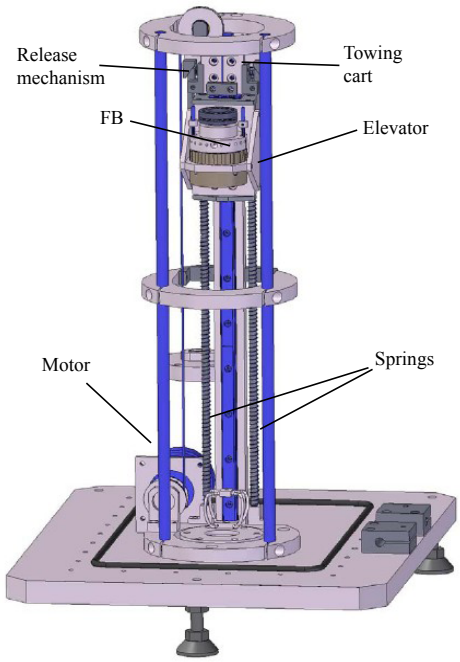


**Figure 3.5:** The portable gravimeter MPG-2 uses springs for acceleration of the elevator, rather than the motor. The motor is just used to lift up the elevator and load the springs. Herewith the vibrations during the free fall are reduced.

position approximately 30 cm further away from the dropping chamber.

As a stable base, a tripod made of aluminium profiles was constructed. The vacuum chamber is placed on the tripod, which has an $x$-$y$-adjustable plate on the top. This adjustable plate allows to align the reflected laser beam, to give a good overlap of the two beams in the interferometer. This is done via two micrometer screws.

The entire mechanical setup measures about 1.30 m in height, and the weight of the whole equipment is about 70 kg.

### 3.2.5 Results

After less than one year of construction, the first satisfactory results with MPG-2 were obtained. Figure 3.6 shows the first long-term measurement we conducted in the end of October 2007.

By correcting the value for theoretical tides we obtained a statistical uncertainty

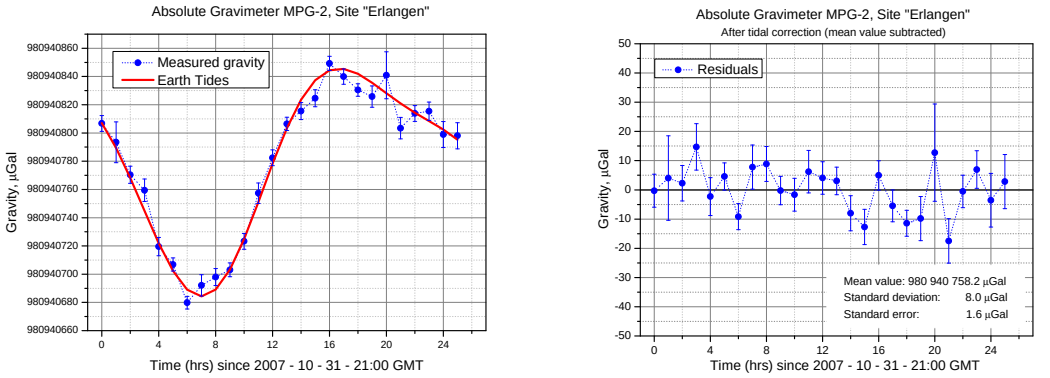


(a) Tidal influences.

(b) The residuals after tidal corrections.

**Figure 3.6:** The first long-term measurement at site Erlangen showed very promising results

of 1.6 $\mu$Gal, when measured during 24 hours. This was an excellent result.

## 3.3 International comparison ECAG 2007, Walferdange/Luxembourg

We participated in the European Comparison of Absolute Gravimeters (ECAG) from November 6th to 9th, 2007, in Walferdange, Luxembourg. The measurement site was located in a gypsum mine (Fig. 3.7). Besides our MPG-2, the comparison included 17 FG5's, 1 JILAG, and the only European rise-and-fall gravimeter IMGC-2.

For the comparison each group had to measure at least for 12 hours at 3 different pillars. The different pillars were located at different heights inside the same measurement room. Additionally, the atomic clocks, thermometers, and pressure gages of each participating group were compared. The first setup time of MPG-2 took several hours, mainly due to the warm-up time of the standards and apparatus. When moving to the next measurement site, however, it took us only one hour to start the next set of measurements.

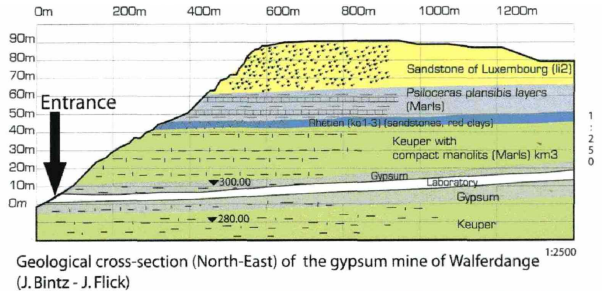


a)

b)

**Figure 3.7:** The ECAG 2007 took place in a gypsum mine in Walferdange, Luxembourg: a) map of the mine; b) picture from the measurement room inside the mine.

Measurements were conducted at three different sites (Fig. 3.8 shows the

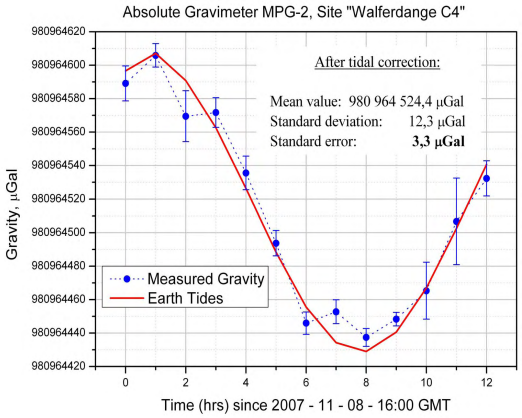


**Figure 3.8:** Measurement at the site C4 at ECAG 2007.

measurement results conducted at site C4) and no serious problems occurred. However, our results showed a considerable disagreement with the values obtained by other apparatuses. Previous results showed that our gravimeter measured a value 510.7±13.4 $\mu$Gal higher than other devices, although the measurement standard uncertainty of MPG-2 during the comparison was typically about 5 $\mu$Gal.

### 3.3.1 Discussion of results

Although the offset of our measured values with respect to other gravimeters was too large, it was quite stable from site to site. The measurements very distinctly depicted the different heights (Fig. 3.9; measurement time at pillar A1 was not 12 hours, since due to warm-up time the measurement was started too late).

Tracing back our value to Erlangen, we were able to investigate the reason for

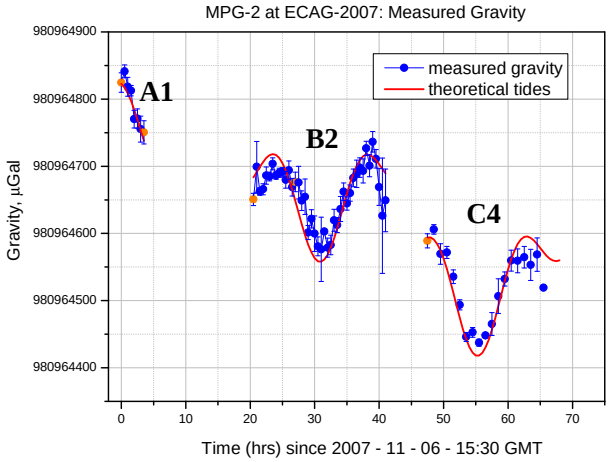


**Figure 3.9:** The measurements with MPG-2 showed good repeatability. The different mean values result from the different heights of the measurement sites.

the large offset observed at ECAG 2007. It turned out that the ion pump's magnet was too close to the dropping chamber (Fig. 3.10(a)). It acted directly on the FB and accelerated it downwards. Measurements were conducted to determine the magnetic field. Finally, we were able to reduce the offset by placing the ion pump about 30 cm further away (Fig. 3.10(b)).

## 3.4 Comparison with BKG

After the source of the offset during ECAG 2007, was located, another comparison had to be carried out to re-evaluate the offset. We were invited by the Bundesamt für Kartographie und Geodäsie (BKG) for a comparison at Bad Homburg,

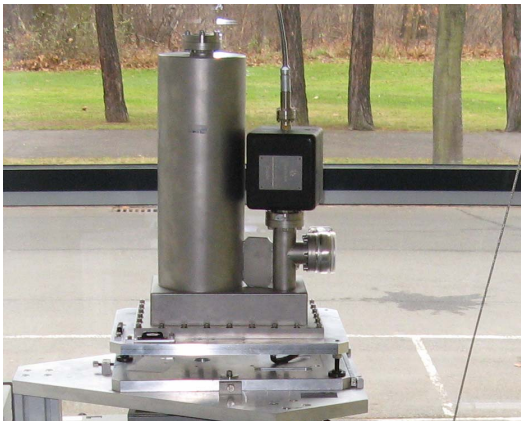

(a) Ion pump close to dropping chamber

(b) Ion pump far from dropping chamber

**Figure 3.10:** The influence of the ion pump's magnetic field was reduced by placing it farther away from the FB.

Germany. Besides the absolute gravimeters, the BKG owns two superconducting relative gravimeters that take continuous data. These were good conditions for a further investigation of our apparatus' systematic errors. Our assumption was confirmed. The offset was reduced by a factor 10. Taking the uncertainty budget and corrections (cf. Table 5.25) into account, our gravimeter's accuracy is in good agreement with FG5-101 from BKG (cf. Table 3.1 and Fig. 3.12). Our offset with respect to the value measured with the FG5 was $-37.6 \pm 38.4$ $\mu$Gal, for pillar BA, and $+9.8 \pm 38.4$ $\mu$Gal, for pillar AA. Figure 3.11 shows the measurement results for pillar AA.

**Table 3.1:** Measurement results – Bad Homburg.

| | Pillar BA | Pillar AA |
|---|---|---|
| Pure measurement | $981\,055\,060.8 \pm 3$ | $981\,055\,072.9 \pm 3$ |
| With corrections & std. unc. | $981\,055\,046.5 \pm 38.4$ | $981\,055\,057.5 \pm 38.4$ |
| Nominal value (FG5) | $981\,055\,081.0 \pm 2.0$ | $981\,055\,044.6 \pm 1.1$ |

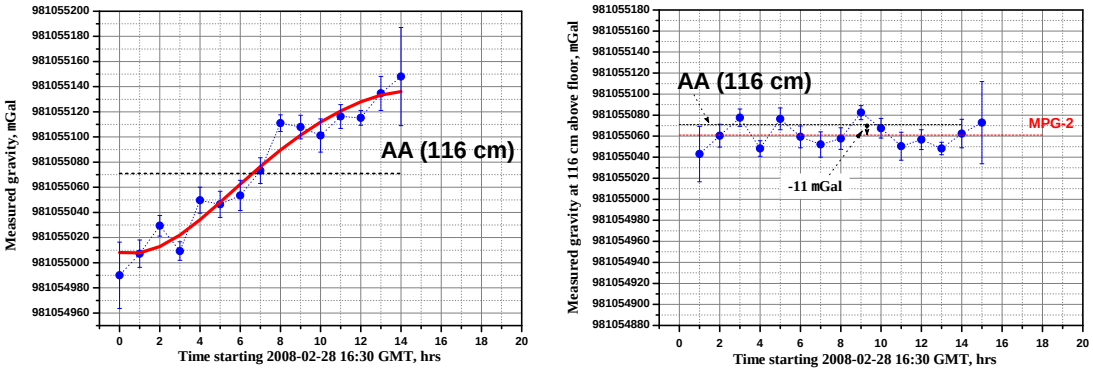


(a) Gravity values.

(b) Residuals (without instrumental corrections).

**Figure 3.11:** Measurements at Bad Homburg – pillar AA.

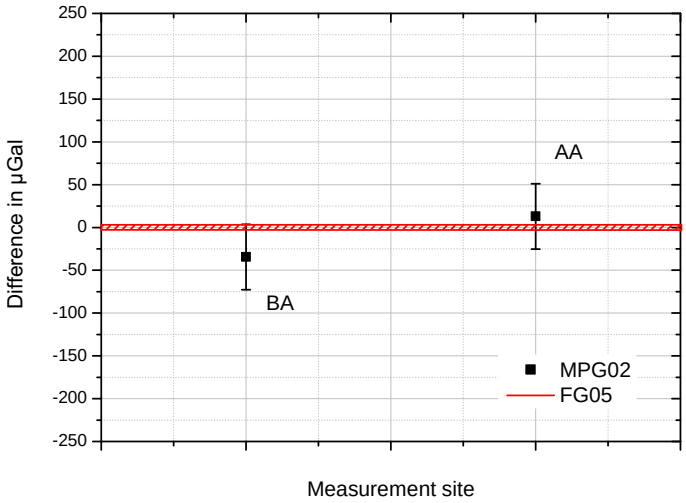


**Figure 3.12:** Measurement results – Bad Homburg. The FG5-value is the reference.

### 3.4.1 Discussion of the results

The comparison at BKG gave us an opportunity to evaluate our gravimeter in more detail. The results of the comparison were more than satisfactory. A full agreement of the measured values within the assessed uncertainty was reached. Of course, all possible error sources have to be further investigated. Just an improved uncertainty budget can give more information about an absolute accuracy. Nevertheless, the portable gravimeter MPG-2 can compete with state-of-the-art gravimeters.

# Chapter 4

# High-precision balancing of the falling body

For many years, the error due to the rotation of the falling body during its free fall was one of the biggest contributions to the absolute gravimeter's uncertainty budget (Hanada, 1988; Hanada *et al.*, 1996; Niebauer *et al.*, 1995). This is why many groups worked on reducing this error (Germak *et al.*, 2002; Hanada, 1988; Vitouchkine & Faller, 2004). This chapter describes how we reduced the contribution of the rotation of the falling body to the uncertainty budget. The development of these methods is a principal item of the thesis and will be discussed in more detail. We were the first in determining the distance between the optical centre of the falling body, and his centre of mass in three dimensions. Others did it only in one dimension.

Two different methods were developed. The first one includes a simple triple-mirror retroreflector assembled in a housing. The position of the optical centre (OC) of the triple mirror can have an unknown position inside the housing, but is determined with a coordinate measuring machine (CMM). The centre of mass (COM) of the entire housing-mirror assembly is then shifted to the OC by employing a commercial balancing machine.

We had two reasons developing a second method. The first was that the balancing technique needed to be enhanced, and the second was to find a way to perform the process without a CMM. CMMs are expensive, so to avoid buying

one or having the OC's position measured commercially, which would have involved bringing the falling body assembly to an according company, we started looking for commercial triple mirrors with known exact OC positions. Then we constructed the housing in a way that the housing-mirror assembly still provides knowledge of the OC to a small tolerance. By means of an enhanced balancing technique the COM is then shifted to the assumed OC.

The first of the two methods we discuss was published in 2007 (Rothleitner *et al.*, 2007a).

## 4.1 Introduction

An absolute gravimeter measures the acceleration of a body, falling freely in the Earth's gravity field. The falling body (FB) contains the object mirror of a laser interferometer (a corner cube prism or a hollow corner cube retroreflector; in our description, we employ a hollow corner cube mirror assembly). The Earth's gravity $g$ acts on the centre of mass (COM) of the falling body. However, the interferometer measures the displacement of the optical centre (OC) of the falling body. Therefore it is vital that the COM and OC coincide. With the OC additionally rotating around the COM during free fall, an additional acceleration will be measured. Its vertical component is

$$a(t) = \omega^2 R \sin(\gamma_0 + \omega t) \; , \tag{4.1}$$

where $\omega$ is the horizontal component of the angular velocity, $R$ the actual distance between the OC and the COM, and $\gamma_0$ the initial angular position of the OC relative to the horizontal plane (Fig. 4.1).

For small rotation angles $\omega t$ during free fall, minimum distortion is reached when $\gamma_0 \approx 0°$ or $\gamma_0 \approx 180°$, i.e. the OC and the COM are separated mainly horizontally. On the other hand, it hits the maximum, when $\gamma_0 \approx 90°$ or $\gamma_0 \approx 270°$, i.e. the separation between the centres is vertical. In this case the distorting acceleration (4.1) is $a(t) \approx \pm\omega^2 R \cos(\omega t)$, where the $\pm$ refer to the OC above/below the COM. Here the value of acceleration does not depend on the direction of rotation. The maximum acceleration is given by

$$|a_{max}| = \omega^2 R \; . \tag{4.2}$$

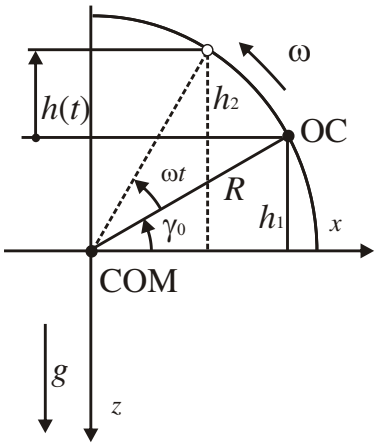


**Figure 4.1:** Rotation of the falling body causes an error in $g$ measurement. If the OC rotates by an angle $\omega t$ about the COM, an apparent change in path length is $h(t) = h_2 - h_1 = -R\sin(\gamma_0 + \omega t) + R\sin\gamma_0$, which results in a distorting acceleration $a(t) = \omega^2 R\sin(\gamma_0 + \omega t)$.

At first glance it seems that only the distance in $z$-direction is important to be balanced. However, if the FB sits not exactly horizontal in the vee-grooves, but inclined to some degree, a distance between the COM and the OC in the horizontal $x$-$y$-plane has a projected part along the $z$-axis. The other reason why a 3-dimensional balancing should be considered is, that a separation of the two centres in the $x$-$y$-plane produces distortions in the third order term, which contains the gravity gradient. An extraction of the gravity gradient from a single drop is planned for the future.

Equation 4.2 illustrates that there are two ways to reduce the error due to FB rotation: either to decrease the value of rotational velocity during free fall or to minimize the distance between the centres. As a rotation is often unavoidable, much research is concentrated on reducing the distance between the centres.

Early works employed an interferometric method to coincide the OC with the COM. A Michelson interferometer generates a fringe pattern between a reference corner cube retroreflector and the corner cube falling body assembly. The falling body assembly is placed on a rotating table. The interference signal contains information about the distance between the OC and the axis of rotation. The

table is constructed in a way that the falling body can be rotated around either the COM (Hanada, 1988) or the OC (Germak *et al.*, 2002). In the first case, the OC is adjusted to within about 50 $\mu$m of the vertical axis of rotation by minimizing the number of fringes during one revolution of the rotating table (Hanada, 1988). Similarly, in the second case, the falling body assembly is shifted to coincide the OC with the horizontal axis of rotation. Then the natural equilibrium of the falling body assembly, mounted on the previously balanced rotating table, indicates the position of the COM relative to the axis of rotation. Hence, in both cases it is possible to adjust the OC and the COM to the axis of rotation. In Germak *et al.* (2002) it was also realized that the total distance in 3D space had to be accounted for. The smallest achievable distances between centres were hence estimated to be 33 $\mu$m and 14 $\mu$m for the falling body assemblies with masses of 33 g and 75 g, respectively (Germak *et al.*, 2002).

Another method to improve the alignment of the centres is to monitor the value of $g$ while introducing a defined rotation on the falling body (Vitouchkine & Faller, 2004). In this case, the COM is moved to coincide with the OC until the difference in the measured values of $g$ is minimized. However, this method requires the vacuum chamber to be opened several times to extract the falling body in order to adjust the COM.

Here, we describe a different method for measuring and minimizing the distance between the OC and the COM in 3D space using a mechanical balancing technique. The method is similar to that commonly used in industry to balance rigid rotors (Schneider, 2003). We demonstrate that the resolution of this method approaches that of an interferometric one with the advantage that the relative position of the centres in 3D space is well defined.

## 4.2 Balancing in three dimensions

### 4.2.1 Theory of balancing

Consider an object with a mass $m$ that rotates at an angular velocity $\Omega$ about an axis. If the COM is offset from the rotation axis by a vector $\mathbf{e}$ with coordinates

$x$, $y$, and $z$, a centrifugal force $\mathbf{F} = m\mathbf{e}\,\Omega^2$ is produced. The product $m\mathbf{e}$ is called the imbalance $\mathbf{u}$:

$$\mathbf{u} = m\mathbf{e}\,. \tag{4.3}$$

The imbalance during rotation around the $z$-axis, projected onto the $x$-$y$ plane, is $\mathbf{u}_L = m\mathbf{e}_L$ (Fig. 4.2). Similarly, projection of this imbalance onto the $y$-$z$ plane

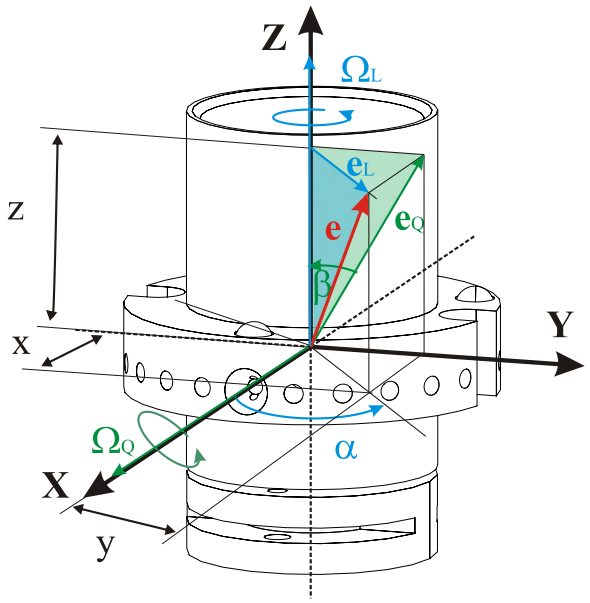


**Figure 4.2:** Eccentricity of the centre of mass in 3D space (vector $\mathbf{e}$ with coordinates $x$, $y$, and $z$).

is $\mathbf{u}_Q = m\mathbf{e}_Q$. Here $\mathbf{e}_L$ and $\mathbf{e}_Q$ are the eccentricities, which express the distance from the axis of rotation to the projection of the COM onto the orthogonal plane. The lengths of these vectors are:

$$\begin{aligned} |\mathbf{e}_L| &= \sqrt{(x^2 + y^2)}\,, \\ |\mathbf{e}_Q| &= \sqrt{(y^2 + z^2)}\,. \end{aligned} \tag{4.4}$$

The angles between the projected vector $\mathbf{e}_L$ and the $x$-axis, and vector $\mathbf{e}_Q$ and the $z$-axis are called $\alpha$ and $\beta$, respectively:

$$\begin{aligned} \alpha &= \arctan\left(\frac{y}{x}\right)\,, \\ \beta &= \arctan\left(\frac{y}{z}\right)\,. \end{aligned} \tag{4.5}$$

A balancing machine measures the vibrational accelerations at the shaft of the rotor $\mathbf{a} = K_S\mathbf{F}/m_S$, where $K_S$ and $m_S$ are the scale factor (sensitivity) and the inertial mass of the accelerometer, respectively. Provided that another scale factor $C = |\mathbf{u}|/|\mathbf{a}|$ is derived during the calibration, the balancing machine calculates the values of the imbalances $u_L = |\mathbf{u_L}| = C|\mathbf{a_L}|$ or $u_Q = |\mathbf{u_Q}| = C|\mathbf{a_Q}|$ with the corresponding angles $\alpha$ or $\beta$. By changing the mass distribution of the rotor, the imbalance can be reduced.

If the mass $m$ of an object is known and constant, and the values of the imbalances $u_L$, $u_Q$ and the angles $\alpha$, $\beta$ are measured, it is possible to solve Eqs. (4.3), (4.4) and (4.5) to find the position of the COM, namely the coordinates $x_{COM}$, $y_{COM}$, and $z_{COM}$. Given that the OC is located at the known coordinates $x_{OC}$, $y_{OC}$, and $z_{OC}$, the COM can then be shifted to this point by changing the mass distribution of the falling body. Thus, instead of completely reducing the imbalance, one has to adjust it to an amount deduced from the position of the OC and the mass value of the falling body.

### 4.2.2 Method

To adjust the COM to the OC, we first constructed a suitable housing for the corner cube retroreflector (Fig. 4.3(a)). For light weight and high strength, the housing is constructed using titanium. A commercial, high precision, hollow corner cube retroreflector (VersaMount Prosystems, USA) with an aperture diameter of 1 inch (25.4 mm)is embedded inside the housing. In order to shift the COM of the entire test body assembly, tap holes and a movable counter mass are added (Fig. 4.3(a)). The housing is designed in a way as to rotate the falling body around two axes perpendicular to each other (Fig. 4.3(b)). By adjusting the counter mass, the COM can be moved along the $z$-axis. To move the COM in the $x$-$y$-plane, screws can be wound into or out of the tap holes. After mounting the retroreflector in the housing, the actual coordinates ($x_{OC}$, $y_{OC}$, and $z_{OC}$) of the OC are measured in the Cartesian coordinate system, using a coordinate measuring machine (DEA, Italy, model Global classic, Hexagon Metrology; Fig. 4.4). This coordinate system has its origin in the intersection point of two rotational axes (Fig. 4.3(b)).

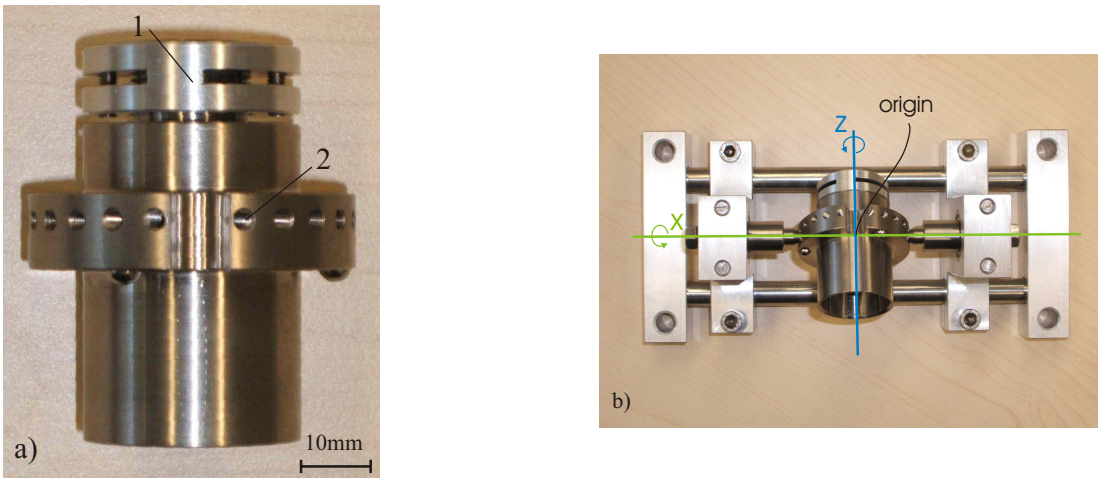


**Figure 4.3:** Falling body of the absolute gravimeter: a) housing of the corner cube retro-reflector (1 - counter mass, 2 - tap hole); b) position during balancing (point of intersection of the rotational axes defines origin of the coordinate system).

**Figure 4.4:** The position of the OC is measured with a coordinate measuring machine.

Once the OC's position is determined, it is possible to start balancing the falling body. A commercial balancing machine (Micro Präzision Marx GmbH, Germany, model BMT 210M) is used. Figure 4.5 shows the main set up. The falling body (a) is centred in the support by two mounting jigs. Its rotation is driven by a motor (b). An optical sensor (c) is employed to detect the angular frequency and phase. A vibration sensor (d) is used to measure the vibrational

accelerations. The balancing machine is calibrated first by introducing a well defined imbalance, i.e. by placing a known mass at a known radius. After calibration, this calibration mass is removed. The balancing machine reports the calculated values of the imbalance in the polar coordinate system. The polar axis of this coordinate system starts at the origin, shown in Fig. 4.3 (b), and passes through the position of the calibration mass, attached during calibration. Thus, after balancing in two planes, the values of the imbalances $u_L$ and $u_Q$ with the corresponding angles $\alpha$ and $\beta$ are known. Then from (4.3) the values of the eccentricities are

$$\begin{aligned} e_L &= \frac{u_L}{m} \,, \\ e_Q &= \frac{u_Q}{m} \,. \end{aligned} \tag{4.6}$$

From (4.4) and (4.5) the coordinates of the COM are

$$\begin{aligned} x_{COM} &= e_L \cos\alpha \,, \\ y_{COM} &= e_L \sin\alpha \,, \\ z_{COM} &= e_Q \cos\beta \,. \end{aligned} \tag{4.7}$$

Compared with the known coordinates $x_{OC}$, $y_{OC}$ and $z_{OC}$ of the OC, the

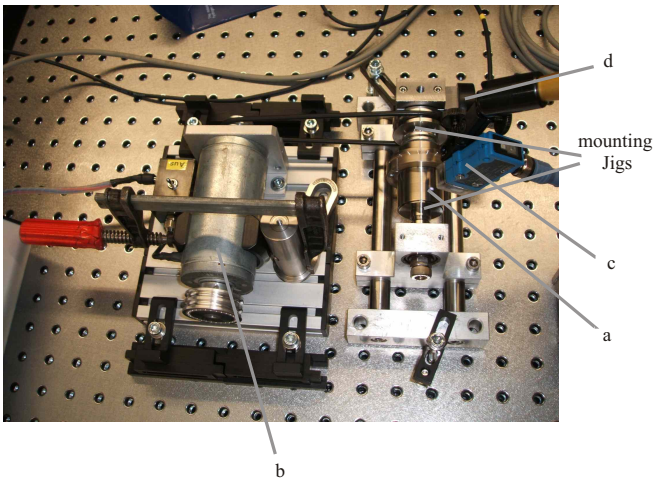


**Figure 4.5:** Balancing setup: (a) falling body; (b) drive motor; (c) optical sensor; (d) vibration sensor.

differences between the centres in each coordinate are

$$\begin{aligned} \Delta x &= x_{COM} - x_{OC} \ , \\ \Delta y &= y_{COM} - y_{OC} \ , \\ \Delta z &= z_{COM} - z_{OC} \ . \end{aligned} \tag{4.8}$$

Hence, the total distance $R$ between the two centres is

$$R = \sqrt{(\Delta x^2 + \Delta y^2 + \Delta z^2)} \ . \tag{4.9}$$

To minimize $R$, the COM is moved to the OC by shifting the counter mass of the housing or by winding in or out screws in the tap holes (Fig. 4.3(a)). After each change of mass distribution, the imbalances are remeasured and calculations (4.6) – (4.9) are repeated. This procedure is performed for both the $x$-axis and $z$-axis of rotation (Fig. 4.3(b)) until $R$ is minimized.

In order to measure the minimized distance $R$ more precisely, we apply

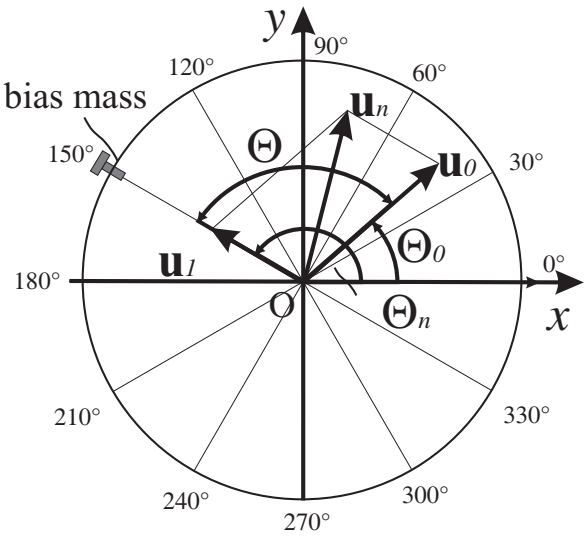


**Figure 4.6:** Enhanced method to detect the imbalance. The unknown imbalance $\mathbf{u}_0$ is at the unknown angle $\Theta_0$ to the $x$-axis of the Cartesian coordinate system, where the OC is defined. The additional imbalance $\mathbf{u}_1$ is applied at twelve different angles $\Theta_n$. The measured imbalance $|\mathbf{u}_n|$ reaches a maximum, when $\Theta = \Theta_n - \Theta_0 = 0$.

the procedure with the enhanced resolution (Schneider, 2003). In this case the

imbalance is measured in another polar coordinate system where the polar axis starts at the same origin (Fig. 4.3(b)) and coincides with the positive $x$-axis or the $z$-axis (Fig. 4.6). A small mass is then attached to the falling body (or to the mounting jigs) at twelve different angular positions in the plane, orthogonal to the axis of rotation. The measured imbalance $u_n = |\mathbf{u}_n|$ depends on the angle $\Theta = \Theta_n - \Theta_0$ between the existing imbalance $\mathbf{u}_0$ and the additional imbalance $\mathbf{u}_1$ (Fig. 4.6). To calculate it, the "parallelogram rule" and the cosine theorem can be used:

$$u_n = \sqrt{u_0^2 + u_1^2 + 2u_0u_1\cos(\Theta_n - \Theta_0)}\ . \tag{4.10}$$

Here $u_0 = |\mathbf{u}_0|$ is the unknown imbalance of the falling body located at the unknown angle $\Theta_0$, and $u_1 = |\mathbf{u}_1|$ is the additional imbalance located under the known angle $\Theta_n$.

The imbalance (4.10) reaches a maximum when a zero difference occurs in the angular positions between the vectors $\mathbf{u}_0$ and $\mathbf{u}_1$ (Fig. 4.6).

In some cases when the imbalances $u_0$ and $u_1$ are essentially different in magnitude (Schneider (2003) recommends setting this ratio in a range 5 to 10), (4.10) can be reduced to the sine curve:

$$u_n \approx u_0 + u_1\cos(\Theta_n - \Theta_0)\ , \tag{4.11}$$

or

$$u_n \approx u_1 + u_0\cos(\Theta_n - \Theta_0)\ . \tag{4.12}$$

The first equation (4.11) is valid for $u_1 \ll u_0$ while the second one (4.12) can be used for $u_0 \ll u_1$. The maximal relative error of approximation for $\Theta_n = \Theta_0$ is of the order of $0.5(u_1/u_0)^2$ and $0.5(u_0/u_1)^2$ for (4.11) and (4.12), respectively.

For the sake of generality, we fit the curve (4.10) with three unknown parameters ($u_0$, $u_1$ and $\Theta_0$) to the measured imbalances $u_n$ using the weighted non-linear fitting option in the software package Origin™. The obtained solutions, namely the values $u_L = u_0$ and $\alpha = \Theta_0$ or $u_Q = u_0$ and $\beta = \Theta_0$, are then used to recalculate the final results (4.6) – (4.9).

### 4.2.3 Results

The actual position of the OC in the housing (Fig. 4.3(a)) was derived using the above-mentioned coordinate measuring machine. Its conventional procedure allows to measure the hollow corner cube's apex coordinates in the Cartesian coordinate system. For this, each of the three surfaces of the hollow corner cube are contacted at 16 different points by a spherical probe (Renishaw, model SP25). This gives results of the length measurements relative to the well-defined reference plane. Three geometrical surfaces (planes in this case) are then fitted to the measured coordinate data. The calculated point of intersection of these planes gives the apex of the corner cube. Hence, the results of measurements are the OC coordinates $x_{OC}$, $y_{OC}$ and $z_{OC}$ (Table 4.1). To compare with the results of the COM determination in the polar coordinate system, the OC coordinates are recalculated into the eccentricities and angles, using Eqs. (4.4) and (4.5) (cf. Table 4.1).

Balancing of the falling body was performed in a few iterations according to the procedure described in Subsection 4.2.2. Finally, in each of the orthogonal planes the imbalance was measured six times for each of the twelve angular positions of the additional mass. These results are given in Tab. 4.1 and shown in Fig. 4.7 together with the curve (4.10), fitted to the measured imbalances. The fitted values are $u_L = (14.10 \pm 0.02)$ g mm, $\alpha = (103.43 \pm 1.06)^\circ$ (rotation around the $z$-axis) and $u_Q = (14.43 \pm 0.02)$ g mm, $\beta = (247.35 \pm 1.33)^\circ$ (rotation around the $x$-axis). If the simplified model (4.11) is used, the differences in the estimated parameters are within 1%, which is acceptable for some applications. In our case the ratio $u_1/u_0 \approx 0.12$ leads to the maximal relative error of approximation (4.11) of the order of 0.7%. To avoid this, we use the general model (4.10).

For the mass of the falling body $m = 121.61$ g the eccentricities $e_L$ and $e_Q$ from (4.6) are 115.93 $\mu$m and 118.64 $\mu$m respectively. The coordinates of the COM are calculated using Eqs. (4.7). The total distance $R = 43.2$ $\mu$m is obtained from equation (4.9). All the uncertainties, listed in Tab. 4.1, are derived in the following sections.

Assume a maximum value for the angular velocity $\omega = 10$ mrad s$^{-1}$ during free fall (Niebauer *et al.*, 1995) and an expanded uncertainty of the distance between

centres $U_R = 74.7$ $\mu$m (cf. Table 4.1)[1]. Then, according to (4.2), the expanded uncertainty of $g$, resulting from such a rotation, is given by $U_g = \omega^2 U_R \approx 0.7$ $\mu$Gal. This is well within the acceptable performance limit for modern free-fall absolute gravimeters.

**Table 4.1:** Results of the COM to the OC adjustment.

| | Eccentricities/$\mu$m | | Angles/degrees | | Coordinates/$\mu$m | | |
|---|---|---|---|---|---|---|---|
| | $e_Q$ | $e_L$ | $\beta$ | $\alpha$ | $x$ | $y$ | $z$ |
| OC | 114.2 | 117.1 | 271.3 | 102.7 | -25.8±1.5 | 114.2±1.5 | -2.5±1.6 |
| COM | 118.6±13.5 | 115.9±3.5 | 247.4±1.4 | 103.4±1.1 | -26.9±2.3 | 112.8±3.4 | -45.7±5.8 |
| Distance between centres in each coordinate | | | | | -1.1±2.8 | -1.4±3.8 | -43.2±6.0 |
| Total distance between centres in 3D space | | | | | | 43.2±15.7 | |
| Expanded uncertainty ( $k = 2$) of the distance between centres in 3D space | | | | | $U_R = 43.24 + 2 \times 15.72 = 74.68$ | | |

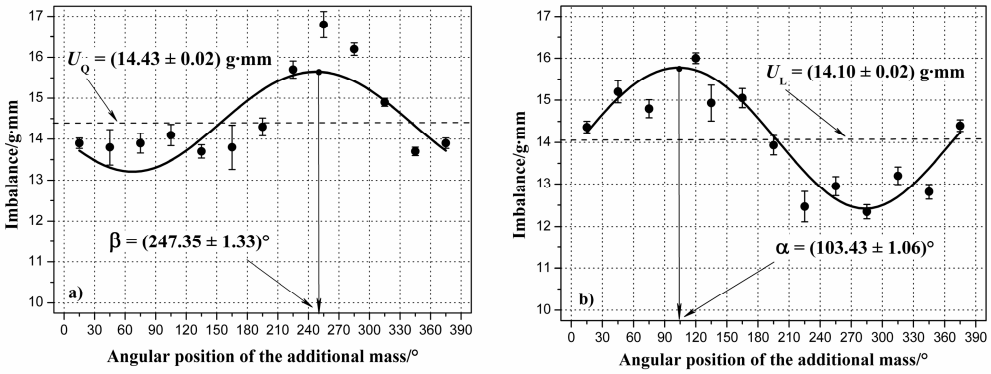


**Figure 4.7:** Results of the imbalance measurements when rotating around the $x$-axis (a) and the $z$-axis (b). Dots are measured values with the statistical standard deviations shown as error bars. The smooth line is the fitted sine curve (4.10). Obtained values of the imbalances and angles are reported with the standard errors derived from the weighted least square fitting.

[1]We use the symbol $U$ with the subscripts for the expanded uncertainty. The symbol $u$ with the subscripts is for the imbalance.

### 4.2.4 Uncertainty analysis

#### 4.2.4.1 Propagation of uncertainty

The measurement equations are given by (4.6) – (4.9). Let the coordinates of the OC ($x_{OC}$, $y_{OC}$, $z_{OC}$) be known with the standard uncertainties $\sigma_{x,OC}$, $\sigma_{y,OC}$ and $\sigma_{z,OC}$. Let the eccentricities $e_L$ and $e_Q$ be derived from (4.6) with the standard uncertainties $\sigma_L$ and $\sigma_Q$. These latter uncertainties combine statistical errors after the weighted non-linear least squares fitting of the curve (4.10) with known erroneous imbalances and eccentricities. Angles $\alpha$ and $\beta$ are derived from the same least squares fitting with the standard uncertainties $\sigma_\alpha$ and $\sigma_\beta$, which combine statistical errors after fitting with an uncertainty due to misalignment of the coordinate systems. Then from (4.7) and (4.8), following the law of uncertainty propagation (ISO, 1995), we obtain the standard uncertainties of the COM coordinates

$$\begin{aligned} \sigma_{x,COM} &= \sqrt{(e_L \sin\alpha)^2\sigma_\alpha^2 + (\cos\alpha)^2\sigma_L^2}\,, \\ \sigma_{y,COM} &= \sqrt{(e_L \cos\alpha)^2\sigma_\alpha^2 + (\sin\alpha)^2\sigma_L^2}\,, \\ \sigma_{z,COM} &= \sqrt{(e_Q \sin\beta)^2\sigma_\beta^2 + (\cos\beta)^2\sigma_Q^2} \end{aligned} \tag{4.13}$$

and the standard uncertainties of the differences between the centres in each coordinate:

$$\begin{aligned} \sigma_{\Delta x} &= \sqrt{\sigma_{x,COM}^2 + \sigma_{x,OC}^2}\,, \\ \sigma_{\Delta y} &= \sqrt{\sigma_{y,COM}^2 + \sigma_{y,OC}^2}\,, \\ \sigma_{\Delta z} &= \sqrt{\sigma_{z,COM}^2 + \sigma_{z,OC}^2}\,. \end{aligned} \tag{4.14}$$

In the case when all coordinates of the COM are obtained independently, the standard uncertainty $\sigma_R$ of the total distance $R$, derived from (4.9), is

$$\sigma_R = \sqrt{\frac{\Delta x^2\sigma_{\Delta x}^2 + \Delta y^2\sigma_{\Delta y}^2 + \Delta z^2\sigma_{\Delta z}^2}{\Delta x^2 + \Delta y^2 + \Delta z^2}}\,. \tag{4.15}$$

Note that in our case, the $x$- and $y$-coordinates of the COM were calculated using the same measured values $e_L$ and the angle $\alpha$ (see (4.7)). Hence, the input

quantities $\Delta x$ and $\Delta y$ in (4.9) are not independent, and the estimation of the standard uncertainty by (4.15) can not be used. To overcome the problem, we take this correlation into account (Sommer & Siebert, 2006). For this we first substitute the measured imbalance $u_L$ through the eccentricity $e_L$ with the angle $\alpha$ directly into equation (4.9) and then calculate the standard uncertainty of the total difference between the centres. With equations (4.7), (4.8) and (4.9) we obtain:

$$R^2 = e_L^2 + x_{OC}^2 - 2e_L\sqrt{x_{OC}^2 + y_{OC}^2}\sin(\alpha+\phi) + y_{OC}^2 + (z_{COM} - z_{OC})^2 \ , \quad (4.16)$$

where

$$\phi = \begin{cases} \arctan\left(\frac{x_{OC}}{y_{OC}}\right), & \text{if} \quad y_{OC} \geq 0 \\ \pi + \arctan\left(\frac{x_{OC}}{y_{OC}}\right), & \text{if} \quad y_{OC} < 0\,. \end{cases} \quad (4.17)$$

Note that now measurement equation (4.16) does not contain the correlated results $x_{COM}$ and $y_{COM}$. The standard uncertainty of the total distance $R$ between the centres is then derived from (4.16) as

$$\sigma_R = \frac{1}{R}\Bigg\{ e_L^2\Big[\sigma_L^2 + \Big(\sin(\alpha+\phi)\Big)^2\sigma_{OC}^2\Big] + x_{OC}^2\Big(\sigma_{x,OC}^2 + S_{xy}^2\Big) + y_{OC}^2\Big(\sigma_{y,OC}^2 + S_{xy}^2\Big) + \Big(z_{COM} - z_{OC}\Big)^2\sigma_{\Delta z}^2\Bigg\}^{\frac{1}{2}} , \quad (4.18)$$

where

$$\begin{aligned} \sigma_{OC}^2 &= \frac{\left(x_{OC}^2\sigma_{x,OC}^2 + y_{OC}^2\sigma_{y,OC}^2\right)}{(x_{OC}^2 + y_{OC}^2)} \ , \\ S_{xy}^2 &= \Big(\sin(\alpha+\phi)\Big)^2\sigma_L^2 + \Big(e_L\cos(\alpha+\phi)\Big)^2\left(\sigma_\alpha^2 + \sigma_\phi^2\right) \ , \\ \sigma_\phi &= \frac{\sigma_{OC}}{|y_{OC}|} \ , \\ \sigma_{\Delta z}^2 &= \sigma_{z,OC}^2 + (e_Q\sin\beta)^2\sigma_\beta^2 + (\cos\beta)^2\sigma_Q^2 \ . \end{aligned} \quad (4.19)$$

Numerical values of the contributing uncertainties are calculated below.

#### 4.2.4.2 OC coordinates

Experimental standard errors of the OC coordinates $x_{OC}$, $y_{OC}$ and $z_{OC}$, derived according to the procedure of Subsection 4.2.2, are 0.14 $\mu$m, 0.13 $\mu$m and 0.22 $\mu$m, respectively. In addition, the specified MPE of the coordinate measuring machine is $\Delta L = \pm(2.5+L/300)$ $\mu$m, where $L$ is the measured distance in millimetres. For the longest measured distance $L = 50$ mm, from the reference plane to the points of contact with the surfaces of the retroreflector, the MPE is $\Delta L = \pm 2.67$ $\mu$m. This corresponds to an equivalent standard deviation of 1.54 $\mu$m (assuming a uniform probability distribution). The combined uncertainties are thus $\sigma_{x,OC} = 1.55$ $\mu$m, $\sigma_{y,OC} = 1.54$ $\mu$m and $\sigma_{z,OC} = 1.56$ $\mu$m.

#### 4.2.4.3 Misalignment of the coordinate systems

To estimate the possible systematic effect through the misalignment of the polar axis and the $x$-axis or $z$-axis (cf. Fig. 4.6), we consider the tolerance limits, given in the fabrication process of the falling body or the mounting jigs. The tolerance value of $\pm 0.5^\circ$ corresponds to an equivalent standard deviation of $\pm 0.29^\circ$ for both axes of rotation (assuming a uniform probability distribution). Combined with the statistical standard errors of the measured angles, shown in Fig. 4.7, we obtain the standard errors $\sigma_\alpha = 1.10^\circ$ and $\sigma_\beta = 1.36^\circ$.

#### 4.2.4.4 Mass values

The mass of the falling body $m = 121.61$ g is required to convert the measured imbalance into the eccentricity (4.6). It is also necessary to know a value of the calibration mass ($\tilde{m}_C = 0.590$ g)[1] to calibrate the balancing machine. We measured these masses using commercial analytical balances, which are specified for such values of mass according to the high accuracy class II with a MPE of $\pm 0.10$ g and $\pm 0.001$ g, respectively. These values correspond to equivalent relative standard deviations of $\sigma_m/m \approx 4.8 \times 10^{-4}$ and $\sigma_{m_C}/m_C \approx 9.8 \times 10^{-4}$ (assuming a uniform probability distribution).

[1] In Subsections 4.2.4.4 and 4.2.4.5 we denote an estimate $\tilde{x}$ (random variable) for the measured quantity $x$ (unknown but fixed value).

#### 4.2.4.5 Balancing machine calibration

In order to derive the scale factor $C$ of the balancing machine, we compare its readings with and without the calibration mass $m_C$ attached to the falling body at the radial distance $r_C$ from the axis of rotation. When rotating with the angular velocity $\Omega_C$, the centrifugal force $\tilde{F}_C = m_C r_C \tilde{\Omega}_C^2$ acts on the inertial mass of the vibration sensor $m_S$. Hence, with the estimated scale factor (sensitivity) of the vibration sensor $\tilde{K}_S$, the measured acceleration is $\tilde{a}_C = \tilde{K}_S(\tilde{F}_C/m_S) = \tilde{K}_S m_C r_C \tilde{\Omega}_C^2/m_S$. Calibration of the balancing machine, with the given values of the dynamic stiffness of the rotor and foundation, gives an estimate $\tilde{C}$ of

$$\tilde{C} = \frac{\tilde{m}_C \tilde{r}_C}{\tilde{a}_C} = \frac{\tilde{m}_C \tilde{r}_C m_S}{\tilde{K}_S m_C r_C \tilde{\Omega}_C^2} \,. \tag{4.20}$$

The estimates $\tilde{m}_C$ and $\tilde{r}_C$ are inquired to input by the software of the balancing machine. Hence, in (4.20) the estimates $\tilde{m}_C$, $\tilde{r}_C$, $\tilde{K}_S$ and $\tilde{\Omega}_C$ are the random variables and the values $m_S$, $m_C$ and $r_C$ are fixed constants.

There are two groups of uncertainties in the estimate $\tilde{C}$ for the scale factor $C$. The first relates to the uncertainty of the calibration imbalance due to the uncertainties in the calibration mass and the calibration radius. The second is due to the measurement imbalance, shown by the balancing machine, which includes the amplitude non-linearity of the vibration sensor (or uncertainty of the estimated scale factor $\tilde{K}$ over an operating amplitude range) and non-stable angular velocity $\tilde{\Omega}$. From (4.20), the combined relative standard uncertainty of the scale factor $C$ is

$$\frac{\sigma_C}{C} = \sqrt{\left(\left(\frac{\sigma_{K_S}}{K_S}\right)^2 + \left(\frac{\sigma_{m_C}}{m_C}\right)^2 + \left(\frac{\sigma_{r_C}}{r_C}\right)^2 + \left(2\frac{\sigma_\Omega}{\Omega}\right)^2\right)} \,. \tag{4.21}$$

The amplitude non-linearity of the vibration sensor is specified to be within $\pm 1\%$, which corresponds to an equivalent relative standard deviation $\sigma_{K_S}/K_S \approx 5.77 \times 10^{-3}$, where the uniform probability distribution is assumed. The relative standard deviation of the calibration mass is $\sigma_{m_C}/m_C \approx 9.8 \times 10^{-4}$. The value of the calibration radius is $r_C = (16 \pm 0.1)$ mm, where the tolerance is given by the tolerance limits in fabrication of the falling body. Due to design considerations, we assume that the COM of the screw, being wound in as the calibration mass,

is within $\pm 0.1$ mm of the calibration radius. Hence the total relative standard deviation of the calibration radius is $\sigma_{r_C}/r_C = (0.2/\sqrt{6})/16 \approx 5.10 \times 10^{-3}$ (a triangular probability distribution is assumed). The nominal value of the rotational velocity during calibration is $\Omega_C = 1537$ rpm, but during measurements it varied within $\pm 10$ rpm. Thus, the corresponding relative standard deviation of the angular velocity is $\sigma_\Omega/\Omega \approx 3.76 \times 10^{-3}$ (the uniform probability distribution is assumed). Finally, the combined relative standard uncertainty of the balancing machine scale factor is $\sigma_C/C \approx 10.81 \times 10^{-3}$.

The estimate for the scale factor $\tilde{C}$ is used as a constant $C$ during measurements to convert the vibrational accelerations to the imbalance units: $\tilde{u} = \tilde{C}a$. Hence, a systematic contribution from the calibration of the balancing machine to the combined uncertainty of any measured imbalance $\tilde{u}$ can be calculated as $\sigma_{u,C} = (\sigma_C/C)\tilde{u} = 10.81 \times 10^{-3}\tilde{u}$. With the measured imbalances $\tilde{u}_L = 14.10$ g mm and $\tilde{u}_Q = 14.43$ g mm (cf. Fig. 4.7), we get $\sigma_{L,C} = 0.15$ g mm and $\sigma_{Q,C} = 0.16$ g mm.

#### 4.2.4.6 Dynamic imbalances

Here we collect erroneous imbalances which are caused by imperfect geometry of both the falling body and the balancing machine. During free fall, the falling body rotates around its COM. On the other hand, while balancing, the body rotates around the fixed rotational axes ($x$ and $z$, cf. Fig. 4.3). Since these axes are not exactly perpendicular to each other, the position of the COM can have an offset from the rotational axes by an amount $\Delta r_\perp$. The resulting error in imbalance will be $\Delta u_\perp = m\Delta r_\perp$, where $m$ is the mass of the falling body. From the tolerance limits given in the fabrication process, we estimate $\Delta r_\perp = \pm 2.5$ $\mu$m. The corresponding standard deviation in imbalance is then $\sigma_{u,L}$ gmm for each axis of rotation (assuming a uniform probability distribution).

During balancing the mounting jigs themselves produce some additional imbalance. Without the falling body attached, the measured values of the imbalances are $u_{Q,m.j.} = 2.3$ g mm and $u_{L,m.j.} = 0.5$ g mm, for different axes of rotation. When balancing the falling body, the angular position of the mounting jigs' imbalance can have one of many different angular values, which are uniformly

distributed over the whole period. Since the magnitudes of these imbalances (2.3 g mm and 0.5 g mm) are much less then the imbalance of the falling body (near 14 g mm), equation (4.11) can be considered. Then the effect of such an imbalance is approximately a root mean square value of the sine curve (4.11) with the amplitudes equal to the measured imbalances of the mounting jigs, (assuming a U-shaped probability distribution). This yields standard deviations of the mounting jigs' imbalance 1.64 g mm and 0.35 g mm, when rotating about the $x$-axis and $z$-axis, respectively. The relatively large value, when rotating about the $x$-axis, explains an observed discrepancy between the measured imbalance and the fitted curve (Fig. 4.7(a)). Assuming that suitable materials, speed of rotation and fixing methods are properly chosen, the uncertainties due to possible changes in the dynamic stiffness of the falling body, bearings and foundation can be neglected.

Table 4.2 lists all uncertainty components of the measured imbalances (as discussed in previous sections).

**Table 4.2:** Uncertainty budget of the measured imbalance.

| Source of uncertainty | Standard uncertainty/g mm | |
|---|---|---|
| | $u_Q$ | $u_L$ |
| Calibration of the balancing machine | 0.16 | 0.15 |
| Measured value of the imbalance: | | |
| repeated observations | 0.02 | 0.02 |
| imbalance of the mounting jigs | 1.64 | 0.35 |
| non-perpendicularity of the rotational axes | 0.18 | 0.18 |
| Combined standard uncertainty | 1.64 | 0.42 |

#### 4.2.4.7 Calculated eccentricities

From equations (4.6), the combined standard uncertainty of the calculated eccentricity depends on the uncertainty of the measured imbalance and the uncertainty of the mass of the falling body:

$$\sigma_e = e\sqrt{\left(\frac{\sigma_u}{u}\right)^2 + \left(\frac{\sigma_m}{m}\right)^2} = \sqrt{\left(\frac{\sigma_u}{m}\right)^2 + \left(\frac{\sigma_m}{m}\right)^2 e^2}\,, \tag{4.22}$$

where the combined standard uncertainties of the measured imbalances are given in Tab. 4.2, the relative standard deviation of the mass of the falling body is

calculated in Subsection 4.2.4.4 and the eccentricities $e_Q$ and $e_L$ are shown in Tab. 4.1. Then the combined standard uncertainties of the calculated eccentricities are $\sigma_Q = 13.51$ $\mu$m and $\sigma_L = 3.48$ $\mu$m.

#### 4.2.4.8 COM coordinates and difference between the centres

With the combined standard uncertainties of the eccentricities $\sigma_Q$ and $\sigma_L$, the combined standard uncertainties of the COM coordinates and of the total distance between the centres can be calculated from Eqs. (4.13) and (4.18), respectively (cf Tab. 4.3). The expanded uncertainty of the total distance between centres is given by

$$U_R = |R| + k\sigma_R \,, \tag{4.23}$$

where $R = 43.24$ $\mu$m as calculated from (4.9) and $\sigma_R = 15.72$ $\mu$m as calculated from (4.18). For the sake of simplicity, the conventional value of the coverage factor $k = 2$ (Taylor & Kuyatt, 1993) is used here.

The combined uncertainty of the total distance in 3D space between the

**Table 4.3:** Uncertainty budget: COM and OC adjusted.

| Measured value | Standard uncertainty/$\mu$m | | |
|---|---|---|---|
| | $x$ | $y$ | $z$ |
| OC coordinates | 1.55 | 1.54 | 1.56 |
| COM coordinates | 2.30 | 3.43 | 5.82 |
| Difference between OC and COM coordinates | 2.77 | 3.76 | 6.02 |
| Total difference between centres in 3D space, combined standard uncertainty | | 15.72 | |
| Expanded uncertainty ($k = 2$) of the distance between centres in 3D space | | 74.68 | |

COM and OC is approximately 16 $\mu$m, while in each coordinate it is no more than 6 $\mu$m. Clearly, it is possible to reduce the expanded uncertainty $U_R$ (4.23) by further reducing the total distance between centres, because the resolution of this method in 3D space is of the order of 16 $\mu$m. It is important to note that the calculation of the combined standard uncertainty by (4.15) instead of (4.18), in case of correlated measurements in the $x$-$y$ plane, leads to the underestimated value of 6.0 $\mu$m instead of 15.7 $\mu$m.

## 4.3 Method of index balancing

The previous Section 4.2 explained how in a falling body (FB) the centre of mass (COM) and the optical centre (OC) can be superposed, which was done in three dimensions for the first time in this project. The distance between the two centres was reduced to 43 $\mu$m, with an uncertainty of 16 $\mu$m. The position of the optical centre was first measured with a coordinate measuring machine (CMM), and then the COM was shifted to that point with a balancing method. This method does away with the requirement that the OC has to lie in the geometrical centre of the falling body assembly.

This approach worked very well, and the results obtained with the FB were more than satisfactory (cf. Chapters 2 and 3). Nevertheless, we decided to go for an improved method. As already mentioned, the goal was to discontinue using a CMM to measure the position of the OC.

We designed a new FB for this purpose. An improved balancing method, with a more sophisticated balancing setup is applied by simply reducing the imbalance of the FB assembly to its geometrical centre, which now coincides within the tolerance limits given by the fabrication tolerances of the different parts of the assembly. Here, another hollow corner cube retroreflector is used, with the distributor providing the well-defined position of the OC relative to the external surface. The index balancing method is adopted from Schneider (2003).

### 4.3.1 Theory of index balancing

Let us consider a rotor with an imbalance $\mathbf{u}$. To balance the rotor with a balancing machine, it has to be fastened to the balancing machine with a mandrel (mounting jig). When measuring the mandrels imbalance without the rotor, the display of the balancing machine shows the imbalance $\mathbf{H}$ (angle $\alpha_H$ and amount of imbalance $|\mathbf{H}|$ after calibration of the balancing machine, see Fig. 4.8).

When measuring the imbalance of the rotor with the balancing-machine-mandrel-rotor assembly, the shown imbalance on the display is $\mathbf{A}$, which is the sum of the imbalance due to the mandrel $\mathbf{H}$ and the rotor $\mathbf{u}$ (cf. Fig. 4.9(a)).

Now, once the rotor is turned by 180° with respect to the mandrel and rebalanced the balancing machine shows a new imbalance $\mathbf{A}'$ (cf. Fig. 4.9(b)).

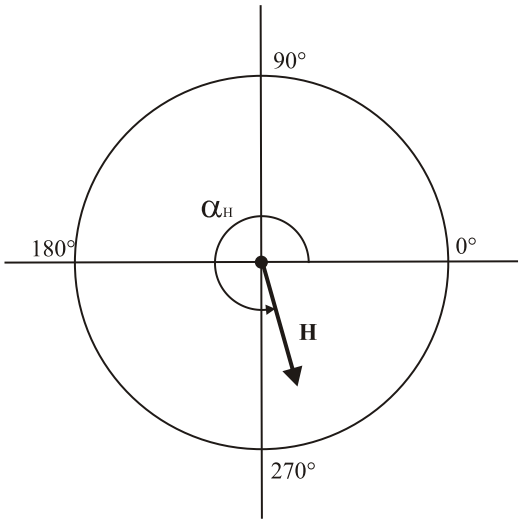


**Figure 4.8:** Imbalance of the mandrel without rotor.

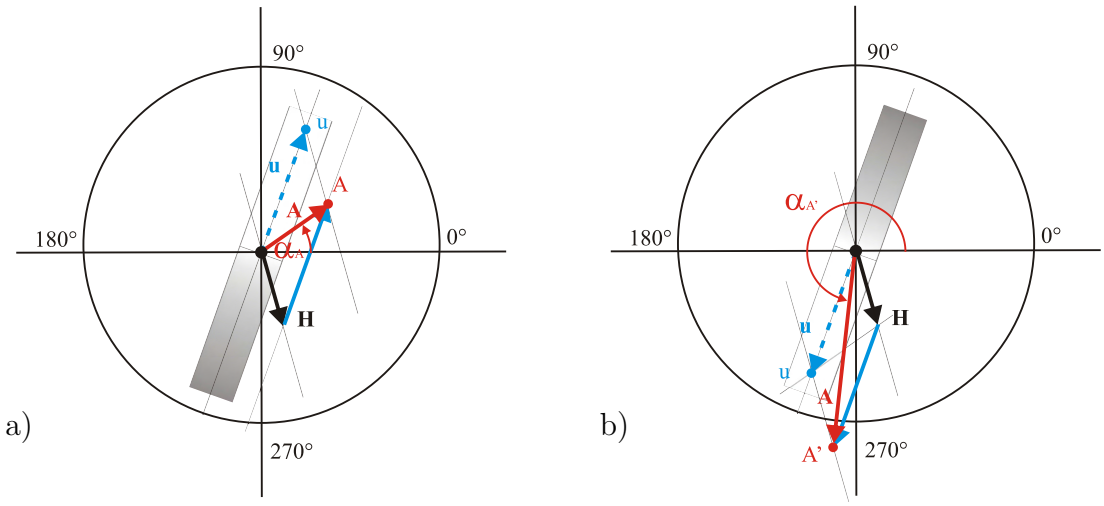


**Figure 4.9:** a) Imbalance of the mandrel with rotor. **A** is the net force, composed of the imbalance of the mandrel **H** and the imbalance of the rotor **u**. $u$ denotes the position of the COM of the rotor; b) Imbalance of the mandrel with rotor. The rotor is turned by 180°.

The imbalance of the rotor can now be reduced by shifting the COM of the whole assembly to the point $X$, which describes the midpoint of the distance between $A$ and $A'$ (cf. Fig. 4.10). With this sort of "differential balancing", the imbalance of the mandrel is excluded from the final result.

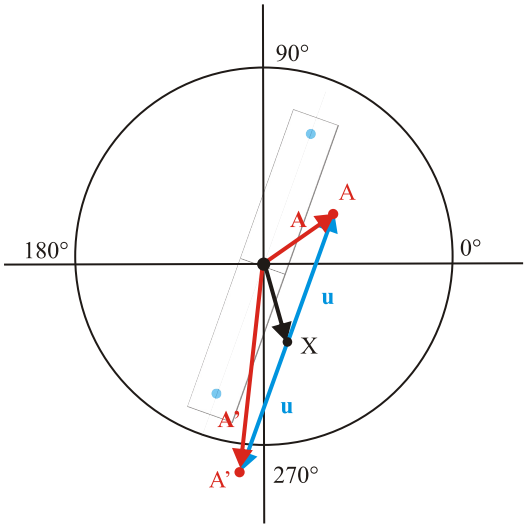


**Figure 4.10:** Imbalance of the rotor **u** can be calculated from the net imbalances **A** and **A′**. The imbalance of the mandrel is cancelled out.

Finally, the residual imbalance **u** can be calculated from the net imbalances **A** and **A′** by means of the equation

$$|\mathbf{u}| = \frac{|\mathbf{A} - \mathbf{A}'|}{2} \,. \tag{4.24}$$

#### 4.3.1.1 Eccentricity of the mounting jigs

Additionally to the imbalance of the mandrel, the point of support of the mounting jig can be offset from the axis of rotation. This eccentricity of the mounting jig with respect to the axis of rotation introduces another imbalance **E**, which will add up to the net imbalance **A**. However, again, this error is systematic and will be cancelled out by index balancing (cf. Figs. 4.11(a), 4.11(b) and 4.12).

### 4.3.2 Method

The idea for the new FB design was to make it easy to balance and avoid having to measure the OC with a CMM.

The first requirement “easy to balance” means that the COM of the FB should be shifted to the axis of rotation, i.e. the imbalance needs to be reduced. The advantage is, that it eliminates tedious recalculations of the actual position of

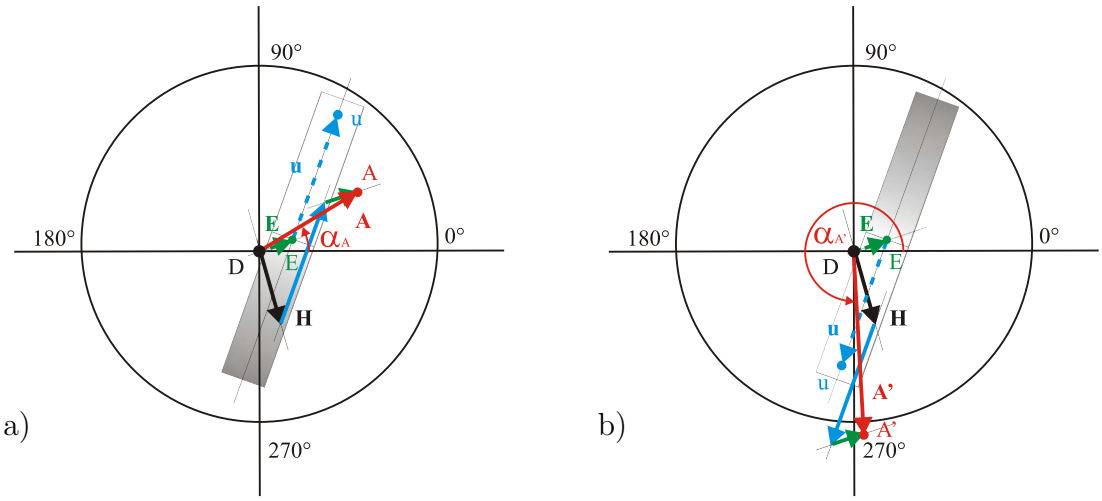


**Figure 4.11:** a) The imbalance **E** due to the eccentricity of the mounting jig with respect to the axis of rotation $D$ adds to the net imbalance **A**.; b) After turning the rotor by 180° the eccentricity of the mounting jig **E** with respect to the axis of rotation $D$ adds to the net imbalance $\mathbf{A}'$.

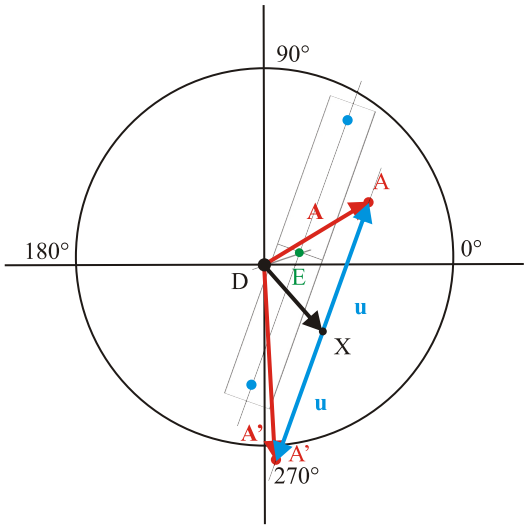


**Figure 4.12:** The imbalance of the rotor **u** can be calculated from the net imbalances **A** and $\mathbf{A}'$. The imbalance of the mandrel and the eccentricity are cancelled out.

the COM. Masses can be attached or reduced to minimize the imbalance. Hence, the housing of the FB should define three axes of rotation for balancing, and the position of the COM should coincide with the intersection point of the three axes

– defining the origin of a coordinate system (cf. Fig. 4.13).

The second requirement stipulates that the retroreflector should be placed

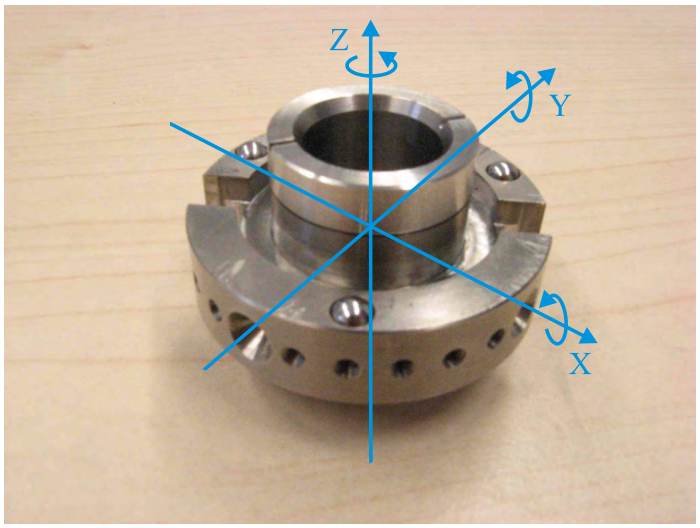


**Figure 4.13:** The figure shows the three rotation axes around which the FB will be balanced. The intersection point of the three axes coincides with the OC.

in the housing, and the OC of the retroreflector should coincide with the origin, defined by the housing, without the need of measuring the position of the OC after assembling the FB.

To master these requirements, we took a ball-mounted hollow retroreflector (BMR) (PLX Inc., BMR-0.875-1, USA, cf. Fig. 4.14(a) whose OC is centred with respect to the spherical surface to within 0.0001 inch (2.5 $\mu$m). Its ball diameter is 0.875 inches (22.2 mm), and its beam divergence is better than 10 arc seconds.

The next step was to design the housing in a way that the BMR was fitted inside of it to a tight tolerance and the OC coincided with the intersection point of the three balancing axes (Fig. 4.13). The universal housing (cf. Fig. 4.14(b)) is made of titanium, and can be used normally as well as upside down, i.e. the laser can enter the ballistic block from above or from below. Figure 4.14(b) shows the tap holes and the counter mass. They are used to shift the COM of the FB, as described in Section 4.2.

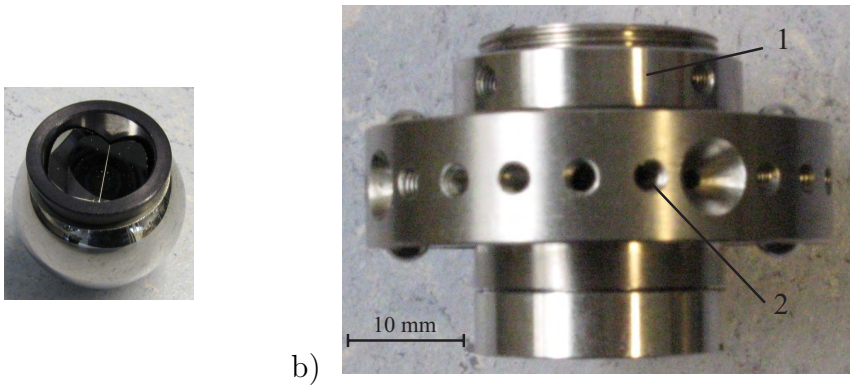


a) b)

**Figure 4.14:** Falling body of the absolute gravimeter: a) ball mounted hollow retro-reflector (BMR); b) housing of the BMR (1 - counter mass, 2 - tap hole).

Once the BMR is mounted inside the housing, the FB can be balanced. Therefore special mounting jigs are constructed (Fig. 4.15) which fit exactly to a commercial balancing machine (Micro Präzision Marx GmbH, model BMT 200 S, Germany, cf. Fig. 4.16). The balancing machine has a feedback control for the

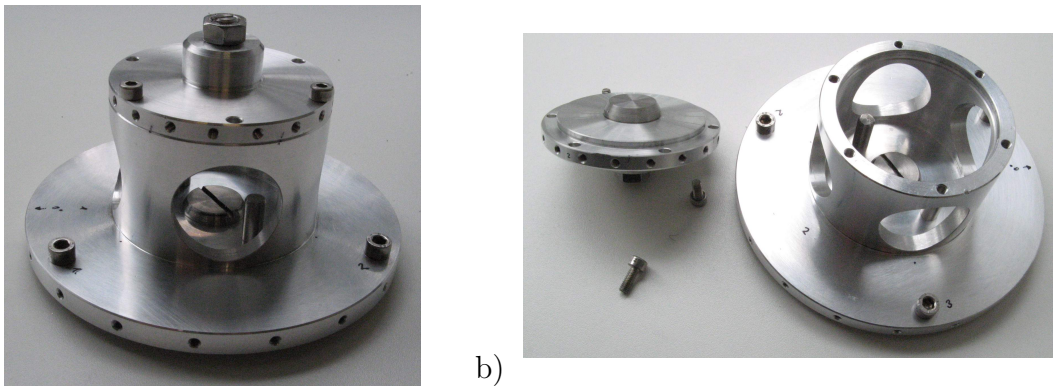

a) b)

**Figure 4.15:** A special mounting jig is designed for balancing the FB: the mounting jig for balancing around the $Z$-axis is shown a) when it is closed; b) when it is open, the conical shapes of the supports are seen which centres the FB to the axis of rotation of the balancing machine.

rotation speed, which allows stable rotation velocities of up to $(2000 \pm 0.5)$ rpm. After attaching the mounting jig to the balancing machine, the balancing machine is calibrated by putting a defined bias mass at a defined angular position and a defined distance from the axis of rotation. Next the bias mass is removed and the

mounting jig is balanced without the FB. This is done by winding screws in or out of the mounting jig (the mounting jig contains tap holes). When the residual imbalance of the mounting jig is reduced to a minimum, the FB is mounted inside the mounting jig, and the whole setup is balanced again. This is done around all three axes, as proposed in Section 4.2, to reduce the uncertainty. Balancing around the $X$- and $Y$-axis can be done with one setup, however for balancing around the $Z$-axis another mounting jig has to be fixed to the balancing machine. The index balancing method as described in Section 4.3.1 is applied for

**Figure 4.16:** Balancing machine BMT 200 S (modified) with the mounting jig for balancing around $X$- and $Y$-axis mounted.

balancing. This means that during the balancing procedure the FB is put into the mounting jig in a defined position, and then the imbalance is measured. This gives the imbalance value $A$ at an angular position $\alpha_A$. Then the FB is turned around by 180° and the net imbalance is measured again. This will give another value for the net imbalance, say $A'$ at a different angle $\alpha_{A'}$. The imbalance $\mathbf{u}$ now can be reduced by shifting the net imbalance to the point $X$ (Fig. 4.10). This is done for the mounting jigs alone as well as for the FB in all three dimensions.

When the FB's imbalance is reduced to a minimum, the final imbalance is measured by the method of index balancing and, combined with a method explained in Section 4.2.2 to enhance the resolution:

A bias mass is attached to the rotor at up to 16 different angular positions $\alpha_n$ and the imbalance $u_n$ is measured. The bias mass is chosen in a way that it produces an imbalance of a factor of 5 to 10 times the residual imbalance $u$ (Schneider, 2003). This is done again by index balancing, i.e. with the FB in two positions, turned by 180°. Hence, for each axis two diagrams are obtained, to which a curve of type (4.10) is fitted. The respective curve is fitted to the data and the values for the imbalances $A_{X,Y,Z}$, $A'_{X,Y,Z}$, and the angular positions of the residual net imbalances $\alpha_{A_X,A_Y,A_Z}$, and $\alpha_{A'_X,A'_Y,A'_Z}$ can be calculated for each axis respectively. The final residual imbalances of the FB $u_{X,Y,Z}$ are obtained by first converting the polar coordinates into Cartesian coordinates with the formulae[1]

$$\begin{aligned} a_x &= |\mathbf{u}_A| \cos \alpha_A \\ a_y &= |\mathbf{u}_A| \sin \alpha_A \ , \end{aligned} \tag{4.25}$$

and

$$\begin{aligned} a'_x &= |\mathbf{u}_{A'}| \cos \alpha_{A'} \\ a'_y &= |\mathbf{u}_{A'}| \sin \alpha_{A'} \ . \end{aligned} \tag{4.26}$$

Its difference gives

$$\begin{aligned} \Delta x &= a_x - a'_x \\ \Delta y &= a_y - a'_y \ , \end{aligned} \tag{4.27}$$

and finally for the imbalance of the FB in the respective plane we have (4.24)

$$|\mathbf{u}_{X,Y,Z}| = \frac{\sqrt{\Delta x^2 + \Delta y^2}}{2} = u_{X,Y,Z} \ . \tag{4.28}$$

To get the three dimensional displacement of the COM of the FB from the intersection point of the three axes of rotation we apply

$$e_{X,Y,Z} = \frac{u_{X,Y,Z}}{m} \ , \tag{4.29}$$

where $m$ is the final mass of the FB.

The final distance $R$ between the OC and the COM is then obtained from

$$R = \sqrt{e_X^2 + e_Y^2 + e_Z^2} \ . \tag{4.30}$$

[1]Lower case letters $x$ and $y$ denote the components of the 2-dimensional vector. Upper case letters $X$, $Y$, $Z$ denote the axis the balancing is done around.

### 4.3.3 Results

The OC's actual position in the housing is given by the precise construction of the housing and the BMR and coincides, to within an uncertainty, with the intersection point of the three rotation axes (Fig. 4.13).

Balancing was performed as described in Section 4.3.2 for each dimension and two different positions of the FB. Due to the stability of the rotational velocity of the balancing machine, for each position of the bias mass, just one measurement was performed. The results for each axis are shown in figure 4.17 together with the fitted curve (4.10). Table 4.4 shows the fitted values with their standard errors.

**Table 4.4:** The fitted values obtained with the enhanced method.

| | With FB - position A | | With FB - position A' | |
|---|---|---|---|---|
| Balancing around | Imbalance $U_A$/g mm | Angle of imbalance $\alpha_A$/degree | Imbalance $U_{A'}$/g mm | Angle of imbalance $\alpha_{A'}$/degree |
| $X$-axis | 0.62 ± 0.01 | 302.67 ± 1.44 | 0.61 ± 0.01 | 116.94 ± 1.06 |
| $Y$-axis | 0.17 ± 0.01 | 115.53 ± 5.02 | 0.94 ± 0.01 | 157.74 ± 0.80 |
| $Z$-axis | 0.59 ± 0.01 | 114.83 ± 0.88 | 3.11 ± 0.01 | 350.03 ± 0.22 |

In order to calculate the 3-dimensional distance of the COM to the OC, Eqs. (4.25) to (4.28) are applied to the numbers listed in Tab. 4.4 to obtain the imbalances of the FB. The respective eccentricities are calculated with (4.29), where the final mass of the falling body $m = 124.84$ g is taken. Finally, the 3-dimensional distance is derived from (4.30):

$$\left.\begin{array}{lllll} X\text{-axis}: & \overset{(4.25)-(4.28)}{\Rightarrow} & u_X = 0.61\,\text{gmm} & \overset{(4.29)}{\Rightarrow} & e_X = \ \ 4.9\,\mu\text{m} \\ Y\text{-axis}: & \overset{(4.25)-(4.28)}{\Rightarrow} & u_Y = 0.82\,\text{gmm} & \overset{(4.29)}{\Rightarrow} & e_Y = \ \ 6.6\,\mu\text{m} \\ Z\text{-axis}: & \overset{(4.25)-(4.28)}{\Rightarrow} & u_Z = 1.73\,\text{gmm} & \overset{(4.29)}{\Rightarrow} & e_Z = 13.9\,\mu\text{m} \end{array}\right\} \overset{(4.30)}{\Rightarrow} \ R = 16.1\,\mu\text{m}\ . \tag{4.31}$$

All uncertainties will be derived in the next sections and are listed in Tab. 4.5.

Again, we assume a maximum angular velocity $\omega = 10\,\text{mrad}\,s^{-1}$ during free fall (Niebauer *et al.*, 1995) and an expanded uncertainty of the distance between

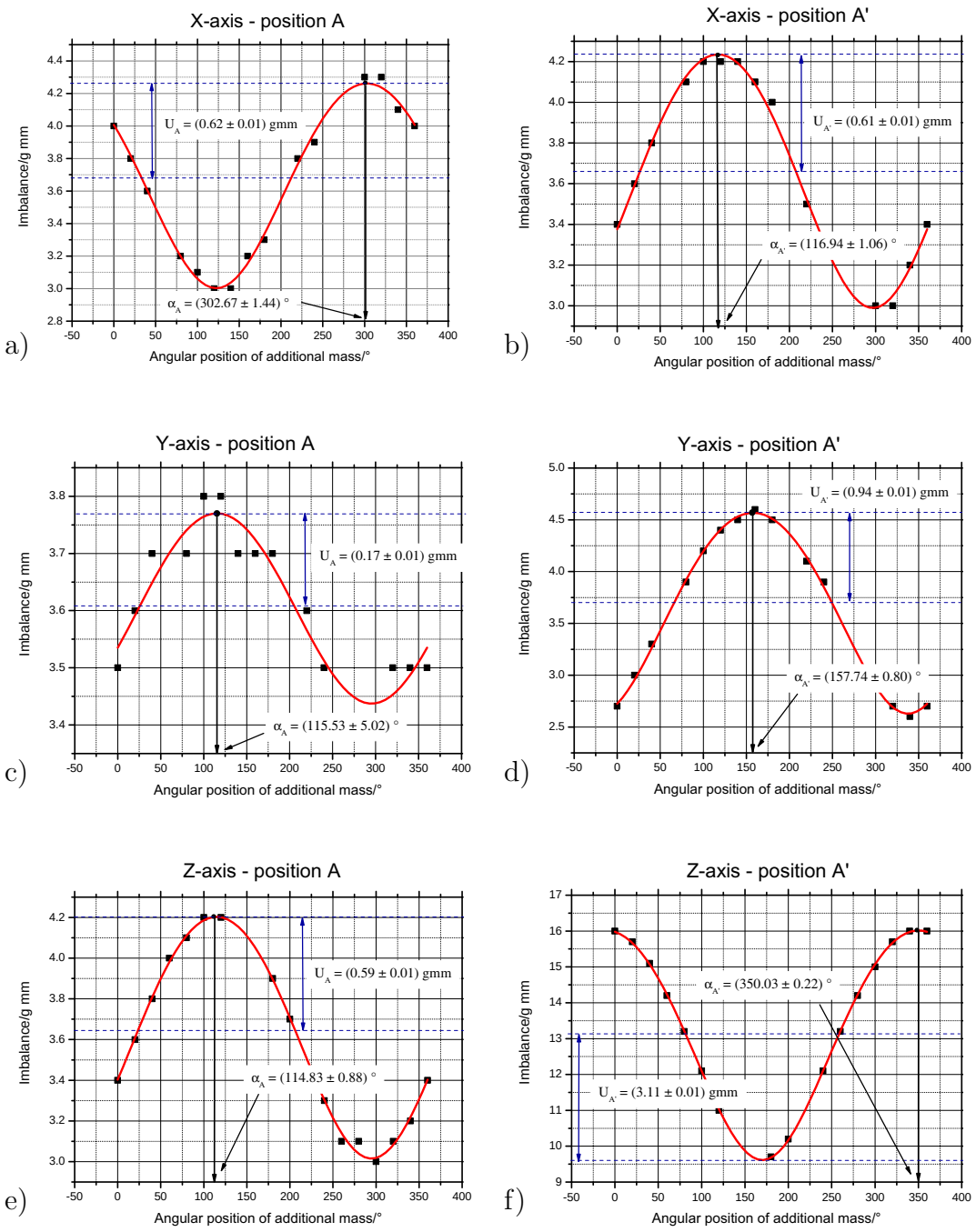


**Figure 4.17:** Results of the imbalance measurement when rotating around the $X$-axis ((a) and (b)), around the $Y$-axis ((c) and (d)), and around the $Z$-axis ((e) and (f)). The dots are the values measured. The solid lines are the fitted curves (4.10). The obtained values of the imbalances and angles are reported with the standard errors derived from the least squares fitting.

the centres $U_R = 39.1\ \mu\text{m}$[1]. Then, with (4.2), the expanded uncertainty of $g$, as the result of such a rotation, amounts to $U_g = \omega^2 U_R \approx 0.4\ \mu\text{Gal}$.

**Table 4.5:** Results of the centre of mass to the optical centre adjustment.

| | Eccentricities/$\mu$m | | |
|---|---|---|---|
| | $e_X$ | $e_Y$ | $e_Z$ |
| OC | 0 ± 6.50 | 0 ± 6.50 | 0 ± 6.50 |
| COM | 4.9 ± 1.2 | 6.6 ± 1.2 | 13.9 ± 1.4 |
| Total distance between centres in 3D space | | 16.1 ± 11.48 | |
| Expanded uncertainty ($k = 2$) of the distance between centres in 3D space | | $U_R = 16.1 + 2 \times 11.48 = 39.06$ | |

## 4.3.4 Uncertainty analysis

### 4.3.4.1 Propagation of uncertainty

The idea with the new FB design is to coincide the OC with the intersection point of the three balancing axes. A measurement of the OC's real position should be avoided. So the standard uncertainty of the OC position – the position coordinates will be called $x_{OC}$, $y_{OC}$, and $z_{OC}$ – is composed of the uncertainty of fabrication tolerance of the BMR and the uncertainty of the fabrication tolerance of the housing and will be called $\sigma_{x,OC}$, $\sigma_{y,OC}$, and $\sigma_{z,OC}$. The eccentricities of the COM are calculated from Eqs. (4.25) to (4.28) and will be called $e_X$, $e_Y$, and $e_Z$, with their respective uncertainties $\sigma_X$, $\sigma_Y$, and $\sigma_Z$. To calculate these eccentricities, the imbalances (absolute value and angle) are derived from the non-linear least squares fitting of (4.10). Following the law of uncertainty propagation (ISO, 1995), from (4.28) for the uncertainty of the imbalances in each dimension we get

$$2\sigma_u = \sqrt{\left(\frac{\Delta x}{2u}\sigma_{\Delta x}\right)^2 + \left(\frac{\Delta y}{2u}\sigma_{\Delta y}\right)^2}\,, \tag{4.32}$$

[1]The symbol $U$ is reserved for the uncertainty, while the symbol $u$ is used as imbalance.

with $u = |\mathbf{u}|$.

The uncertainties $\sigma_{\Delta x}$ and $\sigma_{\Delta y}$ are derived from (4.27)

$$\begin{aligned} \sigma_{\Delta x} &= \sqrt{\sigma_{a_x}^2 + \sigma_{a'_x}^2} \\ \sigma_{\Delta y} &= \sqrt{\sigma_{a_y}^2 + \sigma_{a'_y}^2} \ , \end{aligned} \tag{4.33}$$

and with the uncertainties $\sigma_{a_x}$, $\sigma_{a_y}$, $\sigma_{a'_x}$, and $\sigma_{a'_y}$ obtained from (4.25) and (4.26)

$$\begin{aligned} \sigma_{a_x} &= \left[(\sigma_{u_A} \cos\alpha_A)^2 + (u_A \sin\alpha_A \sigma_{\alpha_A})^2\right]^{\frac{1}{2}} \\ \sigma_{a_y} &= \left[(\sigma_{u_A} \sin\alpha_A)^2 + (u_A \cos\alpha_A \sigma_{\alpha_A})^2\right]^{\frac{1}{2}} \ , \end{aligned} \tag{4.34}$$

and

$$\begin{aligned} \sigma_{a'_x} &= \left[(\sigma_{u_{A'}} \cos\alpha_{A'})^2 + (u_{A'} \sin\alpha_{A'} \sigma_{\alpha_{A'}})^2\right]^{\frac{1}{2}} \\ \sigma_{a'_y} &= \left[(\sigma_{u_{A'}} \sin\alpha_{A'})^2 + (u_{A'} \cos\alpha_{A'} \sigma_{\alpha_{A'}})^2\right]^{\frac{1}{2}} \ . \end{aligned} \tag{4.35}$$

As the eccentricities of all three dimensions are independent, the standard uncertainty $\sigma_e$, derived from (4.30), is

$$\sigma_e = \sqrt{\frac{e_X^2 \sigma_{e_X}^2 + e_Y^2 \sigma_{e_Y}^2 + e_Z^2 \sigma_{e_Z}^2}{{e_X}^2 + {e_Y}^2 + {e_Z}^2}} \ . \tag{4.36}$$

#### 4.3.4.2 OC coordinates

As the real position of the OC was not measured, the uncertainty of its position with respect to the intersection point of the balancing axes is obtained from the fabrication tolerances of the housing, as well as the BMR.

The BMR is fabricated in a manner that the OC is centred to within 2.5 $\mu$m with respect to the outer ball surface. This gives an uncertainty of $\frac{(2.5\ \mu\text{m}/2)}{\sqrt{3}\sqrt{3}} = 0.42\ \mu$m for each dimension. The fabrication tolerance of the ball diameter is 5 $\mu$m; hence has an uncertainty of 2.9 $\mu$m, and the combined standard uncertainty for the BMR amounts to $\sigma_{BMR} = 3.24\ \mu$m.

The housing, on the other hand, is fabricated in a way that the BMR fits exactly into it, and the OC coincides with the intersection point of the balancing axes. The fabrication tolerance of the housing (i.e. its inner diameter; cf. Fig.

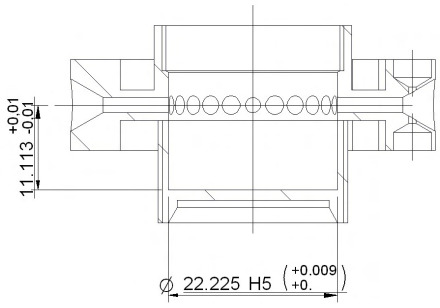


**Figure 4.18:** Fabrication tolerances for the housing.

4.18) is +9 $\mu$m (uncertainty = $9/(2\sqrt{3}) = 2.6$ $\mu$m), whereas the depth tolerance is $\pm 10$ $\mu$m (uncertainty = 5.8 $\mu$m). For simplicity is sake we take the uncertainty $\sigma_{housing} = 5.8$ $\mu$m for all three dimensions.

It follows that the combined standard uncertainty for the OC coordinates then is 6.65 $\mu$m for each dimension.

#### 4.3.4.3 Mass values

As already described in Section 4.2.4.4 the mass of the FB $m = 124.84$ g is required to convert the measured imbalances into the eccentricities (4.29). The same balances were used to weigh the FB and the calibration mass ($m_C = 3.01$ g). Assuming a uniform probability distribution, the values corresponding to the equivalent relative standard deviations are $\sigma_m/m \approx 4.6 \times 10^{-4}$ and $\sigma_{m_C}/m_C \approx 1.9 \times 10^{-4}$, respectively.

#### 4.3.4.4 Calibrating the balancing machine

To estimate the uncertainty due to the calibration of the balancing machine, we follow the same arguments as in Section 4.2.4.5. The only difference to the given uncertainty of the scale factor is that the uncertainty due to the angular velocity is now negligible, as the motor of the balancing machine is feed back controlled. Hence, the combined relative standard uncertainty of the scale factor can be estimated to

$$\frac{\sigma_C}{C} = \sqrt{\left(\frac{\sigma_{K_S}}{K_S}\right)^2 + \left(\frac{\sigma_{m_C}}{m_C}\right)^2 + \left(\frac{\sigma_{r_C}}{r_C}\right)^2}\,, \tag{4.37}$$

where the same values as in section 4.2.4.5 can be taken:
amplitude non-linearity of the vibration sensor – $\sigma_{K_S}/K_S \approx 5.77 \times 10^{-3}$;
relative standard deviation of the calibration mass – $\sigma_{m_C}/m_C \approx 9.8 \times 10^{-4}$;
Total standard deviation of the calibration radius – $\sigma_{r_C}/r_C = (0.2/\sqrt{6})/240 \approx 3.4 \times 10^{-4}$, with the calibration radius $r_C = 240 \pm 0.1$ mm and a triangular probability distribution assumed.

The uncertainties of the measured imbalances resulting from the uncertainty of machine calibration are listed in Tab. 4.6 under the category *Calibrating the balancing machine*.

#### 4.3.4.5 Dynamic imbalances

The dynamic imbalances are cancelled out due to the index balancing method.

#### 4.3.4.6 Calculated eccentricities

The combined standard deviation of the calculated eccentricities depends after (4.29) on the standard deviation of the measured imbalance and the standard deviation of the mass of the FB:

$$\sigma_{e_{X,Y,Z}} = e_{X,Y,Z}\sqrt{\left(\frac{\sigma_{u_{C(X,Y,Z)}}}{u_{C(X,Y,Z)}}\right)^2 + \left(\frac{\sigma_m}{m}\right)^2}, \tag{4.38}$$

where the combined standard deviations of the measured imbalances $u_C$ are shown in Tab. 4.6. With the standard deviation of the mass, derived in section 4.3.4.3, the combined standard deviations of the calculated eccentricities are $\sigma_{e_X} = 1.9$ $\mu$m, $\sigma_{e_Y} = 1.9$ $\mu$m, and $\sigma_{e_Z} = 2.0$ $\mu$m.

#### 4.3.4.7 COM coordinates and difference between the centres

With this balancing method, we shift the COM to the origin of our coordinate system. It should be noted that the labels of the eccentricities given in (4.31) do not correspond to the axes shown in Fig. 4.13, i.e. $e_X$ is not the eccentricity along the $X$-axis, but the eccentricity in the $Y$-$Z$-plane. We are not interested in the exact position of the COM within the FB, although we would be able to calculate it. Our aim is to approximate the centres as closely as possible, that in

**Table 4.6:** Uncertainty budget of the measured imbalance.

| Source of uncertainty | Standard uncertainty/g mm | | | | | |
|---|---|---|---|---|---|---|
| | X | | Y | | Z | |
| | A | A' | A | A' | A | A' |
| Calibrating the balancing machine | $3.6\times10^{-3}$ | $3.5\times10^{-3}$ | $1.0\times10^{-3}$ | $5.4\times10^{-3}$ | $3.4\times10^{-3}$ | $18.0\times10^{-3}$ |
| Measured value of the imbalance: repeated observations | 0.01 | 0.01 | 0.01 | 0.01 | 0.01 | 0.01 |
| Combined standard uncertainty | 0.01 | 0.01 | 0.01 | 0.01 | 0.01 | 0.02 |

the optimum case is coincided with the origin.

The expanded uncertainty of the total distance between the OC and the COM is given by

$$U_R = k\sigma_R \,, \tag{4.39}$$

where from (4.31) we have for $R = 16.1$ $\mu$m, and (4.36) $\sigma_e$ gives 11.73 $\mu$m. For simplicity, we choose a coverage factor $k = 2$ (Taylor & Kuyatt, 1993). Hence, the distance between the centres with the expanded uncertainty amounts to $U_R = (16.1 + 2 \times 11.73)$ $\mu$m $= 39.56$ $\mu$m. The uncertainty budget for the adjusted centres is shown in Tab. 4.7.

**Table 4.7:** Uncertainty budget: COM and OC adjusted.

| | Standard uncertainty/$\mu$m | | |
|---|---|---|---|
| Measured value | $X$ | $Y$ | $Z$ |
| OC coordinates | 6.50 | 6.50 | 6.50 |
| COM coordinates | 1.2 | 1.2 | 1.4 |
| Difference between optical centre and centre of mass coordinates | 6.61 | 6.61 | 6.65 |
| Total difference between centres in 3D space, combined standard uncertainty | | 11.48 | |
| Expanded uncertainty ($k = 2$) of the distance between centres in 3D space | $U_R = 16.1 + 2 \times 11.48 = 39.06$ | | |

## 4.4 Conclusion

This Chapter presented two methods to coincide the positions of the COM and the OC of the falling body for an absolute gravimeter. With the first method the total distance between the centres in 3D space is approximately 43 $\mu$m with a combined standard uncertainty of 16 $\mu$m. This result is presently sufficient for our newly developed absolute gravimeters, where the expanded uncertainty of the measured $g$ value, due to the effect of rotation of the falling body, is less than 1 $\mu$Gal.

With known relative positions of both centres in 3D space, it is possible to calculate a rotation correction, using (4.1). For this, the rotation of the falling body during free fall should be recorded, as discussed regarding the FG5 absolute gravimeter (Niebauer *et al.*, 1995). With this correction applied, the expanded uncertainty of the measured $g$ value due to rotation will be reduced to $U_g = \omega^2(2\sigma_R) \approx 0.3$ $\mu$Gal. As a result, the rejection level of the rotational velocity can be increased, more drops will be accepted and the dropping mechanism's lifetime will be extended.

The reported study regards a hollow corner cube. Nevertheless, the proposed balancing method can be extended to the case of a corner cube prism if the coordinates of the corner cube prism's OC are known (Peck, 1948). It is also expected that the method can be used in other applications where precision balancing is required.

The second method presented here employs an improved balancing method. The resolution of 11.48 $\mu$m is better than with the first method and good enough for most absolute free fall gravimeters. For many years, the error due to the displacement of the two centres was one of the biggest contributions to the absolute gravimeter's uncertainty budget (Hanada, 1988; Hanada *et al.*, 1996; Niebauer *et al.*, 1995). We have shown that with our method this is no longer the case. The easy assemble and balancing makes the construction of the FB straight forward. If the FB's housing is damaged, the retroreflector can easily be placed inside another housing. Our innovation makes it possible to build a more cost-efficient alternative to the admittedly expensive contemporary gravimeters, since

it allows more drops to be realized without fear of abrading the FB.

# Chapter 5

# Uncertainty budgets and possible errors

Since a gravimeter is designed to measure an *absolute* value, it is necessary to assign the measurement apparatus an accuracy to which the *real value* can be measured. This is known as an uncertainty budget. However, for common measuring devices such as rulers, clocks, etc. the real value can be given as it is determined by a *primary standard*. For gravimeters, however, this is not possible. No such primary standard exists. Gravity is not constant, neither in space nor in time. A calibration is impossible. History showes (as in the case of the inverted pendulum in Potsdam; cf. Sec. 1.2.1) that assumedly highly precise apparatuses can turn out to be highly inaccurate once a new method is invented that permits comparing systematic errors. The higher the targeted accuracy, the more difficult it is to give a complete uncertainty budget.

The error sources considered in this chapter are already treated in the literature (D'Agostino, 2005; Niebauer *et al.*, 1995; Zumberge, 1981) and will be applied to our gravimeter setups. The uncertainty of the FB rotation, however, is described in more detail, since a new method was invented in the course of this dissertation, so a separate Chapter 4 is dedicated to this subject. Additionally, the uncertainty due to the non-linearity of electronics (cf. Subsection 5.1.15) is studied in more detail and cannot be found elsewhere in this form, as well as the estimation of the uncertainty due to the residual ground vibrations in subsection 5.1.12.

The uncertainty budget falls into two categories. Uncertainty factors due to the instrument and due to environmental effects. The uncertainty budgets apply to both gravimeters, MPG-1 and MPG-2.

## 5.1 Uncertainty budget due to the instrument

In general, it is very difficult to measure all of the physical effects that can influence the measurement. In this section we will use simplified models to estimate what uncertainties arise from the measurement apparatus itself.

### 5.1.1 Vacuum

The errors due to residual air inside the ballistic block can be put into three different categories. The air drag effect, the outgassing of the falling body (FB), and the buoyancy acting on the FB.

#### 5.1.1.1 Air drag

During the drop, the FB experiences a resistance due to residual air molecules. The force acting on the FB can be estimated according to Niebauer *et al.* (1995) to give

$$F_d = \frac{A\rho V}{4} v \ , \tag{5.1}$$

where $A \approx 117.8 \times 10^{-4}$ m$^2$ is the total surface area of the FB, $v \approx 2.3$ (1.6) m s$^{-1}$ is the maximum velocity of the FB for MPG1 (MPG2), $V \approx 476$ m s$^{-1}$ is the mean gas velocity for gas molecules of $N_2$, and $\rho \approx 0.5 \times 10^{-11}$ kg m$^{-3}$ is the mean gas density. The mean gas density is calculated by

$$\rho = \frac{m_r p}{k_B T} \ . \tag{5.2}$$

Here $m_r = (2 \times 14)/(6.022 \times 10^{23}) \approx 4.65 \times 10^{-23}$ g is the relative molecular mass of diatomic nitrogen, $k_B$ is the Boltzmann constant (cf. Appendix A), $T \approx 300$ K room temperature, and $p \approx 3 \times 10^{-6}$ ($2 \times 10^{-4}$) Pa is the pressure in the ballistic block of MPG-1 (MPG-2). With the mass $m \approx 0.121$ kg of the FB, the biasing acceleration $\Delta g_d = F_d/m$ due to air drag amounts to $1.33 \times 10^{-2}$ (4.0) $\mu$Gal for

MPG-1 (MPG-2). Since the model is not very precise, we assume an uncertainty of 20% of the correction value. This gives $0.3 \times 10^{-2}$ (0.8) $\mu$Gal for MPG-1 (MPG-2).

The bias and the resulting uncertainty for MPG-2 are clearly too high. The future plan is to place the motor outside of the dropping chamber. This will allow the use of copper gaskets and thus pumping to a higher vacuum level.

**Table 5.1:** Uncertainty budget for air drag.

| | Correction/$\mu$Gal | Standard uncertainty/$\mu$Gal |
|---|---|---|
| MPG-1 | $1.33 \times 10^{-2}$ | $0.3 \times 10^{-2}$ |
| MPG-2 | 4.0 | 0.8 |

#### 5.1.1.2 Outgassing

Another effect to consider is the outgassing of the FB. The pumping speed of the ion pump used for MPG-1 and MPG-2 is $dV/dt = 50\,\mathrm{l\,s^{-1}}$ and $20\,\mathrm{l\,s^{-1}}$, respectively. Starting from the ideal gas equation

$$m_{og} = m_m n = \frac{pV}{RT}\ , \tag{5.3}$$

where $m_{og}$ is the outgassing mass pumped off by the ion pump, $m_m = 29 \times 10^{-3}$ kg mol$^{-1}$ is the molar mass of air, $n$ is the number of air molecules, $p \approx 3 \times 10^{-6}$ ($2 \times 10^{-4}$) Pa is the pressure inside the dropping chamber of MPG-1 (MPG-2), $R$ is the molar gas constant (see appendix A), and $T \approx 300$ K is room temperature. Deriving (5.3) with respect to time gives the mass flux $Q = dm/dt = 1.7$ (46.4) $\times 10^{-12}$ kg s$^{-1}$. To calculate the outgassing of the FB the surface area of MPG-1 (MPG-2) is estimated to be $A_{MPG1} = 0.88$ m$^2$ ($A_{MPG2} = 0.24$ m$^2$). With the FB's surface of $A_{FB} = 117.8 \times 10^{-4}$ m$^2$ the relation between MPG1 (MPG2) and the FB's surface area is $r_{MPG1} = A_{FB}/A_{MPG1} = 1.3 \times 10^{-2}$ ($r_{MPG1} = A_{FB}/A_{MPG2} = 4.9 \times 10^{-2}$). Finally, the error in the measurement of $g$ is $\Delta g_{og} = (rQv)/m_{FB} = 4.2 \times 10^{-5}$ $\mu$Gal for MPG-1, and $\Delta g_{og} = (rQv)/m_{FB} = 3 \times 10^{-3}$ $\mu$Gal for MPG-2. Here, the velocity $v = 2.3$ (1.6) m s$^{-1}$, and the mass of the FB $m_{FB} \approx 0.121$ kg is used.

The numbers resulting from these estimations are very small and hence will be neglected in the uncertainty budget.

**Table 5.2:** Uncertainty budget for outgassing.

| | Correction/$\mu$Gal | Standard uncertainty/$\mu$Gal |
|---|---|---|
| MPG-1 | $4.2 \times 10^{-5}$ | negligible |
| MPG-2 | $3 \times 10^{-3}$ | negligible |

#### 5.1.1.3 Buoyancy

An estimation of the buoyancy effect is straightforward by using

$$\Delta g_{bu} = \frac{\rho_{fl}}{\rho_{FB}} g \ , \tag{5.4}$$

with $\rho_{fl} = 1.2 \times 10^{-9}$ kg m$^{-3}$ and $\rho_{FB} = 4.507 \times 10^{3}$ kg m$^{-3}$ are the density of the fluid (air for MPG2) and the FB (titanium), respectively. This is so small that it will also be neglected in our uncertainty budget.

### 5.1.2 Magnetic field

#### 5.1.2.1 Magnetic attraction

The measurements with MPG-2 at ECAG 2007 showed (cf. Sec. 3.4) that the magnetic field resulting from the ion pump gave rise to a big acceleration on the FB. The reason is that the balls that fit the FB into the vee-grooves of the support ring, are made of hardened steel (ball bearing balls). These balls are magnetic, albeit only slightly. The induced magnetic attraction caused an error in $g$ in the order of 500 $\mu$Gal. The best error reduction were achieved by moving the magnets of the ion pump – which are factory-shielded with a $\mu$-material – as far away from the dropping chamber as possible. Measurements of the stray magnetic field showed, that it decays very rapidly with growing distance. The residual magnetic field strength acting on the dropping chamber with the new setup is in the order of the natural Earth magnetic field. The magnetic field due to the ion pump is assumed to be zero, now, with a negligible error. The next generation of FBs is planned to contain no magnetic material at all. The balls will be made of ruby or ceramic.

#### 5.1.2.2 Eddy currents

Two objects in the setup produce magnetic field. Non-homogeneities of those fields could produce eddy currents in the FB, since it is made of conducting material. The eddy currents, in turn, produce a force that counteracts the motion of the FB. Such sources include the ion pump's magnet and the motor. The measured magnetic field around the dropping chamber, however, is in the order of the Earth's magnetic field, which is about 50 $\mu$T (0.5 G) in Central Europe. Following the estimation by Niebauer *et al.* (1995), and modelling the FB as a ring made of titanium, the induced force is of the order $F_{ec} = 1.3 \times 10^{-15}$ N, for a magnetic field strength of 1 mT. For our FB's mass ($m_{FB} = 121$ g), this would result in an acceleration of about $10^{-6}$ $\mu$Gal. Here, we adopt the attributed uncertainty to magnetic fields of 0.1 $\mu$Gal to our uncertainty budget.

**Table 5.3:** Uncertainty budget for eddy currents.

| | Correction/$\mu$Gal | Standard uncertainty/$\mu$Gal |
|---|---|---|
| MPG-1 | none | 0.1 |
| MPG-2 | none | 0.1 |

### 5.1.3 Electrostatic field

The dropping chambers of the MP gravimeters are made of stainless steel and aluminium. The only non-conducting parts are the glass windows at the top and the bottom, that allow the laser beam to enter the dropping chamber. For this reason the chamber functions as a Faraday cage surrounding the FB that shields it from external electrostatic fields. One problem to expect is formation of electric capacitance between the FB and the support ring. Murata (1978) and Niebauer *et al.* (1995) estimated already this effect to be negligible.

**Table 5.4:** Uncertainty budget for electrostatic field.

| | Correction/$\mu$Gal | Standard uncertainty/$\mu$Gal |
|---|---|---|
| MPG-1 | negligible | negligible |
| MPG-2 | negligible | negligible |

### 5.1.4 Influence of instrumental masses

As the gravitational force is a really weak force compared to other fundamental forces, most of the apparatus parts' influence on the FB are assumed to be negligible. On the other hand, this force has a very large range, as the measured influence of the Sun and Moon demonstrates. However, a brief calculation shows that for a spherical body of the mass $M = 0.2$ kg the gravitational attraction at a distance of $r$ =1 cm amounts, according to

$$g = \frac{GM}{r^2} \ , \tag{5.5}$$

to 13.3 $\mu$Gal, where $G$ is Newton's constant. In general, however, the part's shape differ from a sphere. A brief estimation should give an idea of what gravitational attraction the apparatus has on the FB. On the one hand, heavy parts would be expected to exert the most critical influence, but they would have to be very close to the FB to do so, on the other. We will estimate the gravitational acceleration due to the bottom plate of MPG-2, which weighs approximately 7 kg, and, as it is closest to it, the support ring on which the FB sits.

The bottom plate measures $0.42 \times 0.32$ m$^2$, with a thickness of $\Delta z = 0.02$ m, and is made of aluminium. We will model this square shaped plate as a disc with the radius $r = 0.15$ m. Its distance from the FB at the start-of-drop position is about $z_1 = 0.35$ m. The gravitational acceleration due to the bottom plate is given by

$$g_{bp} = G \iiint\limits_V \frac{\rho_{Al}}{q^2} \cos\alpha \ dV \ , \tag{5.6}$$

where $\alpha$ denotes the angle between the plumb line $z_1$ and the line $q$ between the FB and the mass particle $m_i$ (cf. Fig. 5.1). The integration goes over the volume $V$ of the bottom plate. As $\rho_{Al}$ is a constant, we can write it before the integral, and after inserting the limits of integration we get

$$g_{bp} = G\rho_{Al} \int_0^R \int_{z_1}^{z_1+\Delta z} \int_0^{2\pi} \frac{\cos\alpha}{q^2} \, r \, d\theta \, dr \, dz \ . \tag{5.7}$$

By substituting $q^2 = r^2 + z^2$ and $\cos\alpha = \frac{z}{q}$ this can be written as

$$g_{bp} = G\rho_{Al} \int_0^R \int_{z_1}^{z_1+\Delta z} \int_0^{2\pi} \frac{z}{(r^2+z^2)^{3/2}} \, r \, d\theta \, dr \, dz \ . \tag{5.8}$$

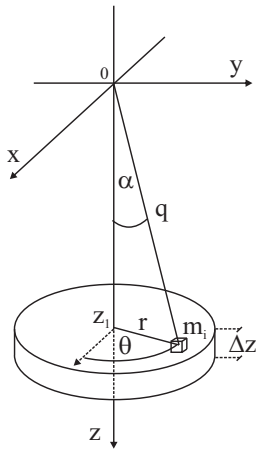


**Figure 5.1:** The gravitational attraction due to instrumental parts can be modelled by circular plates.

After performing the integration, the final expression for $g_{bp}$ becomes

$$g_{bp} = G\rho_{Al}2\pi \left( \Delta z + \sqrt{z_1^2 + R^2} - \sqrt{(z_1 + \Delta z)^2 + R^2} \right) . \tag{5.9}$$

When all values ($\rho_{Al} = 2.7 \times 10^3$ kg m$^{-3}$) are inserted, the acceleration amounts to 0.23 $\mu$Gal.

To estimate the attraction of the support ring, we use the same Eq. (5.8), but with $z_1 = 5 \times 10^{-3}$ m, $\rho_{St} = 8 \times 10^3$ kg m$^{-3}$ (for stainless steel), $\Delta z = 10 \times 10^{-3}$ m. Now, the integration limit for the radius covers the range from $r_1 = 17.5 \times 10^{-3}$ m to $r_1 + \Delta r$, with $\Delta r = 6 \times 10^{-3}$ m. The resultant acceleration amounts to only $0.34 \times 10^{-3}$ $\mu$Gal.

These brief calculations show that an uncertainty due to instrumental attraction of 0.5 $\mu$Gal is reasonable for MPG-2.

The influence in the case of MPG-1 seems more serious, as it is mounted on an optical table of about 500 kg of mass. The distance to the FB is approximately 1 m. We will remodel the table as a disc with the radius $r = 0.75$ m, and a thickness of $\Delta z = 0.45$ m. The mean density of the table amounts to roughly $\rho_{ot} = 630$ kg m$^{-3}$. A calculation with Eq. (5.8) results in an attraction of 1.8 $\mu$Gal. For a better calculation the exact density distribution of the optical table has to be known. As a correction we will give $-1.8$ $\mu$Gal for MPG-1, and an uncertainty of 0.5 $\mu$Gal.

**Table 5.5:** Uncertainty budget for instrumental masses.

| | Correction/$\mu$Gal | Standard uncertainty/$\mu$Gal |
|---|---|---|
| MPG-1 | -1.8 | 0.5 |
| MPG-2 | none | 0.5 |

### 5.1.5 Verticality of the laser beam

If the laser is not exactly aligned along the plumb line, a different effective wavelength results to measure $g$, thereby introducing an error $\Delta g$. Figure 5.2 demonstrates that the effective wavelength $\lambda_{eff}$ resulting from a misalignment angle $\Theta$, is given by

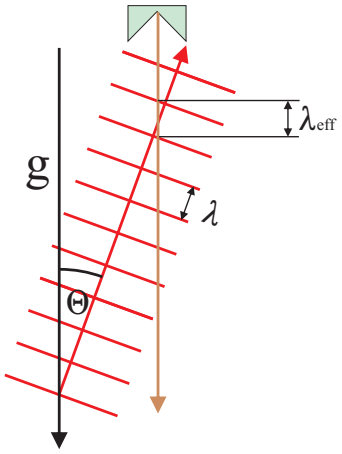


**Figure 5.2:** A deviation of the laser beam from the plumb line introduces an error in the $g$ measurement.

$$\lambda_{eff} = \lambda \cos\Theta \tag{5.10}$$

and leads to a measured value of $g_m = g\cos(\Theta) \approx g(1 - \frac{\Theta^2}{2})$, if a small angle is assumed. This means the measured acceleration due to gravity becomes lower than the "real" value. From (5.10) results that a beam deviation of 9 arcsec (equals 44 $\mu$rad) causes an error of 1 $\mu$Gal.

In order to minimize this error, the beam is aligned along $g$ by the method sketched in Fig. 5.3. The laser beam leaving the laser is reflected by mirror M and is split up into two beams by beam splitter BS1. Beam 1 hits the falling mirror (which is kept stationary during the alignment procedure), and then hits

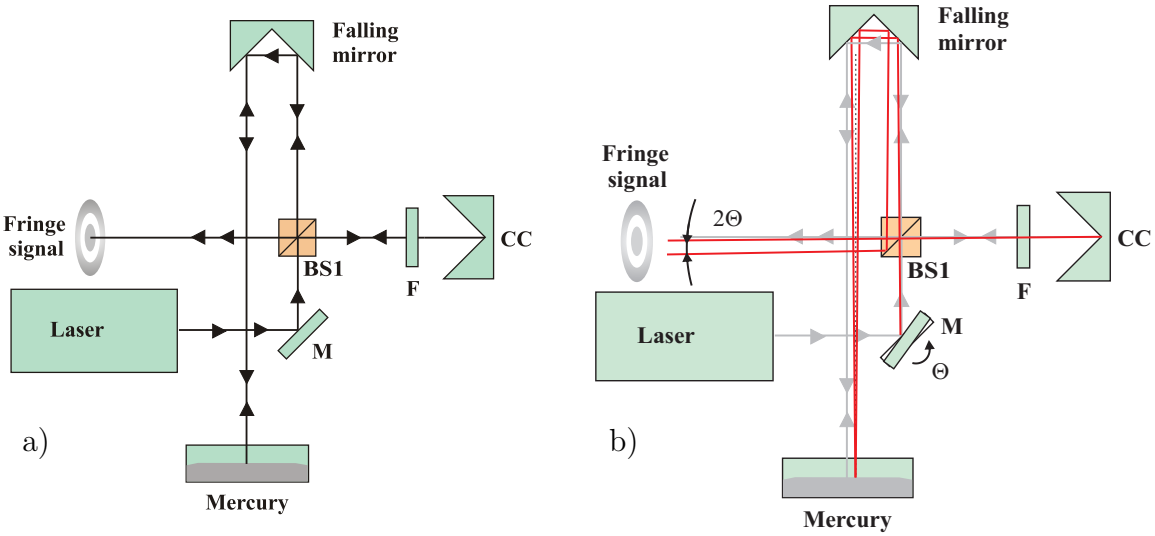


**Figure 5.3:** a) The verticality of the laser beam is aligned by reflecting the object beam on a mercury surface and watching the fringe signal. b) A tilt of the test beam can be estimated by the fringe signal formed on a screen.

the surface of a mercury (or ethanol) pool. This reflects beam 1 back to BS1. Beam 2 serves as a reference beam. It is reflected back by a corner cube mirror CC (the filter F is just to adjust the intensities of both beams) to BS1, where it is finally recombined with beam 1. The superposing beams form a fringe pattern, which contains information about the angle $\Theta$. For plane waves the angle can be estimated as shown in Fig. 5.4. So for small angles we can write

$$\sin(\Theta) = \frac{\lambda}{d} \approx \Theta \,, \tag{5.11}$$

where $\lambda = 633\,\text{nm}$ is the wavelength of the laser, $d$ is the distance between two fringes, and $\Theta$ is the deviation angle. In our case, the beam spot has a diameter of 3 mm and hence, if two fringes are visible on the screen, the resulting angle is 210 $\mu$rad, which corresponds to an error of $\frac{\Theta^2}{4} g = 11\ \mu$Gal (D'Agostino *et al.*, 2003). For the remaining uncertainty we assume a rectangular distribution (D'Agostino *et al.*, 2003), which gives $\sqrt{\frac{\Theta^4}{48}} g = 6\ \mu$Gal. A possible solution could be the use of an autocollimator to adjust the beam.

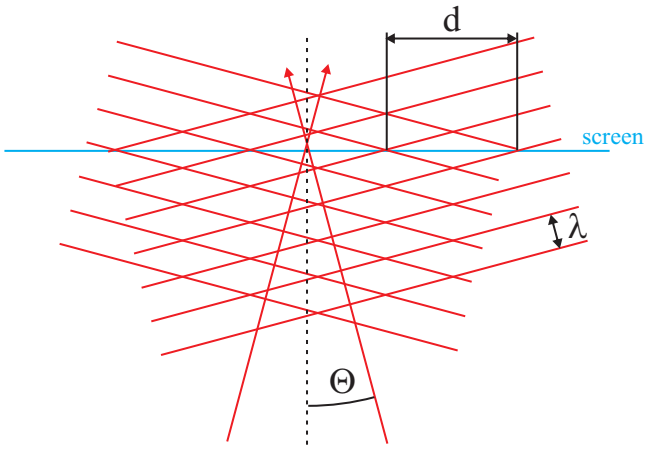


**Figure 5.4:** The beam deviation angle Θ can be estimated by measuring the distance $d$ between two fringes.

**Table 5.6:** Uncertainty budget for laser verticality.

| | Correction/$\mu$Gal | Standard uncertainty/$\mu$Gal |
|---|---|---|
| MPG-1 | 11 | 6 |
| MPG-2 | 11 | 6 |

### 5.1.6 Accuracy and stability of the laser

The trajectory of the FB is measured by counting the interference fringes produced in a Michelson interferometer, and so the measurement of the displacement of the FB directly depends on the stability of the laser frequency. For our gravimeters a Helium-Neon laser (Spectra Physics, A117, Newport) with a wavelength of 633 nm is used as a length standard. Its wavelength was measured with our institute's frequency comb.

Although the stability is not as good as that of an iodine stabilised HeNe laser,

**Table 5.7:** Length standard specifications.

| | |
|---|---|
| Frequency (measured) | 473 612 527 590 ± 77 kHz (min.) |
| Short-term frequency stability | < 100 kHz (typically) |
| | < 300 kHz (1 minute) |
| Long-term frequency drift | < 3 MHz (8 hours) |
| Temperature sensitivity | 0.5 MHz $^{\circ}C^{-1}$ |

we preferred it due to its compactness and easy handling. For the MPG1 setup,

the laser was used in a free space setup, but the MPG2 laser was fibre-coupled. This reduced the output power from $\approx 1.3\,\mathrm{mW}$ to $500\,\mu\mathrm{W}$, but is still good enough to get a fringe signal of an amplitude of $1\ \mathrm{V}_{pp}$. The specifications of the laser are listed in Tab. 5.7. Assuming a rectangular probability distribution, the uncertainty amounts to 3.64 $\mu$Gal.

This uncertainty is still too high. However, a prototype of a caesium stabilized diode laser (852 nm) was built at our institute by our colleague Dr. Jianwei Zhang to our specifications. First measurements of the laser showed accuracies in the order of $9 \times 10^{-11}$. An advantage over the usual iodine stabilized helium-neon lasers is that there is no modulation on the frequency, and an output power of several mW is no problem. We just started first $g$-measurements with the new laser, so they are not reported in the framework of the thesis.

**Table 5.8:** Uncertainty budget for laser stability.

| | Correction/$\mu$Gal | Standard uncertainty/$\mu$Gal |
|---|---|---|
| MPG-1 | none | 3.64 |
| MPG-2 | none | 3.64 |

### 5.1.7 Accuracy and stability of the atomic clock

The ADC-card used to digitize the fringe signal is disciplined by a rubidium frequency standard (SRS, FS725), giving a 10 MHz sine wave signal. Its accuracy is specified with $< 5 \times 10^{-11}$ (monthly) and $< 5 \times 10^{-10}$ (yearly) (cf. Tab. 5.9). The clock was calibrated at our institute and also compared to other standards during the ECAG 2007 in Luxembourg. Assuming a rectangular probability distribution, the error can be estimated to be less than 0.6 $\mu$Gal. As the main uncertainty arises from the drift, a frequent calibration, say every 6 months, should keep the error small. This can be done with other caesium clocks and the maser, which are available at our institute. Another possibility is to use a GPS-disciplined rubidium clock like the AR70 A series from AccuBeat Ltd., where the GPS signal guarantees the long term stability.

**Table 5.9:** Frequency standard specifications.

| | |
|---|---|
| Amplitude | 1 $V_{rms}$ ± 10% |
| Ageing | monthly: $< 5 \times 10^{-10}$ |
| | yearly: $< 5 \times 10^{-9}$ |
| Short-term stability | $< 2 \times 10^{-11}$ (1 s) |
| | $< 1 \times 10^{-11}$ (10 s) |
| | $< 2 \times 10^{-12}$ (100 s) |

**Table 5.10:** Uncertainty budget for clock stability.

| | Correction/$\mu$Gal | Standard uncertainty/$\mu$Gal |
|---|---|---|
| MPG-1 | none | 0.6 |
| MPG-2 | none | 0.6 |

### 5.1.8 Corner cube rotation

The minimisation of the error due to corner cube rotation was one of this work's key projects and is described in detail in Sections 4.2 and 4.3. The uncertainty derived in section 4.2 was 0.7 $\mu$Gal. The FB treated in Section 4.3 is not used in our gravimeters yet, and hence will not be shown in the uncertainty budget.

**Table 5.11:** Uncertainty budget for corner cube rotation.

| | Correction/$\mu$Gal | Standard uncertainty/$\mu$Gal |
|---|---|---|
| MPG-1 | none | 0.7 |
| MPG-2 | none | 0.7 |

### 5.1.9 Radiation pressure

The laser beam reflected by the FB transfers momentum to the FB and hence slows it down. For a total reflection, the force acting on the surface of the mirror is equal to $F = 2\Delta p/\Delta t = 2\Delta E/(c\Delta t) = 2P/c$, where $P \approx 0.5$ mW is the laser power (for the free space set up), $p$ is the momentum of a photon, and $c$ is the velocity of light. Dividing by the mass $m_{FB} = 0.121$ kg of the FB, the acceleration caused is $\approx 2.8 \times 10^{-3}$ $\mu$Gal.

**Table 5.12:** Uncertainty budget for radiation pressure.

| | Correction/$\mu$Gal | Standard uncertainty/$\mu$Gal |
|---|---|---|
| MPG-1 | none | $2.8 \times 10^{-3}$ |
| MPG-2 | none | $2.8 \times 10^{-3}$ |

### 5.1.10 Beam divergence

Even if the laser beam is collimated, diffraction causes the light waves to spread transversely. There is no such thing as a perfectly collimated beam. This diffraction, or spreading, results in a curved wavefront, so not all of the beam reaches the retroreflector aligned along $g$. The result is a bias in $g$ similar to the one mentioned in Subsection 5.1.5. This effect is well known and discussed in literature (Westrum & Niebauer, 2003).

To quantify the error caused by diffraction we can use the following equation, which is valid in the far field of the laser beam:

$$\frac{\Delta g}{g} = \frac{\lambda^2}{4\pi^2\omega_0^2} = \frac{\phi^2}{4} \,, \tag{5.12}$$

where $\lambda \approx 633$ nm denotes the laser wavelength, $\phi$ is half the angle of divergence, and $\omega_0$ is the beam waist, i.e. the radius of the beam at its smallest diameter (cf. Fig. 5.5). This means that when the divergence is measured, the error can be calculated and corrected. The divergence was measured by determining the beam

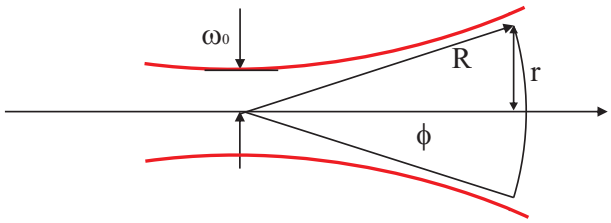


**Figure 5.5:** A collimated laser beam diverges. The radius at its smallest point is called beam waist radius $\omega_0$.

diameter at different positions in the far field. The beam diameter is defined as the diameter at which the intensity has fallen to $1/e^2$ (13.5%) of its peak value. A beam profiler from Coherent was used to measure the diameter at seven positions approximately 3 m away from the collimator, and with a distance of 5 cm between

the different positions. The result was an angle ($\phi = 250 \pm 84$) $\mu$rad, which gives a correction of $\Delta g = 22$ $\mu$Gal, and an uncertainty of $\sigma_{diff} = 1.8$ $\mu$Gal. It should be noted that the effect, as in the case of the beam verticality, always lowers the "real" $g$ value.

The uncertainty in $g$ due to the beam divergence is still too high. The best way to reduce this uncertainty is to use bigger beam diameters. A beam waist diameter of more than 3.2 mm is required for a correction of less than 1 $\mu$Gal. In the free space setup of MPG-1 the beam diameter was bigger than 5 mm and, hence, the error was smaller than 1 $\mu$Gal. However, for the uncertainty budget we will use the number derived from the fibre-coupled system.

**Table 5.13:** Uncertainty budget for beam divergence.

| | Correction/$\mu$Gal | Standard uncertainty/$\mu$Gal |
|---|---|---|
| MPG-1 | 22 | 1.8 |
| MPG-2 | 22 | 1.8 |

Here we note that together with the finite beam size of a Gaussian beam, there is also another phase shift – the Gouy phase shift – along the beam propagation direction. This phase shift may represent another source of systematic error and has not been considered in all previous works. The detailed analysis will be published elsewhere.

## 5.1.11 Temperature effects

### 5.1.11.1 Temperature gradient

If there is a temperature gradient between the top and the bottom of the FB during the drop, a pressure difference is induced. The pressure change can be calculated for an ideal gas as

$$\Delta p_{tg} = \frac{\Delta T}{T} p \,, \tag{5.13}$$

where $\Delta T$ is the difference in temperature between the ends of the FB, $T$ is the nominal temperature, $p$ is the nominal pressure inside the dropping chamber and

$\Delta p$ the induced pressure difference. This pressure difference causes a force that acts on the FB, and the uncertainty in $g$ can be calculated by

$$\sigma_{\Delta p_{tg}} = \Delta T \frac{P A_{FB}}{T M_{FB}} \,, \tag{5.14}$$

with $A_{FB} = (24\text{ mm})^2\pi$ denoting the cross-section area of the FB, and $M_{FB} = 121$ g its mass. By inserting the values $p_{MPG-1} = 2 \times 10^{-4}$ Pa, with the nominal temperature $T = 300$ K, a temperature-induced acceleration gradient for MPG-1 of $1.5 \times 10^{-2}$ $\mu$Gal K$^{-1}$ is obtained. Pessimistically assuming a temperature difference of 0.1 K, the resultant uncertainty amounts to $1.5 \times 10^{-3}$ $\mu$Gal. For MPG-2 the nominal pressure is $p_{MPG-2} = 3 \times 10^{-6}$ Pa, and, hence, the induced acceleration per 1 K amounts to $\approx 1\mu$Gal K$^{-1}$. Again assuming a temperature difference of 0.1 K over the length of the FB, the uncertainty is in the order of 0.1 $\mu$Gal.

**Table 5.14:** Uncertainty budget for temperature gradient.

| | Correction/$\mu$Gal | Standard uncertainty/$\mu$Gal |
|---|---|---|
| MPG-1 | none | $1.5 \times 10^{-3}$ |
| MPG-2 | none | 0.1 |

#### 5.1.11.2 Effects on the setup

By virtue of temperature changes a tilt of the optical table MPG-1 is placed on, was observed. This had an influence on the beam verticality, as the interferometer was placed on the table in case of MPG-1. A correction formula was derived from a long-term measurement. Figure 5.6 shows the good correlation between the temperature and tilts of the optical table. Figure 5.7 shows the correlation between the measured gravity values and temperature. The empirical correction formula, derived from the long-term measurement, is

$$\Delta g_T = \left(790.07 - \frac{32.5}{^\circ\text{C}}\, T\right) \,\mu\text{Gal} \,, \tag{5.15}$$

where $T$ is the temperature in °C. The correlation factor is $\rho = 0.647$ and hence significant. It can be seen in Fig. 5.7 that the change in $g$ ranges up to $\pm 40$ $\mu$Gal. Assuming an uncertainty of 10% of the maximum range as the uncertainty in $g$,

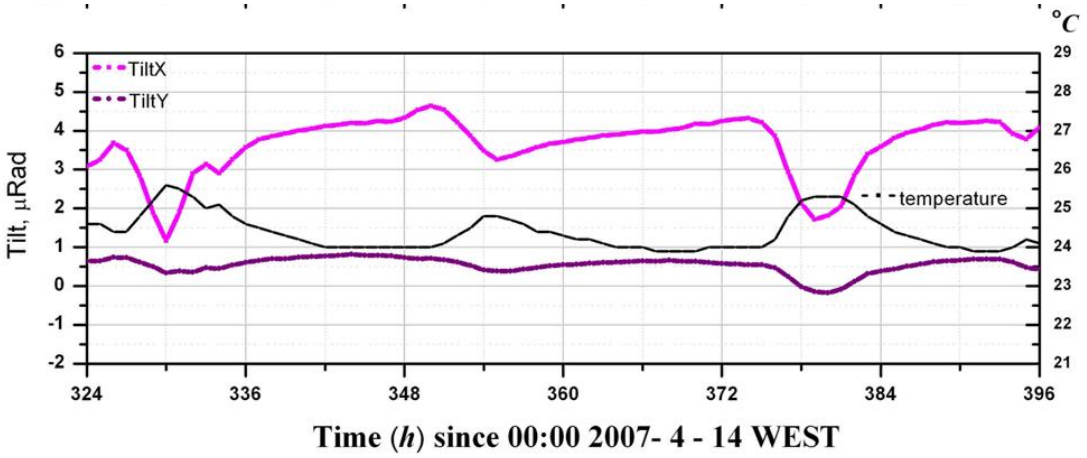


**Figure 5.6:** A change in room temperature causes a tilt of the optical table.

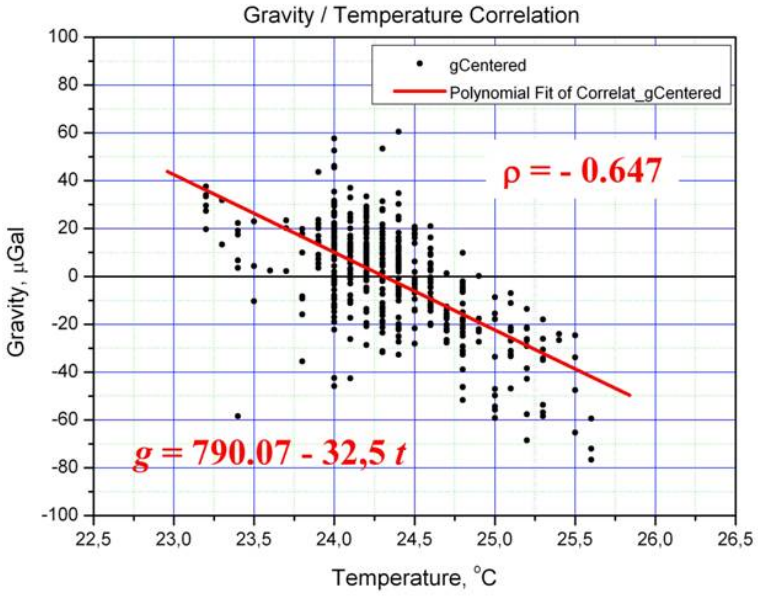


**Figure 5.7:** Correlation between gravity values and temperature. $\rho$ is the correlation factor.

this error contributes 4 $\mu$Gal to the uncertainty budget.

This effect was not observed for MPG-2. This has two reasons. First, MPG-2 is not installed on the optical table, and second, for MPG-2 a fibre-coupled laser is used.

The free space interferometer setup will be replaced in our further measurements with MPG-1. The interferometer will be placed directly on the super spring, as in the case for MPG-2, so this correction will become obsolete.

Another interesting point in this context is the laser beam pointing stability. As in the future only fibre-coupled setups will be used, it may not cause any serious problems, but in my opinion it is worth mentioning that laser pointing stability in free space setups is an error source not to be neglected. The error is similar to a misalignment of the verticality of the laser beam. Gray *et al.* (2001) investigated the problem of pointing stability for the Spectra-Physics 117A He-Ne laser. A peak-to-peak amplitude of 15 mrad ($\approx$ 56 mGal) could be shown for the first 200 s after turning on the laser. After the intensity stabilisation was established, the amplitudes were lower, but still up to 1.5 mrad ($\approx$ 560 $\mu$Gal). Furthermore oscillations were sensitive to temperature drifts just over 1 °C were observed.

The laser beam leaving a fibre should not have such a big pointing instability, but could be an interesting point for further studies.

### 5.1.12 Floor recoil and seismic vibrations

The measurement of the falling distance of the FB is a relative measurement. With the interferometer the distance of the reference mirror (the mirror of the Super Spring) to the beam splitter is compared to the distance of the retroreflector in the FB to the beam splitter. The aim is to measure the trajectory of the FB in an inertial system. This inertial system, however, is just realizable to a certain extent. If the reference mirror oscillates, the measurement is biased. A gravimeter can be considered as a low pass filter with a corner frequency given by (Svetlov, 1997)

$$f_c \approx \frac{0.8}{T} \,, \tag{5.16}$$

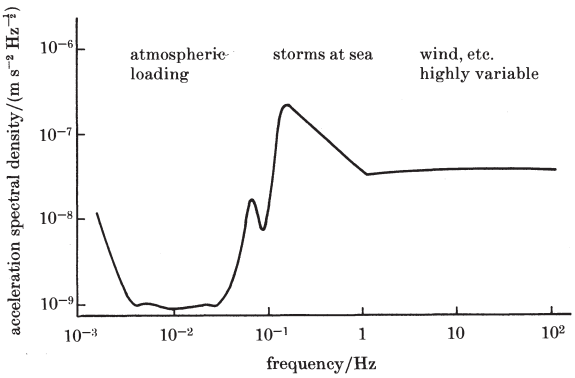


**Figure 5.8:** Ground vibration acceleration spectrum of a quiet site; normalized spectrum.

where $T$ is the drop time. For our gravimeters this corner frequency is about 10 Hz and 4 Hz for MPG-2 and MPG-1, respectively. Torge (1989) quantifies the natural microseismics caused by marine surge with periods of 1 to 10 s, and amplitudes of 0.1 to 10 $\mu$m. A typical amplitude spectral density plot is given in Fig. 5.8 following Speake (1987). A corner frequency of 10 Hz means that all seismic noise below this frequency penetrates the measurement. The Super Spring does good work here isolating the reference mirror from microseismic noise. Since it has a period of 60 s, it shifts the corner frequency of the low pass filter

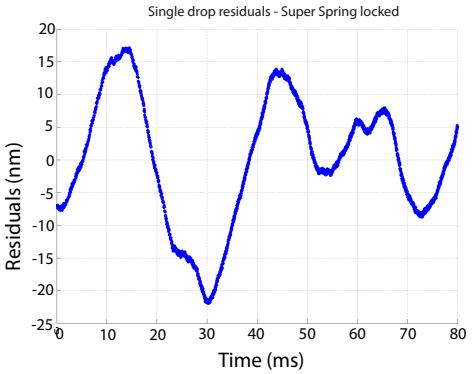


**Figure 5.9:** Single drop residuals of MPG-2 when Super Spring is locked.

from $\approx$ 10 Hz to $\approx$ 0.02 Hz and, hence, filters out the biggest part of the noise. Figure 5.9 shows the residuals of a single drop, obtained with MPG-2 and the

Super Spring locked, while Fig. 5.10(b) shows typical residuals obtained from a single drop with MPG-2, but with the Super Spring working. We can state that the standard deviation in a set of drops could be improved at least by a factor 10 with the Super Spring.

Figures 5.10(a) and 5.10(b) show typical residuals of a single drop. Those residual vibrations cause a bias in the measurement. The error caused by such

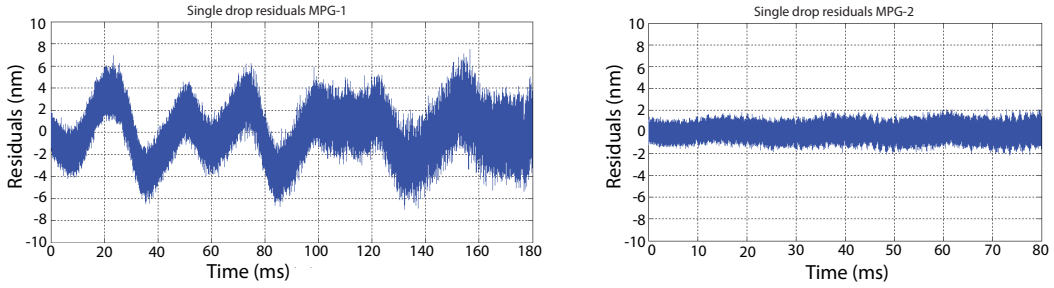


(a) MPG-1 (b) MPG-2

**Figure 5.10:** A closer look at the residuals of a single drop.

residual microseismics can be estimated according to Svetlov (1997) with

$$\Delta g_{seis} = \frac{30\sqrt{2}}{\pi T^3} \frac{A_0}{f_0} \,, \tag{5.17}$$

and the standard uncertainty

$$\sigma_{g_{seis}} = \frac{\Delta g_{seis}}{\sqrt{2}} \,. \tag{5.18}$$

Applying these formulas, where $T$ denotes the total fall time, $A_0$ the amplitude, and $f_0$ the frequency, to the frequencies in our residuals, the uncertainty for MPG-2 ($f_0 = 50$ Hz, $A_0 = 1$ nm, $T = 0.08$ s) amounts to $\sigma_{g_{seis,2}} = 37.3$ $\mu$Gal. Whereas for MPG-1 ($f_0 = 50$ Hz, $A_0 = 6$ nm, $T = 0.2$ s) the uncertainty is $\sigma_{g_{seism,1}} = 14.3$ $\mu$Gal. In the case of MPG-1 we also record higher frequency parts of up to 100 Hz, however the maximum error is computed with the lower frequencies. A simple simulation shows that this is reasonable. For this purpose we synthetically generated drop data with a sine wave added, that approaches the observed one, seen in Fig. 5.11(a) (in the plot only every 1000th sample is

shown). The resultant residuals are shown in Fig. 5.11(b). When computing the acceleration due to gravity, the value obtained is by 28 $\mu$Gal lower than the nominal value, which is well within the predicted uncertainty.

Where our residual microseismics come from, is not clear. We suppose that

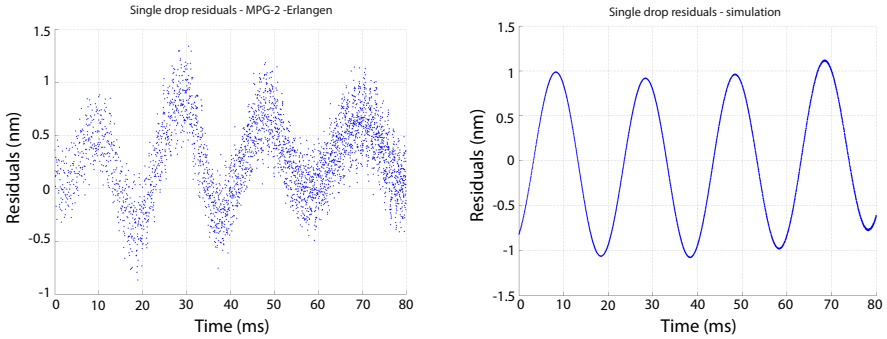


(a) MPG-2 – Real drop.

(b) MPG-2 – Simulated drop.

**Figure 5.11:** A synthetically generated drop compared to a real drop shows a systematic offset in $g$.

they arise from the fact that one part of the object beam path is in the air, and the other part is – inside the dropping chamber – in the vacuum. Hence, a vibration of the dropping chamber causes changes in pathlength. Besides, floor recoil causes also tilts of the interferometer, since it is fixed on top of the Super Spring. As a result the laser beam oscillates around the plumb line. We conclude this since such vibrations are systematic and can be observed in the residuals of each drop. The phase in the observed residual vibrations is almost constant from drop to drop, the frequency, however, varies from measurement site to measurement site.

This systematic effect is big, and Klopping *et al.* (1991) already reported that systematic errors as high as 20 $\mu$Gal were possible and detected for the JILA gravimeters, which were specified to have an accuracy of 3 to 5 $\mu$Gal. However, they presented a mathematical method to reduce the error by subsequently removing frequency parts from the residuals, with which they improved their data to the stated accuracy. Timmen *et al.* (1993) later tried to reproduce the results with the software provided by Klopping, but they concluded that the absolute

accuracy could not be improved, while the precision could (see also Timmen (1994)).

This effect is very complex and cannot be investigated in the framework of this thesis. Hence, we decided to add the theoretical uncertainty to our combined standard uncertainty. To accurately distinguish between vibrations and the free fall, additional information is necessary. A combination of a gradiometer with a gravimeter could be a solution. According to Moritz & Hofmann-Wellenhof (1993) this gives the possibility to separate gravitational from inertial forces.

**Table 5.15:** Uncertainty budget for seismic noise.

| | Correction/$\mu$Gal | Standard uncertainty/$\mu$Gal |
|---|---|---|
| MPG-1 | none | 14.3 |
| MPG-2 | none | 37.3 |

### 5.1.13 Speed of light

The second order polynomial which is fitted to the measured time-distance pairs, does not consider the finite propagation velocity of light. Two possible methods can be chosen among to correct for this error (Kuroda & Mio (1991); in our case the positive $z$-axis is oriented downwards). The first one is an indirect correction: After the least-squares fitting the correction value, obtained from the equation

$$\Delta g_c = -g_0 \left( 3\frac{v_0}{c} + \frac{12}{7}\frac{g_0\, T}{c} \right) \tag{5.19}$$

– which is valid for data equally spaced in distance – is subtracted from the measured value. Subtracted, because the FB is falling towards the BS, which increases the laser frequency. The correct value therefore must be lower. Here $g_0$ is the uncorrected $g$-value, $c$ is the vacuum velocity of light (cf. Appendix A), $v_0$ is the initial velocity of the FB when the first data pair is taken, and $T$ is the total free fall time.

The second way is to introduce a retarded time. The corrected, or retarded, time $t_i'$ has the form

$$t_i' = t_i + \left( \frac{b - z_i(t_i)}{c} \right) , \tag{5.20}$$

where $z_i$ and $t_i$ are the $i$-th distance and time, respectively, as acquired, and $b$ is the initial separation of the FB and the beam splitter. The quotient $b/c$, however, is a negligible constant, as it does not contribute to the acceleration – the entire drop distance is all that counts. This corrects the value for each time-distance data pair. The $g$-value thus obtained is already corrected for the speed of light then. In our gravimeters, the data acquisition is started when $v_0 = 0.32$ m s$^{-1}$. This is valid for both gravimeters. For a drop time of $T = 0.2$ s this gives a correction of -14.1 $\mu$Gal (MPG-1), and for $T = 0.08$ s it amounts to -7.5 $\mu$Gal (MPG-2). The uncertainty arising from this correction mainly comes from the uncertain knowledge of the initial velocity, which is assumed to be 0.01 m s$^{-1}$. A standard uncertainty can be calculated by $\sigma_{g_c} = \frac{\Delta v_0}{v_0} g_c$ and amounts to 0.44 $\mu$Gal for MPG-1, and 0.23 $\mu$Gal for MPG-2. For an uncertainty in total fall time, the error is assumed to be negligible.

**Table 5.16:** Uncertainty budget for speed of light.

| | Correction/$\mu$Gal | Standard uncertainty/$\mu$Gal |
|---|---|---|
| MPG-1 | -14.1 | 0.44 |
| MPG-2 | -7.5 | 0.23 |

### 5.1.14 Reference height

For the absolute gravimeters MPG-1 and MPG-2 the drop lengths are up to 30 cm, and 15 cm, respectively. With a linear gravity gradient $\gamma$ of about 300 $\mu$Gal m$^{-1}$ this signifies a gravity difference between the starting point of the drop and the end point of 90 $\mu$Gal, and 45 $\mu$Gal, respectively. The tracked trajectory, however, is fitted to a second order linear equation, which means the value for $g$ obtained from the fitted curve refers to some point between the starting point and the end point. Several propositions have been made to correct for this *effective height* (Murata, 1978; Nagornyi, 1995; Niebauer, 1989; Zumberge, 1981). We adopt a method proposed by Timmen (2003). Figure 5.12 shows the relation between the instrument height, the reference height, and the effective height. His method requires no previous knowledge of the gravity gradient for the computation; only the initial velocity $v_0$ and the standard gravity value $g = 9.80665$ m s$^{-2}$

(cf. Appendix A) are needed as input parameters. Then the effective height is calculated as

$$h_{eff} = \frac{Av_0^4T + Bv_0^3g_0T^2 + Cv_0^2g_0^2T^3 + Dv_0g_0^3T^4 + Eg_0^4T^5}{Fv_0^3 + Gv_0^2g_0T + Hv_0g_0^2T^2 + Ig_0^3T^3} \,, \tag{5.21}$$

with

$$\begin{aligned} A &= 56.0 & B &= 102.4 & C &= 61.2 \\ D &= 14.0 & E &= 1.0 & F &= 112.0 \\ G &= 168.0 & H &= 67.2 & I &= 5.6 \,. \end{aligned} \tag{5.22}$$

According to this, the reference height $h_{ref}$, which is the instrument height $h_{inst}$ minus the effective height $h_{eff}$ and the initial height $h_0$, therefore is the height to which the measured value should be referred. A reduction of the $g$-value, $g_{eff}$, from the reference height to the rest position is possible, but brings additional errors with it, as a gradiometer is needed to measure the gravity gradient. If the gradient $\gamma$ is known, the reduced value $g_{rest}$ at the instrument height is calculated by

$$g_{rest} = g_{eff} + (h_{eff} + h_0)\,\gamma \,, \tag{5.23}$$

where $\gamma$ is taken as a negative number.

As we use a frequency trigger adjusted to trigger at 1 MHz, the respective velocity is about 0.32 m s$^{-1}$, and the scatter from drop to drop is negligibly small. Timmen (2003) indicates an uncertainty in the effective height determination of less than 0.5 mm. To measure the instrument's height, i.e. the rest position of the FB's apex, with respect to the reference mark on the measurement site ground, a ruler is used. The uncertainty assigned to this measurement is assumed to be within a range of 1 mm. The combined uncertainty, converted into acceleration, is 0.3 $\mu$Gal.

**Table 5.17:** Uncertainty budget for effective height.

| | Correction/$\mu$Gal | Standard uncertainty/$\mu$Gal |
|---|---|---|
| MPG-1 | none | 0.3 |
| MPG-2 | none | 0.3 |

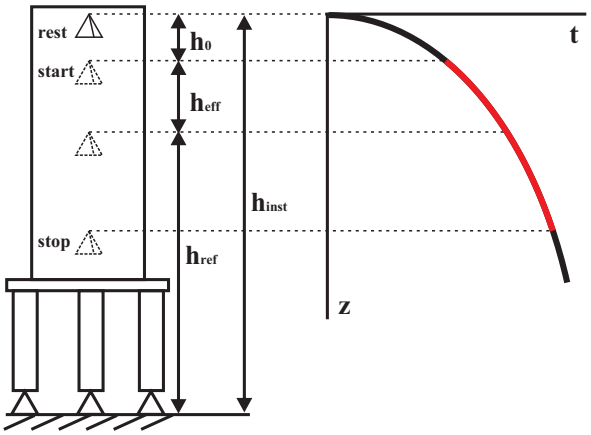


**Figure 5.12:** The reference height is obtained by subtracting the initial height of the trajectory $h_0$ and the effective height $h_{eff}$ from the instrument height $h_{inst}$.

### 5.1.15 Non-linearity of electronics

Each amplifier introduces a phase shift to the measured signal. If this phase shift is constant or linear over the entire frequency range, there is no bias on the measured $g$ value. However, in the case the phase shift is a function of frequency, and non-linear, the phase shift simulates an additional acceleration that causes a systematic error. We investigated this problem by measuring the phase shift produced by the amplifier HCA-200M-20K-C (for specifications see Tab. 5.18), from FEMTO Messtechnik GmbH with the network analyser E5061A from Agilent. A direct measurement with the network analyser shows a very

**Table 5.18:** Specifications of high-speed photoreceiver with SI PIN Photodiode.

| | | |
|---|---|---|
| Gain | Transimpedance | $2.0 \times 10^4$ V $A^{-1}$ (@ 50 Ω load) |
| Frequency response | Lower Cut-Off Frequency | DC |
| | Upper Cut-Off Frequency | 200 MHz (±10%) |
| | Rise/Fall Time (10%-90%) | 1.8 ns |

straight line (Fig. 5.13(a)). The non-linearity only becomes visible after a linear term is subtracted (Fig. 5.13(b)). The data obtained can then be converted into distance (Fig. 5.13(c)), from which the acceleration can be calculated. It

turned out that of all ranges, just in the important frequency range (DC-7 MHz) the amplifier shows non-linearities. The error is calculated considering the fringe signal $U(t) = A\sin(\frac{2\pi z(t)}{\lambda/2})$, where $A$ denotes the maximum amplitude, $\lambda$ is the laser wavelength and $z(t)$ is the height fallen by the FB. For an unperturbed free fall, the velocity, and hence the signal frequency, changes linearly and can be correlated to the drop time. The phase shift introduced by the amplifier, makes a fictitious change in height. The error can be calculated by fitting the second order polynomial, i.e. the free fall model, to the phase response, converted into displacement. Fig. 5.13 (bottom graph) shows the residuals after applying the least squares fit. In our case, this error amounts to $\Delta g = (-4.71 \pm 0.02)$ $\mu$Gal – for correction 4.71 $\mu$Gal has to be added to the measured value. This is systematic and valid for a drop length of 200 ms, as in the case of MPG1. In the case of MPG2, where the starting point is the same, namely 1 MHz, but the total drop time is just 80 ms, the error is $\Delta g = (-1.9 \pm 0.6)$ $\mu$Gal. The uncertainty in the non-linearity correction results from the uncertainty in the initial frequency, i.e. the accuracy of the frequency trigger, where a standard error of 32 kHz is assumed.

**Table 5.19:** Uncertainty budget for non-linearity of amplifier.

| | Correction/$\mu$Gal | Standard uncertainty/$\mu$Gal |
|---|---|---|
| MPG-1 | -4.71 | 0.02 |
| MPG-2 | -1.9 | 0.6 |

## 5.2 Uncertainty budget due to environmental effects

### 5.2.1 Solid Earth tides

When measuring the Earth's gravity field, the tidal influences of other astronomical objects have to be corrected for. The theory of tidal parameter calculation was sketched in Chapter 1. The body tides due to the Sun and Moon are the biggest influences on the measurement, with a range of $\pm 150$ $\mu$Gal. The software *TSoft* (TSoft, 2008; van Camp & Vauterin, 2005) is used to correct the measured

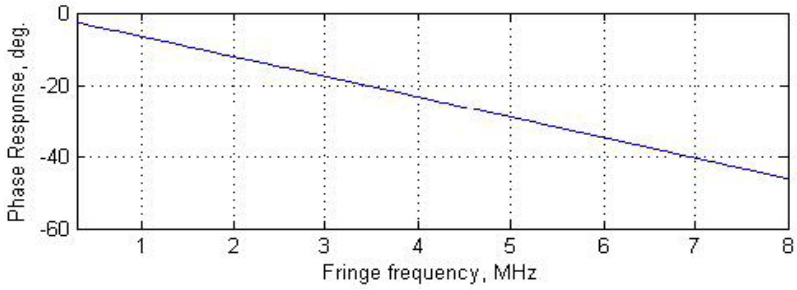


(a) Direct measurement of the phase response.

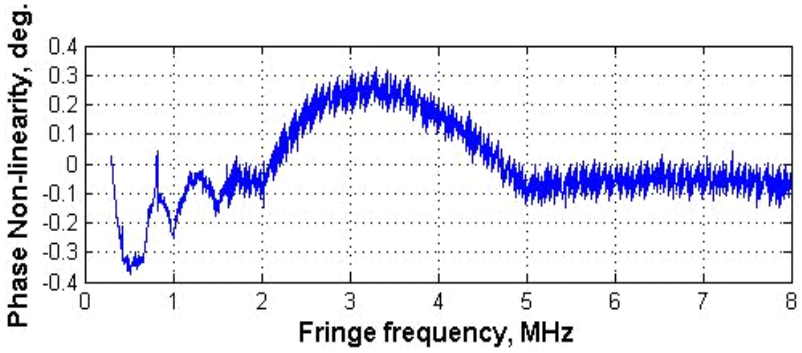


(b) Phase response when linear term is subtracted.

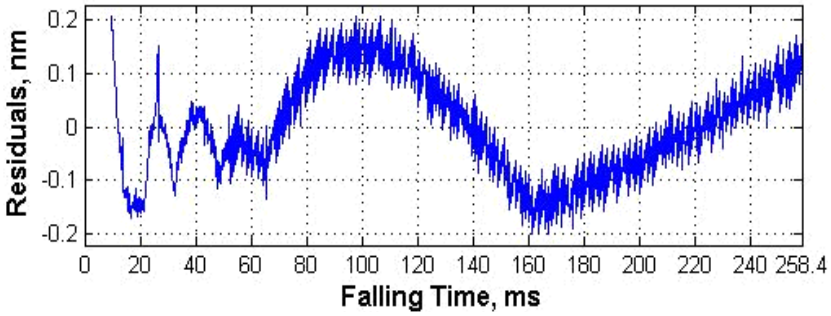


(c) Residuals after least squares fit. nm.

**Figure 5.13:** Results of the phase response measurement of the amplifier.

data for the body tides. The quoted uncertainty for the tidal correction is 0.1 $\mu$Gal.

**Table 5.20:** Uncertainty budget for solid Earth tides.

| | Correction/$\mu$Gal | Standard uncertainty/$\mu$Gal |
|---|---|---|
| MPG-1 | $\pm$150 | 0.1 |
| MPG-2 | $\pm$150 | 0.1 |

### 5.2.2 Ocean loading

When the sea is drawn by the Sun's and Moon's attractions, the Earth is deformed. The huge load at the coastal regions pulls down the solid ground. For this reason, the vertical displacement due to ocean loading can reach up to 20 cm (in Cornwall, (cf. van Camp, 2005)), which equals approximately 30 $\mu$Gal. Inland, the contribution due to ocean loading is much smaller. For the site Erlangen the ocean loading effect is no more than 3 $\mu$Gal, with an error estimated to about 10 %, which contributes with 0.3 $\mu$Gal to our uncertainty budget. A better estimate of this effect needs better models to describe the ocean tides, which are the main error source, and also a better knowledge of the rheology of the Earth's interior (van Camp, 2005).

**Table 5.21:** Uncertainty budget for ocean loading.

| | Correction/$\mu$Gal | Standard uncertainty/$\mu$Gal |
|---|---|---|
| MPG-1 | $\pm$3 | 0.3 |
| MPG-2 | $\pm$3 | 0.3 |

### 5.2.3 Polar motion

The Earth's axis of rotation is not fixed within the the Earth, but is displaced at any moment by a few meters from the axis of maximum inertia. Although this can be measured by observing the zenith distance of the celestial pole of rotation, it cannot be predicted accurately. Chandler observed in 1891 that the amplitude of the quasi-circular motion changes in a range of 0.05 to 0.25 arc seconds within a period of 6 years (Seidelmann, 1992). In his honour, this polar

motion is also called *Chandler wobble*. It corresponds to the Euler nutation in an elastic Earth. Variations of up to 13 $\mu$Gal in surface gravity are possible (Wahr, 1985). The formula specified in the IAGBN Absolute Observations Data Processing Standards (1992) (extracted from Vauterin & van Camp (2007)) for polar motion correction (in nm s$^{-2}$) is

$$\Delta g_{pm} = -1.164\,\omega^2 a \sin\phi\cos\phi(x_p\cos\lambda - y_p\sin\lambda)\ , \tag{5.24}$$

where $\omega$ is the angular velocity of the Earth (in radians s$^{-1}$), $a = 6378136.6(1)$ m is the semi major axis of the reference ellipsoid (number from McCarthy & Petit (2003), IERS Numerical Standards), $\phi$ is the geodetic latitude (in radians), and $\lambda$ the geodetic longitude (in radians). $x_p$ and $y_p$ are the pole coordinates (in radians) and are available on `ftp://hpiers.obspm.fr/iers/eop/eopc04/`. The daily predicted values can also be found in the IERS Bulletin – A, and the final daily polar coordinates are published in the IERS Bulletin – B. IERS's site (`http://hpiers.obspm.fr/eop-pc/`) estimates that the present relative uncertainty as to the Earth's orientation parameters is about $10^{-4}$, hence we consider the uncertainty to be negligible.

**Table 5.22:** Uncertainty budget for polar motion.

| | Correction/$\mu$Gal | Standard uncertainty/$\mu$Gal |
|---|---|---|
| MPG-1 | $\pm 13$ | $10^{-4}$ |
| MPG-2 | $\pm 13$ | $10^{-4}$ |

### 5.2.4 Pressure effects

A change in local pressure also changes the gravity value, as a higher pressure signifies a higher mass of air above the measurement apparatus. This means an attraction upwards, and hence lowers the nominal value. A correction can be applied as recommended in Boedecker & Richter, Bu. (1984): The nominal pressure at a measurement height $h_m$ (in meters) is defined by the equation

$$p_n = 1013.25\left(1 - 0.0065\,\frac{h_m}{288.15\,\mathrm{m}}\right)\ hPa\ . \tag{5.25}$$

With the barometric factor defined as $f_B = 0.3\ \mu\text{Gal hPa}^{-1}$ the correction to the observed value $g_o$ amounts to

$$\Delta p_{corr} = f_B(p_o - p_n)\ . \tag{5.26}$$

To collect weather data we use the Heavy Weather station 2300. It has a pressure resolution of 0.1 hPa. Assuming the standard error of the pressure gage to be 1 hPa, the relative standard deviation amounts to about $1 \times 10^{-3}$. This gives an uncertainty contribution to our uncertainty budget of 0.3 $\mu$Gal. This can easily be reduced by the pressure gauge frequently calibrating. For the comparison at Bad Homburg in February 2008, the pressure values provided by the superconducting gravimeters, were taken. For this comparison, the uncertainty due to environmental pressure is negligible.

**Table 5.23:** Uncertainty budget for environmental pressure.

| | Correction/$\mu$Gal | Standard uncertainty/$\mu$Gal |
|---|---|---|
| MPG-1 | $\pm 3$ | 0.3 |
| MPG-2 | $\pm 3$ | 0.3 |

### 5.2.5 Coriolis force

A vertical acceleration – the Coriolis acceleration – on the FB can be generated, if during the start of the drop the FB has a horizontal momentum in the east-west direction, according to the following equation:

$$a_{Cor} = 2\,\Omega_N v_{EW} \sin\Theta = \frac{14.6\ \mu\text{Gal}}{\text{mm s}^{-1}}\, v_{EW} \sin\Theta\ . \tag{5.27}$$

Here $\Omega_N$ is the nominal angular velocity of the Earth (cf. Appendix A), $v_{EW}$ is the velocity component of the FB in the east-west direction, and $\Theta$ is the latitude of the site of measurement. To estimate this effect we assume that our rail which guides the elevator is not well aligned along $\mathbf{g}$. This can easily observed by the movement of the laser spot, when moving up and down the elevator by means of the motor. The rail is usually aligned so that the beam spot does not move more than 0.5 mm. The range the elevator can be moved up and down is about 250 mm. Hence the inclination with respect to the plumb line is about

**Table 5.24:** Uncertainty budget for Coriolis force.

| | Correction/$\mu$Gal | Standard uncertainty/$\mu$Gal |
|---|---|---|
| MPG-1 | none | 0.5 |
| MPG-2 | none | 0.5 |

$2 \times 10^{-3}$ rad. The acceleration of the elevator is about 11 m s$^{-2}$. Overestimating a dragging contact time between the vee-grooves and the falling body to be 10 ms gives a velocity along the rail of about 110 mm s$^{-1}$ and, hence, as a horizontal component $v_{EW} = 0.22$ mm s$^{-1}$. This would give an Coriolis acceleration (for $\Theta \approx 50°$) of approximately 0.5 $\mu$Gal. For our uncertainty budget we assume 0.5 $\mu$Gal as an upper limit.

## 5.3 Combined standard uncertainty

By combining all of the error sources we can give the total corrections and uncertainty for the gravimeters MPG-1 and MPG-2.

### 5.3.1 MPG-1

**Table 5.25:** Corrections and standard uncertainty for MPG-1.

| | Correction/$\mu$Gal | Standard uncertainty/$\mu$Gal |
|---|---|---|
| Air drag | | $0.3 \times 10^{-2}$ |
| Outgassing | | $4.2 \times 10^{-5}$ |
| Buoyancy | | negligible |
| Magnetic attraction | | negligible |
| Eddy currents | | 0.1 |
| Electrostatic field | | negligible |
| Instrumental masses | -1.8 | 0.5 |
| Beam verticality | | 6 |
| Laser stability | | 3.64 |
| Clock stability | | 0.6 |
| FB rotation | | 0.7 |
| Radiation pressure | | $2.8 \times 10^{-3}$ |
| Beam divergence | +22 | 1.8 |
| Temperature gradient | | $1.5{\times}10^{-3}$ |
| Tilt of optical table | up to $\pm$40 | 4 |
| Floor recoil & seismic vibrations | | 14.3 |
| Speed of light | -14.1 | 0.44 |
| Reference height | | 0.3 |
| Non-linearity of electronics | +4.71 | 0.02 |
| Solid Earth tides | up to $\pm$150 | 0.1 |
| Ocean loading | up to $\pm$3 | 0.3 |
| Polar motion | up to $\pm$13 | $1{\times}10^{-4}$ |
| Environmental pressure | up to $\pm$3 | 0.3 |
| Coriolis force | | 0.5 |
| Statistical uncertainty (1 month) | | 0.6 (Erlangen) |
| Total correction | +10.81 | |
| Combined standard uncertainty | | 16.58 |

### 5.3.2 MPG-2

**Table 5.26:** Corrections and standard uncertainty for MPG-2.

| | Correction/$\mu$Gal | Standard uncertainty/$\mu$Gal |
|---|---|---|
| Air drag | +4.0 | 0.8 |
| Outgassing | | $3 \times 10^{-3}$ |
| Buoyancy | | negligible |
| Magnetic attraction | | negligible |
| Eddy currents | | 0.1 |
| Electrostatic field | | negligible |
| Instrumental masses | | 0.5 |
| Beam verticality | | 6 |
| Laser stability | | 3.64 |
| Clock stability | | 0.6 |
| FB rotation | | 0.7 |
| Radiation pressure | | $2.8 \times 10^{-3}$ |
| Beam divergence | +22 | 1.8 |
| Temperature gradient | | $1.5 \times 10^{-3}$ |
| Floor recoil & seismic vibrations | | 37.3 |
| Speed of light | -7.5 | 0.23 |
| Reference height | | 0.3 |
| Non-linearity of electronics | +1.9 | 0.6 |
| Solid Earth tides | up to $\pm$150 | 0.1 |
| Ocean loading | up to $\pm$3 | 0.3 |
| Polar motion | up to $\pm$13 | $1 \times 10^{-4}$ |
| Environmental pressure | up to $\pm$3 | 0.3 |
| Coriolis force | | 0.5 |
| Statistical uncertainty (24 hours) | | 5.0 (Bad Homburg) (1.6 (Erlangen)) |
| Total correction | +20.4 | |
| Combined standard uncertainty | | 38.36 (Bad Homburg) (38.07 (Erlangen)) |

## 5.4 Discussion of the uncertainty budgets

The uncertainty budgets listed above result from a first careful study of the newly designed absolute free fall gravimeters, and do not claim to be complete. Both gravimeters were developed together in less than three years. The main focus

was developing a new method to balance the falling body and to design new mechanics for a portable system. Both tasks were accomplished to our satisfaction. The resolutions of MPG-1 and MPG-2 are 0.6 $\mu$Gal and 1.6 $\mu$Gal, respectively. The specified combined standard uncertainties (accuracies) of 16.58 $\mu$Gal and 38.07 $\mu$Gal for MPG-1 and MPG-2, respectively, can be regarded as overestimations. Looking closer at the uncertainty budget we can clearly distinguish the main error sources, such as floor recoil and seismic vibrations, beam verticality and laser stability. Without the uncertainty due to floor recoil and seismic vibrations, the combined standard uncertainty would decrease to 7.62 $\mu$Gal for MPG-2. This were an excellent result. We believe that residual vibrations mainly come as a result of path length differences due to vibrations of the dropping chamber. This changes the relation between the beam propagating in vacuum and that in air. A full treatment of this effect is very complex and is outside the scope of this thesis. A very careful estimation has been done therefore. Except for the vibration problems we expect to be able to reduce or eliminate these error sources soon. A new laser system has already been constructed and tested to reduce laser instability. Beam verticality uncertainties can be reduced by a new alignment method, e.g. employing an autocollimator.

# Chapter 6

# Summary and outlook

During the last three years two new absolute gravimeter systems have been designed, constructed and tested. The first one (MPG-1) was aimed to provide stationary, long-term, highly accurate gravity measurements. Several long-term measurements were conducted over months, with measurement standard errors of down to 0.6 $\mu$Gal month$^{-1}$. Due to its long drop duration of up to 250 ms, the main uncertainty source in the uncertainty budget, namely residual vibrations, can be reduced in comparison to the portable gravimeter MPG-2. This high accuracy allows the stationary gravimeter MPG-1 the status of a reference apparatus.

The second gravimeter (MPG-2) was developed to provide a portable apparatus, which enables field measurements and intercomparisons with other instruments. It was brought to an european comparison of absolute gravimeters and showed a good agreement with most other European gravimeters. With its compact design and measurement standard errors of about 5 $\mu$Gal (12 h)$^{-1}$ it represents a competitive device in the field of absolute gravity measurements. An estimated combined standard uncertainty for MPG-2 of 38.5 $\mu$Gal comes mainly from disturbing vibrations. For a better understanding of the origin of these vibrations, further investigations have to be conducted. Once this source of error can be eliminated, we believe that the uncertainty can be reduced to the $\mu$Gal-scale.

For now, the target tasks are achieved. A highly accurate stationary reference absolute gravimeter and a fully automated, portable absolute gravimeter were

built, which can find application in many fields of physics, geophysics, and the military, just to name some. The expanded uncertainty of 77 $\mu$Gal (coverage factor $k = 2$), is good enough for the measurement of the Boltzmann constant and the redefinition of the Kelvin, which require a relative uncertainty of $1 \times 10^{-7}$.

The novel spring mechanics in the portable gravimeter promises to be a good way of decreasing disturbing vibrations. The new method developed to balance falling bodies to high precision gives hope of further increasing the accuracy of free fall absolute gravimeters, as during the last years it proved to be the biggest error contribution. A new laser system with a high stability and accuracy, and which needs no modulation on the frequency, is finished. Together with a new inertial reference mirror system that is under development, the whole gravimeter will be a completely own development, which will help to detect systematic errors, and hence, give more insight to the accuracy of modern free fall gravimeters.

Gravity measurements are becoming increasingly important in many fields beyond physics. Some instances are the use of gravity data to determine mineral deposits (Bell & Hansen, 1998; Pawlowski, 1998), or applications in archaeology, i.e. to reveal local gravity changes associated with remains of ancient buildings within the cultural layer (Slepak, 1997), as well as in geophysics to observe land uplifts (Müller *et al.*, 2007). Metrology and fundamental physics are highly interested in further improvements of gravimeters, because of the devices' high potential to measure the Planck constant, the Boltzmann constant, the Newtonian constant or to redefine the Kelvin and the kilogram (cf. Sec. 1.3).

Regarding the influence of radiation pressure of $2.8 \times 10^{-3}$ $\mu$Gal (cf. Sec. 5.1.9) in our system, a laser with higher power and a lighter falling body could detect this effect. As an application, Newton's second law could be verified by comparing the mechanical force with the light force. Measurements in this field were already done by Gundlach *et al.* (2007), but using a torsion pendulum, or by Abramovici & Vager (1986), employing the prototype of their active cavity gravitational-radiation detector.

In conclusion, it can be said that the two free fall absolute gravimeters built in the framework of this thesis under the supervision of Prof. L.J. Wang, and Dr. S. Svitlov present excellent devices to continue research in fundamental physics. The groundwork is laid for prospective projects.

# Appendix A

# List of numbers and physical constants

In the following table some of the important numbers and constants used in the thesis are compiled. Physical constants are taken from NIST (2008), or IERS Constants (2008), and the material density numbers from Fischer *et al.* (2002).

Remark on the use of the unit $\mu$Gal:
The SI unit of acceleration is $\mathrm{m\,s^{-2}}$, but it is impractical for use in geophysics, as the effects of interest are in the $\mathrm{cm\,s^{-2}}$ range and lower. In the c.g.s. system however, the unit of acceleration is $\mathrm{cm\,s^{-2}}$ which, in honour of Galileo Galilei, is called "Gal" (1 $\mu$Gal is 10 $\mathrm{nm\,s^{-2}}$). It is widely used in geophysics as well as in geodesy.

The unit $E$ (Eötvös) for the gravity gradient is also not compatible with the SI, but frequently used for convenience. The conversion is 1 E = $10^{-9}$ $\mathrm{s^{-2}}$ = 0.1 $\mu$Gal $\mathrm{m^{-1}}$.

Coordinates for the site *Erlangen*:
49.34°N, 11.00°E, 287.0 m elevation

# A. LIST OF NUMBERS AND PHYSICAL CONSTANTS

**Table A.1:** Physical Constants and numbers.

| Name of constant | Value | Relative Standard Uncertainty | Unit (SI) |
|---|---|---|---|
| Newtonian constant of gravitation $G$ | $6.674\,28 \times 10^{-11}$ | $1{\times}10^{-4}$ | $m^3\ kg^{-1}\ s^{-2}$ |
| Speed of light in vacuum $c$ | 299 792 458 | (exact) | $m\ s^{-1}$ |
| Standard acceleration of gravity $g$ | 9.806 65 | (exact) | $m\ s^{-2}$ |
| Boltzmann constant $k_B$ | $1.380\,650\,4 \times 10^{-23}$ | $1.7 \times 10^{-6}$ | $J\ K^{-1}$ |
| Avogadro constant $N_A$ | $6.022\,141\,79 \times 10^{23}$ | $5 \times 10^{-8}$ | $mol^{-1}$ |
| Planck constant $h$ | $6.626\,068\,96 \times 10^{-34}$ | $5{\times}10^{-8}$ | J s |
| Molar gas constant $R$ | 8.314 472 | $1.7{\times}10^{-6}$ | $J\ mol^{-1}\ K^{-1}$ |
| Earth's equatorial radius $a$ | 6 378 136.6 | $1.5{\times}10^{-8}$ | m |
| Earth's flattening $f$ | 1/298.256 42 | $3 \times 10^{-8}$ | |
| Geocentric constant of gravitation $GM$ | $3.986\,004\,418 \times 10^{14}$ | $2 \times 10^{-9}$ | $m^3\ s^{-2}$ |
| Heliocentric constant of gravitation $GS$ | $1.327\,124\,420\,76 \times 10^{20}$ | $4 \times 10^{-10}$ | $m^3\ s^{-2}$ |
| Nominal angular velocity of the Earth $\Omega_N$ | $7.292\,115\,146\,706\,4$ $\times 10^{-5}$ | (exact) | $rad\ s^{-1}$ |
| Density of titanium $\rho_{Ti}$ | $4.5 \times 10^3$ | | $kg\ m^{-3}$ |
| Density of aluminium $\rho_{Al}$ | $2.7 \times 10^3$ | | $kg\ m^{-3}$ |
| Density of stainless steel $\rho_{St}$ | $7.9 \times 10^3$ | | $kg\ m^{-3}$ |

# Appendix B

# Results of long term measurements

## B.1 Measurements with MPG-1

The following presents some graphs of long-term measurements conducted with the stationary absolute gravimeter MPG-1. The gaps seen in the figures are mainly due to software glitches, which caused the measurement to stop. The FB was also observed to jump out of the support ring. This error was tracked to a lack of grease on the rails and did not reoccur once the rail and ball bearings had been maintenanced.

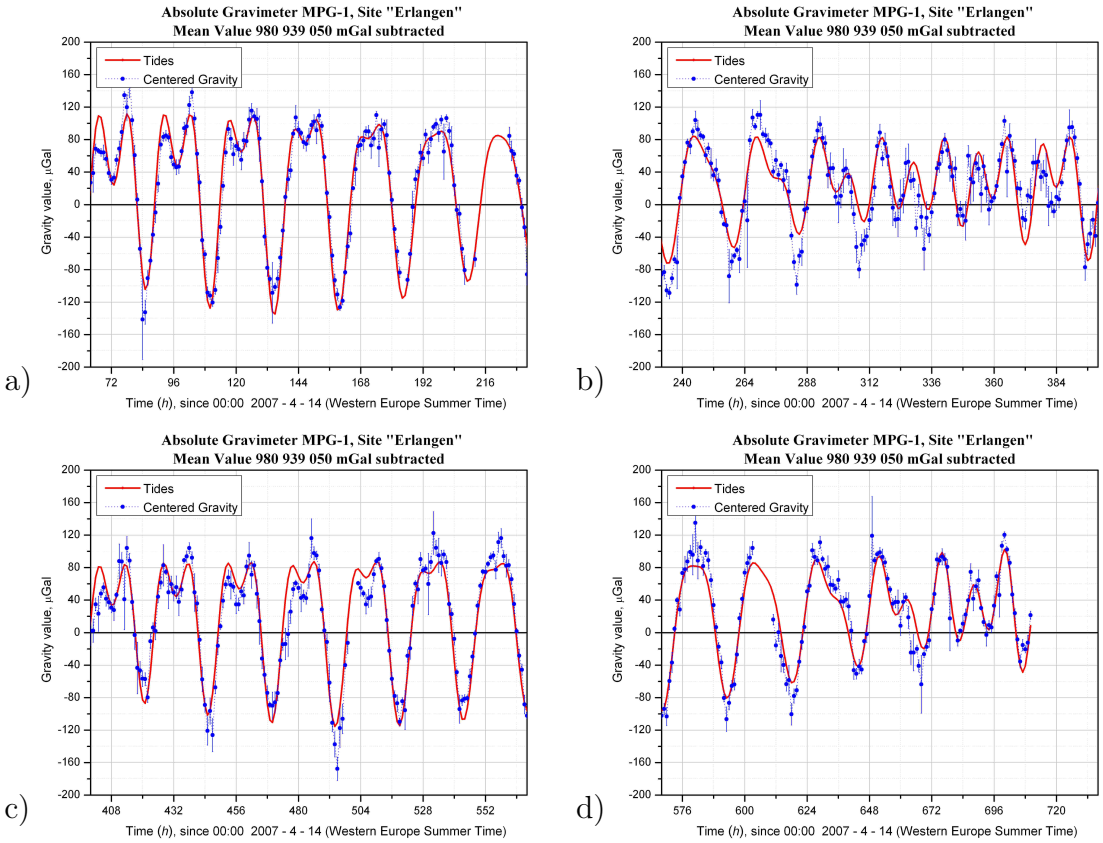


**Figure B.1:** Results of the long term measurement #4 with MPG-1.

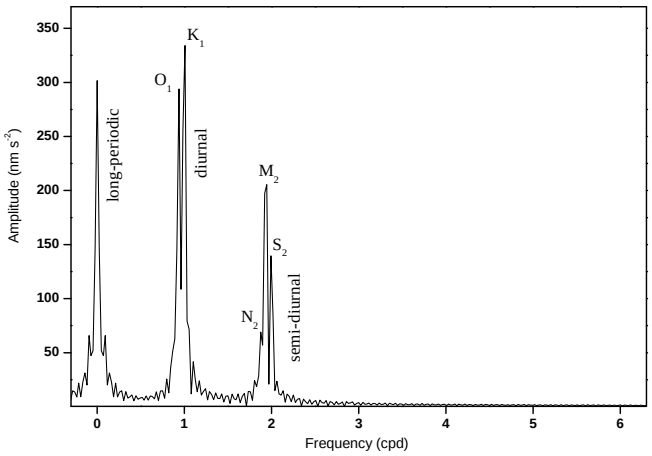


**Figure B.2:** Amplitude spectrum of one month of measured gravity with MPG- 1 (LT#4).

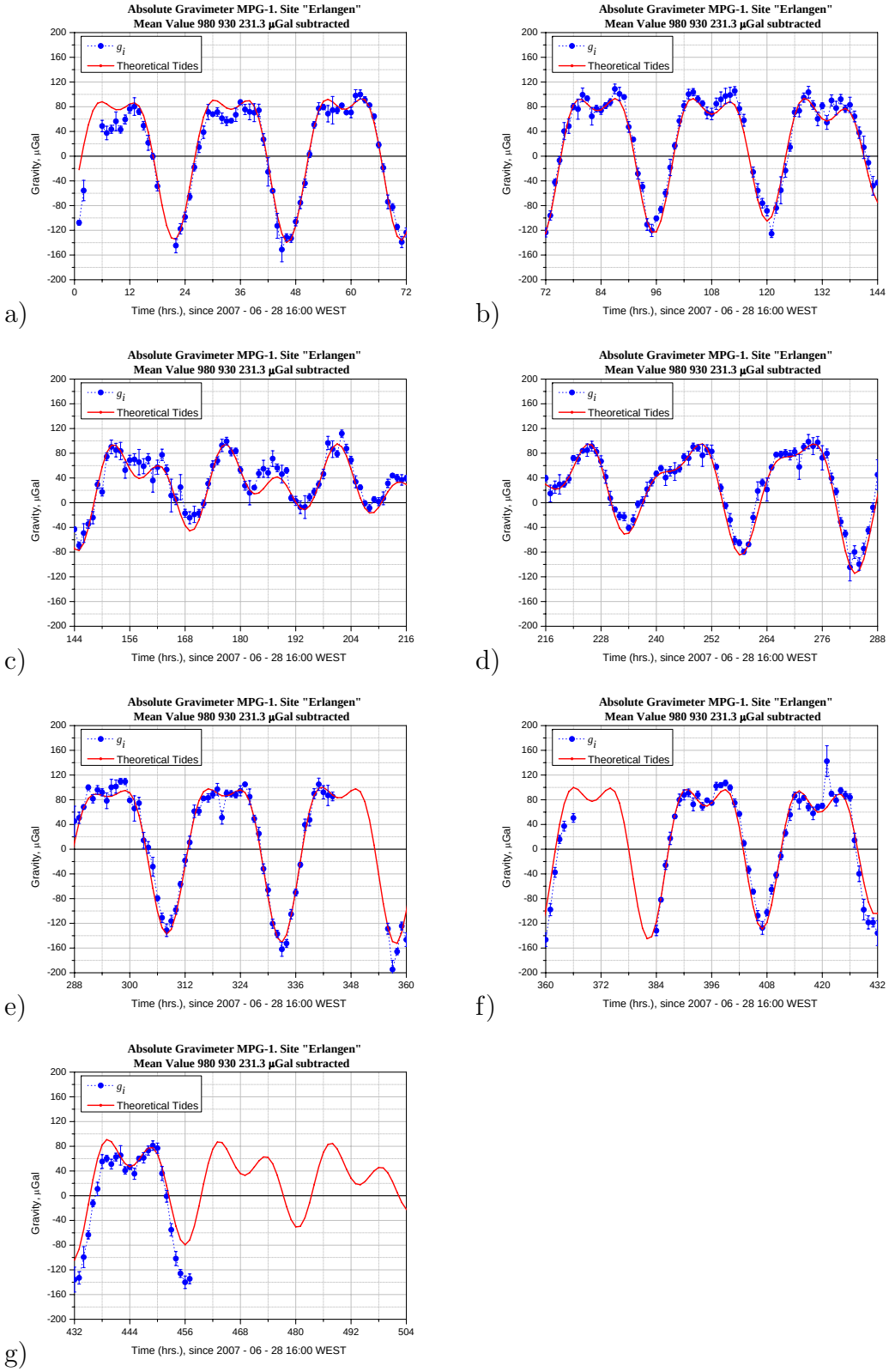


**Figure B.3:** Results of the long term measurement #5 with MPG-1.

## B.2 Measurements with MPG-2

The following figures show the measurements realized during ECAG 2007 at the observation sites A1 and B2:

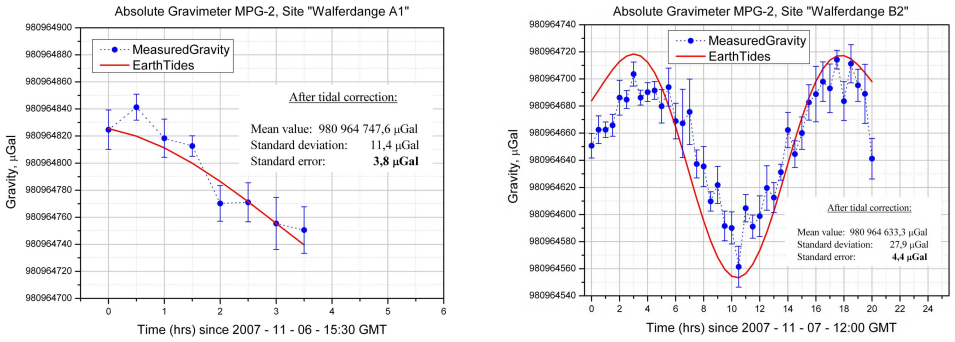


(a) Observation site A1 (b) Observation site B2

**Figure B.4:** Measurements at ECAG 2007 in Walferdange/ Luxembourg with MPG-2.

Data from the comparison at Bad Homburg:

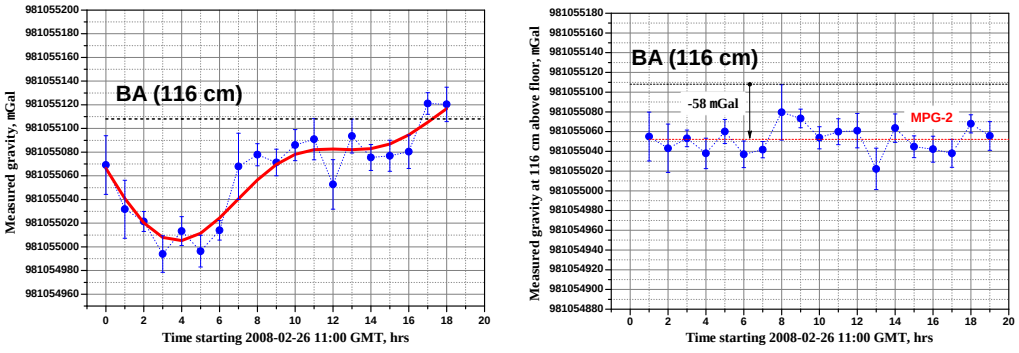


(a) Gravity values. (b) Residuals.

**Figure B.5:** Measurements at Bad Homburg – pillar BA.

# References


Abramovici, A. & Vager, Z. (1986). Test of newton's second law at small accelerations. *Phys. Rev. D*, **34**, 3240–3241. 122

AccuBeat Ltd. (2008). http://www.accubeat.com. 97

Adelberger, E.G., Stubbs, C.W., Heckel, B.R., Su, Y., Swanson, H.E., Smith, G., Gundlach, J.H. & Rogers, W.F. (1990). Testing the equivalence principle in the field of the Earth: Particle physics at masses below 1 $\mu$eV? *Phys. Rev. D*, **42**, 3267–3292. 5

Agaletzkij, P.N., Egorov, K.N. & Martsinjak, A.I. (1959). Results of absolute determinations of the acceleration due to gravity by three independent methods in the point of VNIIM (Leningrad). *Bull. Géod.*, **51**, 82–90. 13

Agilent (2007). http://www.home.agilent.com/. 110

Baudon, J., Mathevet, R. & Robert, J. (1999). Atomic interferometry. *J. Phys. B: At. Mol. Opt. Phys.*, **32**, R173–R195. 14, 17

Bell, R.E. & Hansen, R.O. (1998). The rise and fall of early oil field technology: The torsion balance gradiometer. *The Leading Edge*, 81–83. 122

Boedecker, G. & Richter, Bu. (1984). *Das Schweregrundnetz 1976 der Bundesrepublik Deutschland (DSGN 76) - Teil II: Netzentwurf, instrumentelle Vorarbeiten und Datenaufbereitung*. No. Heft Nr. 281 in Reihe B, Deutsche Geodätische Kommission, angewandte Geodäsie. 114

## REFERENCES


Bondarenko, V.P., Lokshin, Y.V., Svetlov, S.M., Sidorenko, V.S., Solojov, V.S. & Shurubkin, V.D. (1997). SSIA "Metrology" absolute gravimeters. In J. Segawa, H. Fujimoto & S. Okubo, eds., *Gravity, Geoid and Marine Geodesy*, 117, 20–23. 13

Braginsky, V. & Panov, V. (1971). Verification of equivalency of inertial and gravitational masses. *Zh. Eksp. Teor. Fiz.*, **61**, 873–879. 5

Coherent (2008). http://www.coherent.com/index.cfm. 99

Cook, A.H. (1965). The absolute determination of the acceleration due to gravity. *Metrologia*, **1**, 84–114. 6, 13

D'Agostino, G. (2005). *Development And Metrological Characterization of a New Transportable Absolute Gravimeter*. Ph.D. thesis, Scuola di Dottorato. 15, 16, 17, 87

D'Agostino, G., Desogus, S., Germak, A., Origlia, C. & Barbato, G. (2003). The assessment of the measurement error due to a non-vertical laser beam path in absolute gravimeters. In O. Francis & T. van Dam, eds., *Cahier du Centre Européen de Géodynamique et de Séismologie*, vol. 26. 95

Dehlinger, P. (1978). *Marine Gravity*, vol. 22 of *Elsevier Oceanography Series*. Elsevier Scientific Publishing Company Amsterdam. 3, 7, 9, 10, 11, 13

Doodson, A. (1921). Harmonic development of the tide-generating potential. In *Proceedings of the Royal Society of London A*, vol. 100, 305329. 10

Eichenberger, A., Jeckelmann, B. & Richard, P. (2003). Tracing plancks constant to the kilogram by electromechanical methods. *Metrologia*, **40**, 356–365. 21

ETERNA (2008). http://www.eas.slu.edu/GGP/ETERNA/. 11

Fellmuth, B., Gaiser, C. & Fischer, J. (2006). Determination of the boltzmann constant—status and prospects. *Measurement Science and Technology*, **17**, R145–R159. 19

FEMTO Messtechnik GmbH (2008). http://www.femto.de/. 110

Fischer, J., Gerasimov, S., Hill, K., Machin, G., Moldover, M., Pitre, L., Steur, P., Stock, M., Tamura, O., Ugur, H., White, D., Yang, I. & Zhang, J. (2007). Preparative steps towards the new definition of the kelvin in terms of the boltzmann constant. *International Journal of Thermophysics*, **28**, 1753 – 1765. 18

Fischer, U., Heinzler, M., Kilgus, R., Näher, F., Oesterle, S., Paetzold, H., Röhrer, W., Stephan, A. & Winkow, R. (2002). *Tabellenbuch Metall*. Europa-Lehrmittel, 42nd edn. 125

Fixler, J.B., Foster, G.T., McGuirk, J.M. & Kasevich, M.A. (2007). Atom interferometer measurement of the newtonian constant of gravity. *Science*, **315**, 74–77. 22

Gage Applied (2008). http://www.gage-applied.com/. 27

Germak, A., Desogus, S. & Origlia, C. (2002). Interferometer for the IMGC rise-and-fall absolute gravimeter. *Metrologia*, **39**, 471–475. 51, 54

Gray, J., Thomas, P. & Zhu, X. (2001). Laser pointing stability measured by an oblique-incidence optical transmittance difference technique. *Review of Scientific Instruments*, **72**, 3714–3717. 103

Gundlach, J.H., Schlamminger, S., Spitzer, C.D., Choi, K.Y., Woodahl, B.A., Coy, J.J. & Fischbach, E. (2007). Laboratory Test of Newton's Second Law for Small Accelerations. *Physical Review Letters*, **98**, 150801–+. 122

Hanada, H. (1988). Coinciding the optical center with the center of gravity in a corner cube prism: a method. *Appl.Opt.*, **27**, 3530–3533. 51, 54, 85

Hanada, H., Tsubokawa, T. & Tsuruta, S. (1996). Possible large systematic error source in absolute gravimetry. *Metrologia*, **33**, 155–160. 51, 85

Heavy Weather (2007). http://www.heavyweather.info/. 115

Hexagon Metrology (2006). http://www.hexagonmetrology.net/. 56

Hofmann-Wellenhof, B. & Moritz, H. (2005). *Physical Geodesy*. Springer Wien New York. 3, 4

IERS Constants (2008). http://hpiers.obspm.fr/eop-pc/. 125

ISO (1995). Guide to the expression of uncertainty in measurement. ISBN 92-67-10188-9. 63, 80

Jungnickel, C. & McCormmach, R. (1996). *Cavendish (Memoirs of the American Philosophical Society)*. American Physical Society. 22

Kasevich, M. & Chu, S. (1991). Atomic interferometry using stimulated raman transitions. *Phys. Rev. Lett.*, **67**, 181–184. 14, 17

Kibble, B.P. (1976). A measurement of the gyromagnetic ratio of the proton by the strong field method. In J.H. Sanders & A.H. Wapstra, eds., *Atomic Masses and Fundamental Constants*, vol. 5, 542–551, Plenum, New York. 20

Kibble, B.P., Robinson, I.A. & Belliss, J.H. (1990). A realization of the SI Watt by the NPL moving-coil balance. *Metrologia*, **27**, 173–192. 20

Kleppner, D. (2008). PHYSICS: A Milestone in Time Keeping. *Science*, **319**, 1768–1769. 22

Klopping, F.J., Peter, G., Robertson, D.S., Berstis, K.A., Moose, R.E. & Carter, W.E. (1991). Improvements in absolute gravity observations. *Journal of Geophysical Research*, **96**, 8295–8303. 106

Kühnen, F. & Furtwängler, P. (1906). Bestimmung der absoluten Grösze der Schwerkraft zu Potsdam: mit Reversionspendeln. *Veröff. Königl. Preuss. Geod. Inst.*, **27**, 390. 13

Kuroda, K. & Mio, N. (1991). Correction to interferometeric measurements of absolute gravity arising from the finite speed of light. *Metrologia*, **28**, 75–78. 107

Lambeck, K. (1980). *The Earth's Variable Rotation*. Cambridge Monographs on Mechanics and Applied Mathematics, Cambridge University Press. 11

Longman, I.M. (1959). Formulas for computing the tidal accelerations due to the moon and the sun. *J. Geophys. Res.*, **64**, 23512355. 11

Lowrie, W. (1997). *Fundamentals of Geophysics*. Cambridge University Press. 3, 4

Lubcon (2008). http://www.lubcon.com/. 34

Ludlow, A.D., Zelevinsky, T., Campbell, G.K., Blatt, S., Boyd, M.M., de Miranda, M.H.G., Martin, M.J., Thomsen, J.W., Foreman, S.M., Ye, J., Fortier, T.M., Stalnaker, J.E., Diddams, S.A., Le Coq, Y., Barber, Z.W., Poli, N., Lemke, N.D., Beck, K.M. & Oates, C.W. (2008). Sr Lattice Clock at 1 x 10-16 Fractional Uncertainty by Remote Optical Evaluation with a Ca Clock. *Science*, **319**, 1805–1808. 22

Magma (2007). http://www.magma.com/index.html. 41

Mattke AG (2008). http://www.mattke.de/. 29, 33

McCarthy, D.D. & Petit, G. (2003). IERS Conventions. Tech. Rep. 32, International Earth Rotation and Reference Systems Service (IERS). 114

MicroG-LaCoste (2008). http://www.microglacoste.com/index.html. 14, 25

Micro Präzision Marx GmbH (2006). http://www.mpmgmbh.de/. 57, 75

Moritz, H. & Hofmann-Wellenhof, B. (1993). *Geometry, Relativity, Geodesy*. H. Wichmann. 107

Müller, J., Neumann-Redlin, M., Jarecki, F., Denker, H. & Gitlein, O. (2007). *Gravity Changes in Northern Europe as Observed by GRACE*, vol. 130 of *International Association of Geodesy Symposia*, 523–527. Springer Berlin Heidelberg. 122

Murata, I. (1978). A transportable apparatus for absolute measurement of gravity. *Bulletin of the Earthquake Research Institute*, **53**, 49–130. 91, 108

Nagornyi, V.D. (1995). A new approach to absolute gravimeter analysis. *Metrologia*, **32**, 201–208. 108

Newport (2007). http://www.newport.com/. 26, 96

Niebauer, T.M. (1987). *New Absolute Gravity Instruments for Physics and Geophysics.*. Ph.D. thesis, UNIVERSITY OF COLORADO AT BOULDER. 13

Niebauer, T.M. (1989). The effective measurement height of free-fall absolute gravimeters. *Metrologia*, **26**, 115–118. 108

Niebauer, T.M., Sasagawa, G.S., Faller, J.E. & Klopping, F. (1995). A new generation of absolute gravimeters. *Metrologia*, **32**, 159–180. 2, 14, 15, 26, 51, 61, 78, 85, 87, 88, 91

Niebauer, T.M., Schiel, A. & van Westrum, D. (2006). Complex heterodyne for undersampled chirped sinusoidal signals. *Appl. Opt.*, **45**, 8322–8330. 32

NIST (2008). http://physics.nist.gov/constants. 21, 125

ONERA (2008). http://www.onera.fr/dmph-en/cold-atom-devices/inertial-measurements.php. ix, 18

Opta GmbH (2008). http://www.opta-gmbh.de/. 34

Pawlowski, B. (1998). Gravity gradiometry in resource exploration. *The Leadin Edge*, 51–52. 122

Peck, E. (1948). Theory of the corner-cube interferometer. *J. Opt. Soc. Am.*, **38**, 1015–1024. 16, 85

Peters, A., Chung, K.Y. & Chu, S. (1999). Measurement of gravitational acceleration by dropping atoms. *Nature*, **400**, 849–852. 2, 17

Phytron (2008). http://www.phytron-elektronik.de/. 42

PLX Inc. (2008). http://www.plxinc.com. 74

Renishaw (2006). http://www.renishaw.com/en/1030.aspx. 61

Rinker, R.L.I. (1983). *Super Spring – a New Type of Low-Frequency Vibration Isolator.*. Ph.D. thesis, UNIVERSITY OF COLORADO AT BOULDER. 15, 25

Robinson, I.A. & Kibble, B.P. (2007). An initial measurement of plancks constant using the npl mark ii watt balance. *Metrologia*, **44**, 427–440. 21

Rosenband, T., Hume, D.B., Schmidt, P.O., Chou, C.W., Brusch, A., Lorini, L., Oskay, W.H., Drullinger, R.E., Fortier, T.M., Stalnaker, J.E., Diddams, S.A., Swann, W.C., Newbury, N.R., Itano, W.M., Wineland, D.J. & Bergquist, J.C. (2008). Frequency Ratio of Al+ and Hg+ Single-Ion Optical Clocks; Metrology at the 17th Decimal Place. *Science*, **319**, 1808–1812. 22

Rothleitner, C., Svitlov, S., Mérimèche, H. & Wang, L.J. (2007). A method for adjusting the centre of mass of a freely falling body in absolute gravimetry. *Metrologia*, **44**, 234–241. 52

Sabuga, W. (2007). Towards 7 mpa pressure standards with 110-6 uncertainty. *MAPAN - Journal of Metrology Society of India*, **22**, 3–11. 20

Schneider, H. (2003). *Auswuchttechnik*. Springer VDI. 54, 59, 60, 70, 77

Schwarz, J.P. (1998). *The Free-Fall Determination of the Universal Constant of Gravity*. Ph.D. thesis, UNIVERSITY OF COLORADO AT BOULDER. 22

Schwarz, J.P., Robertson, D.S., Niebauer, T.M. & Faller, J.E. (1998). A free-fall determination of the newtonian constant of gravity. *Science*, **18**, 2230 – 2234. 22

Schwitz, W., Jeckelmann, B. & Richard, P. (2004). Towards a new kilogram definition based on a fundamental constant. *Comptes Rendus Physique*, **5**, 881–892. 2, 20, 21

Seidelmann, P.K., ed. (1992). *Explanatory Supplement to the Astronomical Almanac*. University Science Books. 3, 11, 113

Slepak, Z. (1997). Complex Geophysical Investigations for Studying the Cultural Layer and Remains of Ancient Buildings in the Territory of Kazan Kremlin, Kazan, Republic of Tatarstan, Russia. *Archaeological Prospection*, **4**, 207–218. 122

Sommer, K. & Siebert, B. (2006). Systematic approach to the modelling of measurements for uncertainty evaluation. *Metrologia*, **43**, 200–210. 64

Speake, C.C. (1987). Fundamental limits to mass comparison by means of a beam balance. *Proceedings of the Royal Society of London. Series A, Mathematical and Physical Sciences*, **414**, 333–358. 104

SRS (2007). http://www.thinksrs.com/. 28, 97

Steiner, R., Newell, D. & Williams, E. (2005). Details of the 1998 watt balance experiment determining the planck constant. *J. Res. Natl. Inst. Stand. Technol.*, **110**, 1–26. 21

Su, Y., Heckel, B.R., Adelberger, E.G., Gundlach, J.H., Harris, M., Smith, G.L. & Swanson, H.E. (1994). New tests of the universality of free fall. *Phys. Rev. D*, **50**, 3614–3636. 5

Svetlov, S.M. (1997). An absolute gravimeter and vibration disturbances: A frequency response method. In J. Segawa, H. Fujimoto & S. Okubo, eds., *Gravity, Geoid and Marine Geodesy*, 117, 47–54. 103, 105

Taylor, B. & Kuyatt, C. (1993). Guidelines for evaluating and expressing the uncertainty of nist measurement results. 69, 84

THK (2008). http://www.thk.com/. 33, 42

Timmen, L. (1994). *Untersuchungen zur Modellbildung bei der Auswertung absoluter Schweremessungen.*. Ph.D. thesis, Universität Hannover. 107

Timmen, L. (2003). Precise definition of the effective measurement height of free-fall absolute gravimeters. *Metrologia*, **40**, 62–65. 108, 109

Timmen, L., Röder, R.H. & Schnüll, M. (1993). Absolute gravity determination with JILAG-3 - improved data evaluation and instrumental technics. *Bull. Géod.*, **67**, 71–80. 106

Torge, W. (1989). *Gravimetry*. Walter de Gruyter. 2, 14, 104

TSoft (2008). http://www.astro.oma.be/SEISMO/TSOFT/tsoft.html. 11, 35, 111

Tsubokawa, T. & Svitlov, S. (1999). New method of digital fringe signal processing in an absolute gravimeter. *IEEE Trans. Instrum. Meas.*, 488–491. 32

van Camp, M. (2005). Introduction to the earth tides. In *Summer School on Microgravimetric methods: Static and Dynamic Aspects*, Lanzarote, Canarian Islands. 113

van Camp, M. & Vauterin, P. (2005). Tsoft: graphical and interactive software for the analysis of time series and earth tides. *Computers & Geosciences*, **31(5)**, 631–640. 11, 111

Varian Inc (2008). http://www.varianinc.com/cgi-bin/nav?/. 34

Vauterin, P. & van Camp, M. (2007). *TSoft Manual 2.1.1*. Royal Observatory of Belgium, Royal Observatory of Belgium Avenue Circulaire 3, B-1180 Bruxelles BELGIUM. 114

Vitouchkine, A. & Faller, J. (2004). A direct and sensitive method for positioning the centre of mass of a dropping object at the optical centre of the enclosed corner cube in ballistic absolute gravimeters. *Metrologia*, **41**, L19–L21. 51, 54

Wahr, J.M. (1985). Deformation induced by polar motion. *Journal of Geophysical Research*, **90**, 9363–9368. 114

Walker, G. (2004). STANDARDS: A Most Unbearable Weight. *Science*, **304**, 812–813. 20

Wenzel, H.G. (1996b). The nanogal software: Earth tide data processing package ETERNA 3.30. *Bulletin d'Information Mareés Terrestres*, **124**, 9425–9439. 11

Westrum, D. & Niebauer, T.M. (2003). The diffraction correction for absolute gravimeters. *Metrologia*, **40(5)**, 258–263. 99

Wignall, J. (2005). An absolute replacement for the standard kilogram. *Meas. Sci. Technol.*, **16**, 682684. 20

Williams, E.R. (1998). An accurate measurement of planck's constant using a watt balance experiment. *APS Meeting Abstracts*, C1903+. 21

Zumberge, M. (1981). *A Portable Apparatus for Absolute Measurements of the Earth's Gravity.*. Ph.D. thesis, UNIVERSITY OF COLORADO AT BOULDER. 87, 108

# Acknowledgements

There are a number of people I would like to thank for making it possible to graduate in this *attracting* field.

First I am indebted greatly to my supervisor, Prof. Lijun Wang. I want to thank him for enabling me, a theorist by training, to enter experimental physics, for his supervision, and for creating a division of talented individuals. Due to the broad diversity of members there was always an expert I could ask for advice. I am grateful to his insight, advice, and encouragement, and to share with me his knowledge about precision measurements.

I am indebted to Dr. Sergiy Svitlov. He taught me the art of *looking into the residuals*, and shared with me his enormous knowledge on gravimetry and metrology. He is a good colleague and a good friend. I will always remember our daily "cake breaks" where we often discussed our *crazy ideas*.

I want to thank Dr. Habib Mérimèche, who introduced me to the gravimetry project, and Dr. Andreas Pförtner who started it (although I never knew him). Here also many thanks to Pawel Maslyk, a distinguished young programmer. I admired how quickly he understood a problem and how he wrote the code.

Prof. Wang's group members, both past and present, have contributed greatly to this thesis. A special thanks to Felix Müller, Dr. Zehuang Lu, Jie Zhang, Yanhui Wang, Dr. Vladimir Elman, and Dr. Harald Schwefel for some of the *expert* advice. Special thanks to Dr. Jessica Mondia who helped me to convert a "mess" into an accepted article. I would like to thank all members of division II, i.e. Dr. Tao Liu, Dr. Stefan Malzer, Dr. Mingying Peng, Dr. Alois Stejskal, Dr. Bo Wang, Dr. Jinxiong Wang, Dr. Jianwei Zhang, Dr. Quanzhong Zhao, Dr. Marian Florentin Ciobanu, Simon Heugel, Sascha Preu, Jan Schäfer, Rachit Sharma, Benjamin Sprenger, Yanning Zhao, Dr. Rainer Dumke, Wolfgang Köhler and Simon Grams for their support. Thanks also goes to Kirsten Oliva, our secretary, who helped proof read my thesis and took care of many other administrative

duties.

The gravimeters required a lot of technical expertise. Constructing precision instruments is not possible without expert technical advise. I want to thank Klaus Kärcher for his excellent technical drawings, Thomas Spona and his crew from the machine shop (especially Bernhard), as well as Klaus Streeb and company from the electronic shop.

To all the external Professors who contributed to the project I would like to thank. In particular, Prof. James Faller for his visits and fruitful discussions at our institute. It is invaluable to talk to a *pioneer* in this field. Prof. Olivier Francis enabled me to compare our "baby" MPG-2 with many other gravimeters. Dr. Herbert Wilmes and Dr. Reinhard Falk made it possible to find the *last 500 $\mu Gal$*, by making another comparison in Bad Homburg.

I have thanked the people who helped me with the experiment. Now I want to give a hug to all the people who have helped me to make it through. First to my parents Harald and Maria Rothleitner, who did so much in their life for me, and to my sister Silvia and to my brothers Harald, Martin (who also helped me with the coordinate measuring machine), Wolfgang, and Andreas. Then to all my friends, who supported me during difficult times. The biggest hug, however, together with a kiss, belongs to my beloved wife Johanna. She always believed in me, and helped me switch off the physics in my head, when necessary.

# Curriculum Vitae


## Christian Rothleitner

*15 January 1973 in Berlin, Germany

German

Married


## Academic Career

Apr. 2005 – now

Doctorate studies of Experimental Physics, Max Planck Research Group, University of Erlangen-Nuremberg, Germany

Topic of thesis:

*Ultra-high Precision, Absolute, Earth Gravity Measurements*

Apr. 2003 – Dec. 2004

Studies of Physics, University of Erlangen-Nuremberg, Germany

Topic of diploma thesis (Theoretical Physics):

*Vergleich der Gross-Projektion und der Heavy Quark Effective Theory für Zweiteilchensysteme mit einem sehr schweren und einem leichten Quark*

Feb. 1999 – Jan. 2003

Studies of Physics, University of the Andes, Merida, Venezuela

*Studies had to be interrupted because of political riots*

Oct. 1997 – Jan. 1999

Studies of Physics, University of Erlangen-Nuremberg, Germany

Apr. 1997 – Sep. 1997

Studies of Physics, University of Parma, Italy

Oct. 1994 – Mar. 1997

Studies of Physics, University of Erlangen-Nuremberg, Germany

Oct. 1992 – Sep. 1994

Studies of Precision- and Micro Engineering

University of Applied Sciences, Nuremberg, Germany

## Publications

Dillig, M. & Rothleitner, C. (2006). Multinucleon mechanisms in inclusive subthreshold k+ production in p+c12 collisions at 1 GeV. *http://www.citebase.org/abstract?id=oai:arXiv.org:nucl-th/0604056*.

Dillig, M. & Rothleitner, C. (2007). Quenching of the deuteron in flight. *International Journal of Modern Physics E*, **16**, 69.

Rothleitner, C., Svitlov, S., Mérimèche, H. & Wang, L.J. (2007a). A method for adjusting the centre of mass of a freely falling body in absolute gravimetry. *Metrologia*, **44**, 234–241. 52

## Oral Presentations

Rothleitner, C., Svitlov, S.M. & L.J., Wang (2007b). The MPG Free-Fall Absolute Gravimeters. In *Terrestrial Gravimetry: Static and Mobile Measurements*, Saint Petersburg, Russia.